

# Spin-Correlation Coefficients and Phase-Shift Analysis for $p+{}^3\text{He}$ Elastic Scattering

Timothy Vaughn Daniels

A dissertation submitted to the faculty of the University of North Carolina at Chapel Hill in partial fulfillment of the requirements for the degree of Doctor of Philosophy in the Department of Physics and Astronomy.

Chapel Hill  
2009

Approved by:

T. B. Clegg, Advisor

H. J. Karwowski, Reader

W. Tornow, Reader

Y. Wu, Reader

E. J. Ludwig, Reader

C. R. Brune, Reader

© 2009  
Timothy Vaughn Daniels  
ALL RIGHTS RESERVED

# Abstract

**TIMOTHY VAUGHN DANIELS: Spin-Correlation Coefficients and Phase-Shift  
Analysis for  $p+{}^3\text{He}$  Elastic Scattering.  
(Under the direction of T. B. Clegg.)**

A new spin-exchange optical pumping polarized  ${}^3\text{He}$  target has been used to measure angular distributions of  $A_{0y}$ ,  $A_{yy}$ , and  $A_{xx}$  for  $p+{}^3\text{He}$  elastic scattering at proton energies of 2.28, 2.77, 3.15, 4.02, and 5.54 MeV. The new data, along with previous cross-section and beam analyzing power measurements were included in a global phase-shift analysis of data below 12 MeV. The additional data resolved the ambiguity in that analysis, and a unique set of energy-dependent phase-shifts was obtained. These phase-shifts, as well as the data themselves, were compared to theoretical calculations using realistic nuclear potential models that accurately reproduce NN scattering data. These calculations underpredicted  $A_{0y}$ , in addition to the previously-observed underprediction of  $A_{y0}$  known as the “ $A_y$  puzzle”. The spin-correlation coefficients were found to be better reproduced. There was good agreement for the S-wave phase-shifts, while the P-wave phases showed small discrepancies, especially for  ${}^3\text{P}_2$  and  ${}^3\text{P}_0$ , and different discrepancies were observed for different interaction models.



*to Amy*



# Acknowledgments

This project would not have been successful without the help and support of many people. The value of the patient guidance of my thesis advisor, Professor Thomas Clegg, through all the stages of my graduate studies cannot be overstated. Professor Hugon Karwowski also provided advice and critical feedback throughout. I thank them for their energy, enthusiasm, and accessibility. I am also grateful for Dr. Tatsuya Katabuchi's intelligence, attention to detail, and cheerfulness.

Many others have contributed to my success at TUNL. Dr. Brian Fisher and Dr. Doug Leonard showed me the ropes when I first arrived. Charles Arnold, Alex Couture, John Cesaratto, and Dr. Astrid Imig were the core team that performed the data-taking, with participation by Dr. Chris Angell. I thank them for hard work on a difficult experiment. I also thank John for tolerating the mess in our office. TUNL staff members John Dunham, Richard O'Quinn, Paul Carter, Bret Carlin, Patrick Mulkey, Brenda West, Dr. Alex Crowell, and Chris Westerfeldt have provided help and advice on subjects including vacuum pumps, beam sources, accelerator operation, radioactive sources, LabVIEW, using the copy machine, and local breweries.

Professor Elizabeth George provided the  $p+^3\text{He}$  phase-shift code along with very helpful advice on the phase-shift analysis. Professor Richard Prior provided the phase-shift code used for  $p+^4\text{He}$  scattering. Richard Longland and Dr. Michael Akashi-Ronquest tried valiantly to help me make a working GEANT4 target simulation.

Joseph Newton and Dr. Mitzi Boswell have been great friends who pitched in on my experiment, advised me on any number of subjects in physics and life in general, and with whom I enjoyed many beers. My family has also been a source of great support, especially my parents Craig and Sherry. Thanks for believing in me.

Finally, the love and support of my wife Amy have been invaluable.

Timothy Vaughn Daniels  
April 2009





# Table of Contents

<b>Abstract</b>	<b>iii</b>
<b>List of Tables</b>	<b>xi</b>
<b>List of Figures</b>	<b>xiii</b>
<b>1 Introduction</b>	<b>1</b>
<b>2 Theory</b>	<b>7</b>
2.1 Interaction Models . . . . .	7
2.2 Methods . . . . .	8
<b>3 Polarized Target</b>	<b>12</b>
3.1 Scattering Target . . . . .	13
3.2 Optical Pumping . . . . .	16
3.3 Optical Pumping Cells . . . . .	17
3.4 Polarizer . . . . .	21
3.5 Narrowed Laser . . . . .	22
3.6 Performance Summary . . . . .	25
<b>4 Observables</b>	<b>26</b>
4.1 Spin- $\frac{1}{2}$ Formalism . . . . .	27
4.1.1 One Particle . . . . .	27
4.1.2 Two Particles . . . . .	28
4.2 Observables . . . . .	29
4.3 Detector Yields . . . . .	31
<b>5 Data Collection and Analysis</b>	<b>33</b>
5.1 Experimental Set-Up . . . . .	33
5.2 Spectra . . . . .	36
5.2.1 Peak Sums . . . . .	36
5.2.2 Background . . . . .	39

5.2.3	Dead Time . . . . .	42
5.3	Asymmetries . . . . .	43
5.4	Polarized Beam Preparation . . . . .	43
5.5	Measurement of Beam Polarization . . . . .	44
5.6	Measurement of Target Polarization . . . . .	46
5.7	Location of Calibration Point . . . . .	48
5.8	Spin-Correlation Coefficients . . . . .	51
5.9	Steering Effect . . . . .	51
<b>6</b>	<b>Phase-Shift Analysis</b>	<b>57</b>
6.1	Calculation of Observables . . . . .	57
6.2	Partial-Wave Expansion . . . . .	59
6.3	Effective Range Expansion . . . . .	60
6.4	Procedure . . . . .	61
<b>7</b>	<b>Results</b>	<b>66</b>
7.1	Observables . . . . .	67
7.2	Phase-Shifts . . . . .	77
7.2.1	Comparison with Theory . . . . .	82
7.3	Scattering Lengths . . . . .	91
<b>8</b>	<b>Conclusions</b>	<b>92</b>
<b>A</b>	<b>Beam Spin Precession</b>	<b>97</b>
<b>B</b>	<b>Angular Momentum Coupling</b>	<b>99</b>
<b>C</b>	<b>Data Tables</b>	<b>100</b>
	<b>Bibliography</b>	<b>105</b>

# List of Tables

1.1	Global $p+{}^3\text{He}$ data set . . . . .	4
1.2	Theoretical scattering lengths . . . . .	4
1.3	Experimental scattering lengths . . . . .	5
3.1	Performance summary of optical pumping cells . . . . .	21
5.1	Target cell bombarding energies . . . . .	35
5.2	Estimated precision for TRIM stopping powers . . . . .	35
5.3	Polarimeter cell bombarding energies . . . . .	45
5.4	Polarimeter cell analyzing powers . . . . .	46
5.5	Bombarding energies for target cell calibrations . . . . .	48
5.6	Bombarding energies for $\alpha+{}^3\text{He}$ $A_y$ minimum . . . . .	49
6.1	Points dropped from the phase-shift analysis . . . . .	63
6.2	Best-fit effective-range parameters . . . . .	64
6.3	Single-energy phase-shift results . . . . .	65
6.4	Global phase-shift results . . . . .	65
7.1	Theoretical scattering lengths . . . . .	91
7.2	Experimental scattering lengths . . . . .	91
B.1	Angular momentum coupling . . . . .	99
B.2	Mixing between orbital angular momentum states . . . . .	99
C.1	Data at 2.28 MeV . . . . .	101
C.2	Data at 2.77 MeV . . . . .	101
C.3	Data at 3.15 MeV . . . . .	102
C.4	Data at 4.02 MeV . . . . .	102
C.5	Data at 5.54 MeV . . . . .	103



# List of Figures

1.1	Observables for $p+{}^3\text{He}$ elastic scattering at 4 MeV . . . . .	6
2.1	Jacobi vectors for four-nucleon calculations . . . . .	10
3.1	Overview of the polarized target . . . . .	14
3.2	A target cell . . . . .	15
3.3	The sine-theta coil . . . . .	16
3.4	Sine-theta coil currents . . . . .	17
3.5	Atomic levels in Rb relevant to optical pumping . . . . .	18
3.6	An optical pumping cell . . . . .	18
3.7	Accumulation of ${}^3\text{He}$ polarization . . . . .	19
3.8	Alkali filling station for optical pumping cells . . . . .	20
3.9	Polarizer schematic . . . . .	23
3.10	Narrowed laser output . . . . .	24
5.1	Diagram of chamber setup . . . . .	34
5.2	Diagram of spin-flip electronics . . . . .	36
5.3	Chamber detector spectrum for ${}^3\text{He}(p,p){}^3\text{He}$ . . . . .	37
5.4	Chamber detector spectrum for ${}^3\text{He}(\alpha,\alpha){}^3\text{He}$ . . . . .	38
5.5	Polarimeter detector spectrum . . . . .	38
5.6	Polarimeter background . . . . .	40
5.7	Chamber background . . . . .	40
5.8	Wein Filter Calibration . . . . .	45
5.9	Target cell “spin-down” . . . . .	47
5.10	Determination of target nmr calibration constant. . . . .	48
5.11	${}^4\text{He} + {}^3\text{He}$ $A_y$ measurements with respect to angle . . . . .	50
5.12	${}^4\text{He} + {}^3\text{He}$ $A_y$ measurements with respect to energy . . . . .	50
5.13	Instrumental steering effect . . . . .	52
5.14	Steering of the incoming proton beam and scattered particles by the sine-theta coil magnetic field . . . . .	52
5.15	Deflection of the incoming beam and scattered particles through angles $\alpha$ and $\beta$ , respectively, by the sine-theta coil magnetic field. . . . .	53
5.16	Angular distribution of $A_{y0}$ for $p+{}^3\text{He}$ elastic scattering at 2.25 MeV . . . . .	54
5.17	Calculated instrumental effect for $A_{y0}$ at 2.25 MeV . . . . .	55
5.18	Extrapolation of systematic asymmetries to zero target polarization . . . . .	55
5.19	Correction for systematic asymmetry for $A_{y0}$ at 2.25 MeV . . . . .	56

6.1	Measurements of $A_{y0}$ at 1.60 MeV shown with the phase-shift solution . . . .	63
7.1	Present results at 2.28 MeV . . . . .	69
7.2	Present results at 2.77 MeV . . . . .	70
7.3	Present results at 3.15 MeV . . . . .	71
7.4	Present results at 4.02 MeV . . . . .	72
7.5	Present results at 5.54 MeV . . . . .	73
7.6	Comparison of 3.15 MeV measurements with theoretical calculations . . . . .	74
7.7	Comparison of 3.15 MeV measurements with theoretical calculations . . . . .	75
7.8	Comparison of 5.54 MeV measurements with theoretical calculations . . . . .	76
7.9	Results for S-wave phase-shifts . . . . .	78
7.10	Results for P-wave phase-shifts . . . . .	79
7.11	Results for D- and F-wave phase-shifts . . . . .	80
7.12	Results for mixing parameters . . . . .	81
7.13	Comparison with theoretical S-wave phase-shifts. . . . .	84
7.14	Comparison with theoretical P-wave phase-shifts . . . . .	85
7.15	Comparison with theoretical P-wave phase-shifts . . . . .	86
7.16	Comparison with theoretical D-wave phase-shifts. . . . .	87
7.17	Comparison with theoretical ${}^3F_2$ and mixing parameters . . . . .	88
7.18	Triplet P-wave splitting. . . . .	89
7.19	Comparison of phase-shifts to theoretical results . . . . .	90

# 1 Introduction

---

According to our modern understanding, protons and neutrons interact through the strong nuclear force to form atomic nuclei. The exact form of the interaction between the “nucleons” has been sought since the proposal of this picture of the nucleus, which in fact predates both the discovery of the neutron and the development of the Standard Model [Bro96]. We now believe that nucleons are composed of quarks and gluons, which interact according to Quantum Chromodynamics (QCD). The force between nucleons should be derivable from this underlying physics in much the same way that molecular forces can be derived from the electromagnetic interaction of atomic electrons. The difficulty of solving QCD in the non-perturbative nuclear regime, however, has prevented that derivation.

A model of the nucleon-nucleon interaction would, in principle, allow one to understand nuclear systems in terms of their constituent nucleons. Such an *ab initio* approach requires both a workable model of the interaction and computational techniques to solve it for a system of multiple nucleons. Because the interaction has not been derived from QCD, physicists have developed various phenomenological models. These models start from the general experimentally-deduced description of the nuclear force, which is described in many nuclear physics textbooks, such as [Ros48, Kap62, Kra88]. The meson exchange model, first proposed by Yukawa in 1935 [Yuk35], accounts for many of the observed features, including finite range, saturation, and spin-dependence. More phenomenological terms are included to describe the short-range repulsion as well as more subtle effects such as charge symmetry breaking. As a result, the models have free parameters which must be adjusted to reproduce experimental data. Several models now exist which accurately describe the extensive NN scattering database [Car98].

According to the *ab initio* approach, these “realistic” models should also be able to describe more complicated nuclear systems. Several methods now exist to apply these models to the three-nucleon (3N) and four-nucleon (4N) systems, and a wide variety of bound state and scattering observables have been calculated [Car98]. Calculations of the  $^3\text{H}$  and  $^3\text{He}$  binding

energies find that a three-nucleon force (3NF) must be added to the potential models in order to reproduce the experimental values [Nog02, Nog03]. The models generally reproduce p+d and n+d scattering data well. There are a few significant exceptions to this success, including the “ $A_y$  puzzle”, in which the nucleon and deuteron vector analyzing powers for elastic scattering at low energy are under predicted [Glö96].

In the 4N system, the alpha-particle binding energy is well reproduced without additional interactions beyond the 3NF [Wir00, Nog02, Viv05b], but an even stronger  $A_y$  puzzle has been firmly established for p+ $^3\text{He}$  elastic scattering [Fis06]. Despite this and some other discrepancies, observables in many 4N reactions are well reproduced [Del07a, Del07b, Del07c]. For heavier systems, bound-state properties have been calculated up to  $A=12$  [Nav03, Pie04], as well as n+ $^4\text{He}$  elastic scattering phase-shifts [Car07].

The four-nucleon system provides a more difficult challenge to nuclear interaction models than either the 2N or 3N systems, and has been characterized as a “theoretical laboratory” for studying those models [Laz05]. It is more tightly bound than the latter two systems, which should amplify the importance of both the more phenomenological short-range parts of interaction models and 3NF. It is also the lightest nuclear system to exhibit such typical “nuclear” properties as resonances and thresholds [Til92], which makes its accurate description an important milestone for *ab initio* nuclear physics. Finally, calculating the interaction between four nucleons uses 3NF in higher isospin channels than have so far been available.

The work described in this thesis is aimed at clarifying the comparison of theory and experiment in p+ $^3\text{He}$  elastic scattering at the low energies relevant to the  $A_y$  puzzle. A unique set of experimental phase-shifts and mixing parameters for the system would allow a systematic comparison to theoretical models and perhaps establish which partial waves are to blame for the disagreement. Phase-shift analyses, in which these parameters are fit to measured angular distributions of scattering observables, have been attempted since the first measurements were made in 1954, but have historically been hampered by the lack of double-polarized observables.

The global data-set for p+ $^3\text{He}$  elastic scattering below 12 MeV proton energy is summarized in Table 1.1. The first measurements were angular distributions of differential cross-section by Famularo in 1954 [Fam54]. A few other cross-section measurements were made in the following several years [Swe55, Lov56, Bro60, Art60] and phase-shift analyses [Low54, Fra55] of available data indicated that no spin-dependence was necessary to reproduce those data. In the 1960’s, systematic measurements of precision cross sections became available [Tom62, Cle64, McD64, Tom65, Kav66, Dri66], as well as  $A_{y0}$  obtained from double-scattering experiments [Ros60, McD64, Dri66]. Spin-dependent analyses were attempted [Tom62, Cle64, Tom65, Dri67] but wide solution bands were still possible. In the late ’60s, polarized proton beams and polarized  $^3\text{He}$  targets were developed, so that high-quality  $A_{y0}$  [Mor69, Det79] as well as  $A_{0y}$  [McS70, May73, Bly75, Sza78b], spin-correlation



coefficients [McS69, May73], and spin-transfer coefficients [Wei78], as well as cross-sections and  $A_{y0}$  below 1 MeV [Ber80] became available. Phase shift analyses [McS69, Mor69, Bos72, Bly75, Sza78a, Ber80, Bel85] including these data were better constrained, but the solutions were generally not unique.

The situation improved substantially in 1993, when Alley and Knutson published an energy-dependent, global analysis which included their measurements of  $A_{y0}$ ,  $A_{0y}$ , and  $A_{yy}$  at 4, 5.54, 7, 8.5, and 10 MeV, as well as  $A_{xx}$ ,  $A_{xz}$ ,  $A_{zx}$ , and  $A_{zz}$  at 5.54 MeV [All93a]. This dramatic increase in the available spin-correlation data enabled subsequent analyses [All93b, Yos00] to obtain unique solutions. However, a later reanalysis that included the Berg cross-section and analyzing power measurements below 1 MeV, as well as  $A_{y0}$  measurements between 1 and 2 MeV, found two distinct solutions [Geo03]. The observables most sensitive to the difference between those solutions are spin-correlation coefficients below 4 MeV. That is not surprising, since no such measurements are present in the database.

The first theoretical calculation for the  $p+{}^3\text{He}$  elastic scattering observables was by Swan in 1953 [Swa53], who obtained scattering phase-shifts from simple interaction models using variational methods. The first scattering calculation using a realistic model for the system was of the triplet scattering length by Carlson *et al.* in 1991 [Car91], who used a variational approach with the AV14+URVII potential. That work was motivated in part by the fact that the triplet scattering length is an important input parameter in calculations of the weak  $p-{}^3\text{He}$  capture rate, which is the reaction that produces the highest-energy solar neutrinos. The singlet and triplet scattering lengths were calculated in 2000 by both Filikhin and Yakovlev [Fil00], who used a cluster reduction method to solve the Fadeev-Yakubovski equations with the Malfet-TjonI-III potential. The scattering lengths were also calculated by the Pisa group, Viviani, Rosati, and Kievski [Viv98], who used the Correlated Hyperspherical Harmonics with the Kohn variational principle to solve the Schrodinger equation with the AV14 and AV18 potentials with a variety of 3N interactions. These three calculations, summarized in Table 1.2, disagree with one another, which implies that experimental values for the scattering lengths might distinguish between them.

Scattering lengths for the system can be obtained from experimental phase shifts by extrapolating a parameterization of the energy dependence of the appropriate phase shift to zero energy, and the three available values are summarized in Table 1.3. Tegner and Bargholtz [Teg83] fit an effective range expansion to the  ${}^3\text{S}_1$  phase shifts of [Tom65] and [Ber80] to obtain the triplet scattering length. The energy dependent phase-shift analyses of [All93b] and [Geo03] determine scattering lengths explicitly as search parameters. The scattering lengths from the two solutions of [Geo03] disagree with each other as well as with those from [All93b], which in turn disagree with [Teg83].

Today, several realistic calculations of scattering observables for the system are also available. The Pisa group published the first such calculations in 2001 [Viv01], extending their

Table 1.1: Global data set. See section 6.4 for a discussion of [Geo03] data groups.

Reference	$E_p$	Observable	PSA?	in [Geo03]? (group)
[Fam54]	1.01-3.53	$\sigma$	n	y (5)
[Low54]	1.01-3.53	-	y	-
[Swe55]	4.96, 8.6	$\sigma$	n	n
[Fra55]	1.0-3.5	-	y	-
[Lov56]	9.75	$\sigma$	n	y (14)
[Bro60]	6.5, 8.3	$\sigma$	n	y (13)
[Art60]	4.96, 8.6	$\sigma$	n	n
[Ros60]	10	$A_{y0}$	n	n
[Tom62]	2.0-4.8	$\sigma$	y	n
[Cle64]	4.55-11.48	$\sigma$	y	y (11)
[McD64]	4.05-12.79	$\sigma, A_{y0}$	n	y (9,10)
[Tom65]	1-11.5	-	n	-
[Kav66]	0.125-2.0	$\sigma$ (excitation)	n	n
[Dri66]	3.38-4.46	$A_{y0}$	y	excluded
[Mor69]	4.0-10.8	$A_{y0}$	y	y (12)
[McS69]	8.8	$A_{xz}$	y	y (4)
[McS70]	3.86-10.94	$A_{0y}$	y	y (4)
[Bos72]	4-10.77	-	y	-
[May73]	6.80, 8.82	$A_{y0}, A_{0y}, A_{xx}, A_{yy}$	?	y (3)
[Bly75]	10.5	$A_{0y}$	y	y (8)
[Sza78b]	2.3-8.8	$A_{0y}$	y	y (7)
[Sza78a]	13.6	-	y	-
[Wei78]	6.82, 8.82, 10.7	$K_{xx}, K_{yy}, K_{xz}$	n	n
[Det79]	1.75-4.5	$A_{y0}$	R?	y (6)
[Ber80]	0.3-1.0	$\sigma, A_{0y}$	y	y (16,17)
[Bel85]	0-10	-	y	-
[Geo06]	12.4	$A_{0y}$	n	y (15)
[All93a]	4-10	$A_{y0}, A_{0y}, A_{yy}$	n	y (1,2)
[All93a]	5.54	$A_{xx}, A_{xz}, A_{zx}, A_{zz}$	n	y (1)
[All93b]	0-12	-	y	-
[Yos00]	4-20	-	y	-
[Viv01]	1.60, 2.25	$A_{0y}$	n	y (18)
[Geo03]	0-12	-	y	-
[Fis06]	1-4	$\sigma, A_{0y}$	y	-

Table 1.2: Theoretical scattering lengths

Reference	$a_s$ (fm)	$a_t$ (fm)
[Viv98]	11.5	9.13
[Fil00]	8.2	7.7
[Car91]		$10.1 \pm 0.5$

Table 1.3: Experimental scattering lengths

Reference	$a_s$ (fm)	$a_t$ (fm)
[Teg83]		$10.2 \pm 1.4$
[All93b]	$10.8 \pm 2.6$	$8.1 \pm 0.5$
[Geo03] Soln. 1	$15.1 \pm 0.8$	$7.9 \pm 0.2$
[Geo03] Soln. 2	$7.2 \pm 0.8$	$10.4 \pm 0.4$

earlier zero-energy calculations. Updated calculations are given in [Fis06]. Pfitzinger and collaborators [Pfi01] used the Resonating Group Model (RGM) with the AV18, AV8, URIX, and TRA potentials, and compared their results to an updated R-matrix analysis of  $T=1$  data in the four-nucleon system. Most recently, the Lisbon group, Fonseca and Deltuva, has solved the Alt-Grassberger-Sandhas (AGS) equations [Alt67] in momentum space for a variety of modern potentials, including one derived from effective field theory [Del07b]. Quaglioni and Navratil [Qua08] have developed a hybrid method that combines the RGM with the “no core shell model” (NCSM).

These calculations generally compare well with measured angular distributions of cross-section, but underpredict the beam analyzing power by as much as 40%, and the target analyzing power to a lesser extent. Calculations of the Pisa group [Viv05a] are shown with measurements from [Fis06] and [All93a] at 4 MeV proton energy in Figure 1.1. Spin-correlation coefficients agree within the large experimental uncertainties. This  $A_y$  puzzle is discussed by the various authors in terms of the P-wave phase shifts. In [Fis06], the authors report that  $A_y$  is strongly influenced by the combination  ${}^3P_2 - \frac{1}{2}({}^3P_1 + {}^3P_0)$ , the calculated value of which is smaller than would be necessary to reproduce the experiment data.

In order to clarify the comparison with theoretical calculations by better constraining the experimental phase-shift analysis, we have measured angular distributions of the spin-correlation coefficients  $A_{xx}$  and  $A_{yy}$  for  $p+{}^3\text{He}$  elastic scattering at 4 energies between 2.25 and 5.54 MeV. The measurements used a new polarized  ${}^3\text{He}$  target specifically designed for use in low-energy charged particle scattering. The remainder of the thesis describes the project in detail. Relevant theoretical calculations are discussed in Chapter 2, while the polarized target is described in Chapter 3. The experimental observables are defined in Chapter 4, while the experiment and analysis are described in Chapter 5. Chapter 6 describes the phase-shift analysis. The results are discussed in Chapter 7 and conclusions are laid out in Chapter 8.

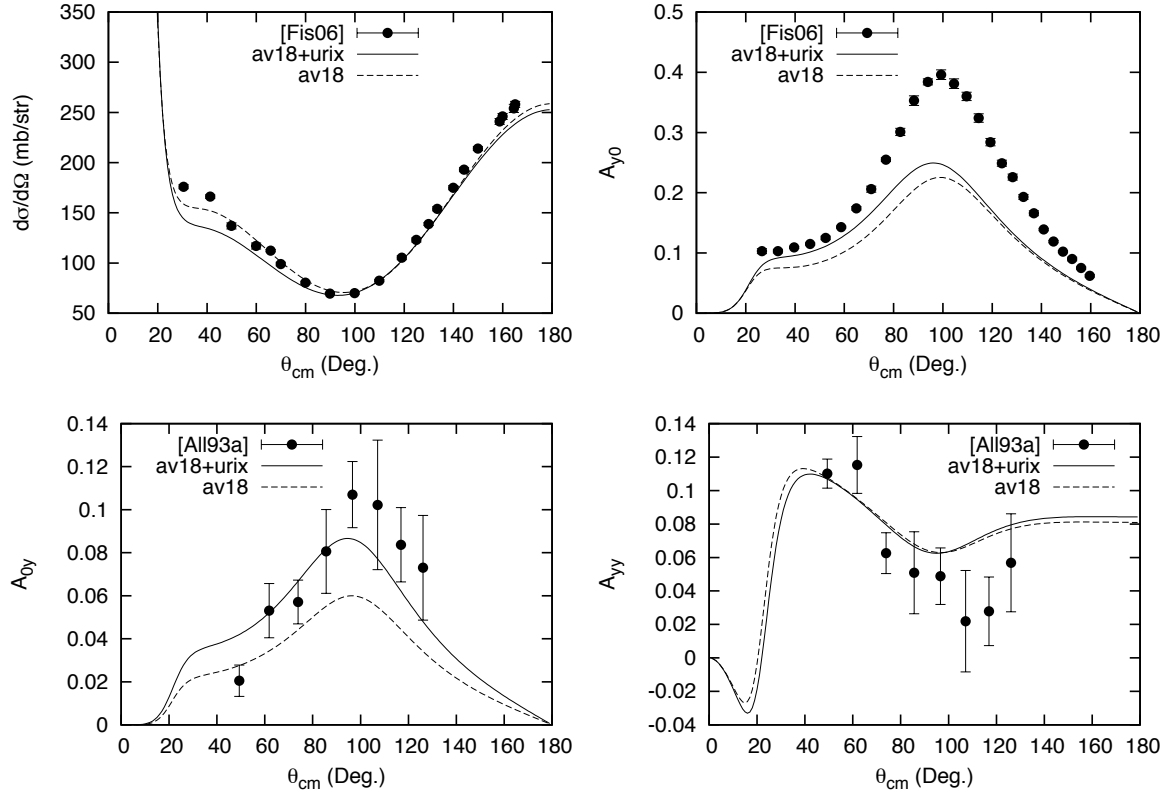


Figure 1.1: Observables for  $p+{}^3\text{He}$  elastic scattering at 4 MeV. The data are from [Fis06] and [All93a], while the theoretical calculations are from the Pisa group [Viv05a] and use the AV18 potential with and without the UR1X three-nucleon force.

## 2 Theory

---

### 2.1 Interaction Models

Two commonly-used models for the force between nucleons are AV18 [Wir95] and CD-Bonn [Mac01]. Both models use one-pion exchange to describe the long-range part of the force, and both include electromagnetic interactions. While the intermediate and short-range physics terms in both models are phenomenological and have about 40 free parameters adjusted to fit experimental data, the two differ in style. The terms in the AV18 potential are written in configuration space and are each of a different functional form with respect to the relevant variables, including position and spin. In this way, each term serves to include a particular feature, such as spin-orbit dependence or charge-independence breaking, into the model. In contrast, the terms of the CD-Bonn potential, written in terms of momentum, each correspond to the exchange of a different meson. A phenomenological  $\sigma$  meson is included to account for the two-meson exchange that is important at small distances, and it is primarily the coupling constants and masses of the  $\sigma$  mesons for each partial wave that are fit to data. The former model is therefore more explicitly phenomenological than the latter, but the two are fit to nucleon-nucleon scattering data and measured deuteron properties with similar accuracy.

As discussed in the Introduction, three-nucleon forces are required to reproduce  $^3\text{H}$  and  $^3\text{He}$  binding energies. The URIX model [Car83], used in [Fis06], is based on two-pion exchange and is written in configuration space. It contains two terms, each of which contains a parameter that is fit to experimental data. The first term describes two-pion exchange through an intermediate delta excitation, and is fit to the  $^3\text{H}$  and  $^4\text{He}$  binding energies. The second is more phenomenological and is fit to the equilibrium density of nuclear matter.

Other models have been developed by modifying the NN potentials described above to reproduce 3N properties directly. Deltuva and coworkers [Del03] have modified the CD-Bonn potential to couple nucleons explicitly to delta excitations through meson exchange. The

parameters of the  $\sigma$  mesons' coupling to the delta in each partial wave were adjusted to reproduce the Nijmegen NN database. This fit included the readjustment of some of the original nucleon-nucleon parameters. This “CD-Bonn +  $\Delta$ ” potential therefore includes a three-nucleon interaction without actually being fit to any 3N data, and still underbinds  $^3\text{H}$  and  $^3\text{He}$ , though to a lesser degree than CD-Bonn.

Doleschall and collaborators, in an attempt to exploit the connection between three-nucleon forces and non-local interactions described in [Pol90], have developed so-called “Inside non-local, outside Yukawa” (INOY) potentials. These potentials consist of a purely phenomenological non-local interaction at small distances (within about 3 fm) that smoothly connects to the AV18 potential at larger distances. In its most realistic form [Dol03], the non-locality is restricted to S and D waves and its parameters are fit to the Nijmegen NN database, deuteron properties, and the  $^3\text{He}$  binding energy. The more recent INOY04 [Dol04] and ISuj [Dol08] models include modified P-wave interactions which better describe nucleon-deuteron scattering below 10 MeV, including  $A_y$ .

A different approach to constructing nuclear potential models is chiral perturbation theory ( $\chi\text{PT}$ ). This approach, first used by Weinberg [Wei90], starts with the most general Lagrangian consistent with the approximate chiral symmetry of the underlying theory of QCD at low energy. Though interaction models developed in this way contain an infinite number of terms, Weinberg showed that they can be ordered in powers of the ratio of the momentum to the chiral-symmetry breaking scale. Actual potential models, therefore, contain a finite number of terms up to a given order. These terms are associated with either contact interactions or with pion exchange, and the contact terms contain constants which must be fit to NN data. A nucleon-nucleon potential at next-to-next-to-next-to leading order, (N<sup>3</sup>LO), containing 29 parameters has been constructed by Entem and Macleidt [Ent03]. Terms involving three or more nucleons emerge from the chiral Lagrangian just as NN terms do, so that chiral 3NF's can be constructed. For example, Navratil [Nav07] discusses the chiral 3NF at N<sup>2</sup>LO.

## 2.2 Methods

Several methods now exist to calculate  $p+^3\text{He}$  elastic scattering using realistic potential models. The Resonating Group Method (RGM), introduced into nuclear physics by Wheeler [Whe37a, Whe37b] to calculate light nuclear systems with simple NN interaction models, was used in the first  $p+^3\text{He}$  calculation [Swa53]. The method groups the nucleons into clusters and separately considers the inter-cluster interactions and the description of the clusters themselves. Several calculations using the RGM with the interactions between clusters derived from realistic models have been published [Pfi01, Rei03, Ara08]. In all these calculations, however, the description of the clusters is approximate and is accomplished with harmonic-oscillator (Gaussian) wave-functions whose parameters are determined variationally by minimizing the

overall ground-state energy.

Navratil and Quaglioni [Qua08, Qua09] have developed a hybrid method which combines the ability of the RGM to calculate scattering observables with the accurate use of realistic NN interactions in the No-Core Shell Model (NCSM) to describe the clusters. The interaction between clusters is calculated by considering the interaction of each nucleon in the first cluster with each nucleon of the second through a realistic model. The NCSM uses an average potential derived from the underlying NN interaction in a harmonic oscillator basis. The NCSM results converge to those of an exact calculation provided that enough basis states are used. These calculations are limited both in the cluster excitations and the number of clusters considered, which means that even virtual break-up of the  ${}^3\text{He}$  is not included. This, in turn, may reduce their accuracy.

In contrast to the RGM, two other methods have been developed which explicitly consider all possible interactions between nucleons without regard to clusters. The Pisa group has used the method of Hyperspherical Harmonics (HH) to calculate 3- and 4-nucleon bound-state and scattering observables [Fis06] with realistic potential models. The wave function is divided into two terms, one of which describes the  $p+{}^3\text{He}$  system asymptotically while the other describes the system of four nucleons in the interaction region. The former can be written in terms of the S-matrix, which contains the phase-shifts and mixing parameters as described in Chapter 6, through a partial-wave expansion:

$$\Psi_A^{LSJ\pi J_z} = \sum_{L'S'} \left[ \delta_{LL'} \delta_{SS'} \Omega_{LSJJ_z}^- - S_{LS,L'S'}^J(q) \Omega_{L'S'JJ_z}^+ \right], \quad (2.1)$$

where  $\Omega^-$  is an incoming spherical wave with relative angular momentum  $L$  and total spin  $S$ , and  $\Omega^+$  is an outgoing spherical wave with  $L'$  and  $S'$ .

The “core” wave function, on the other hand, is expanded in the HH basis. This basis is derived from a set of Jacobi coordinates for the system, a suitable choice for which are, as shown in Figure 2.1:

$$\begin{aligned} \vec{x}_{1p} &= \sqrt{\frac{3}{2}} \left( \vec{r}_m - \frac{\vec{r}_i + \vec{r}_j + \vec{r}_k}{3} \right), \\ \vec{x}_{2p} &= \sqrt{\frac{4}{3}} \left( \vec{r}_k - \frac{\vec{r}_i + \vec{r}_j}{2} \right), \\ \vec{x}_{3p} &= \vec{r}_j - \vec{r}_i, \end{aligned} \quad (2.2)$$

where the vectors  $\vec{r}$  are the locations of the nucleons  $i$ ,  $j$ ,  $k$ , and  $m$ , and the subscript  $p$  refers to a given permutation of the particles.

The hyperspherical coordinates are constructed from the Jacobi coordinates, and consist

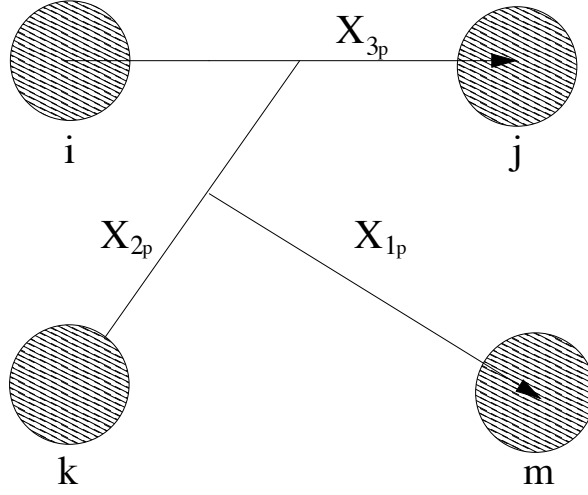


Figure 2.1: Jacobi vectors for four-nucleon calculations. Figure adapted from [Fis03].

of a hyperradius:

$$\rho = \sqrt{x_{1p}^2 + x_{2p}^2 + x_{3p}^2}, \quad (2.3)$$

hyperangles:

$$\begin{aligned} \cos \phi_{2p} &= \frac{x_{2p}}{\sqrt{x_{1p}^2 + x_{2p}^2}}, \\ \cos \phi_{3p} &= \frac{x_{3p}}{\sqrt{x_{1p}^2 + x_{2p}^2 + x_{3p}^2}}, \end{aligned} \quad (2.4)$$

as well as the polar angles for each Jacobi vector.

In these coordinates, the kinetic energy operator depends on the hyperradius in one term and on the angular variables, collectively referred to as  $\Omega$ , in another. The core wavefunction is expanded in the eigenfunctions  $Y_\alpha(\Omega)$  of the angular term, called the hyperspherical harmonic functions:

$$\Psi_C^{LSJ\pi J_z} = \sum_\alpha \sum_{p=1}^{12} u_\alpha(\rho) S_{p\alpha} T_{p\alpha} Y_\alpha(\Omega_p), \quad (2.5)$$

where  $S_\alpha$  and  $T_\alpha$  are the spin and isospin functions, respectively. The coefficients  $u_\alpha(\rho)$  of the expansion carry the hyperradial dependence. The scattering results are obtained by applying



the Kohn variational principle [Koh48] to the complete wavefunction, in which a functional of the Hamiltonian is made stationary with respect to variation of the both the asymptotic scattering-matrix elements and the internal hyperradial coefficients.

The Lisbon group [Del07b, Del08] in contrast, solves the Alt-Grassberger-Sandhas (AGS) [Alt67] equations in momentum space. The method is based on transition operators  $U$ , such as

$$U |\phi\rangle = V |\psi\rangle, \quad (2.6)$$

where  $V$  is the interaction potential,  $|\phi\rangle$  is an asymptotic free-particle state, and  $|\psi\rangle$  is the full wave function. Configurations of the four nucleons are considered where: (1) one nucleon is free and the other three bound, and (2) where two pairs are separately bound, and the transitions from the former configuration in the incoming channel to either configuration in the outgoing channel are considered. Each transition has its own operator satisfying the the AGS equations. The scattering observables are extracted from the 4-body transition matrix  $T$ , which is obtained from the four-body transition operator through numerical integration of the momentum-space integrals:

$$\langle \vec{p}' | T | \vec{p} \rangle = \langle \phi_f | U | \phi_i \rangle. \quad (2.7)$$

The inclusion of the long-range Coulomb interaction is difficult in this scheme and is accomplished by including a screening factor that removes the interaction beyond a radius  $R$ . The final results are obtained with  $R$  large enough to ensure convergence. Larger  $R$  values are required for lower energies, so that these calculations have only been performed above 2 MeV proton energy.



## 3 Polarized Target

---

A new spin-exchange optical pumping (SEOP) spin-polarized  $^3\text{He}$  target, described in detail in [Kat05], was developed for this work. Previous polarized  $^3\text{He}$  targets used in low energy charged particle scattering experiments (e.g. protons below 10 MeV) [Roh68, Bak69, Har71, Lee71, Mil89, All93a], have used metastability-exchange optical pumping (MEOP) [Col63], which operates at about 2 mbar  $^3\text{He}$  pressure. With SEOP [Wal97], in contrast, one operates at a  $^3\text{He}$  pressure of 1-8 bar. Since thicker targets are advantageous for scattering experiments, many polarized  $^3\text{He}$  targets today use SEOP in, for example, high-energy electron [Ant96] and gamma-ray [Kra07] experiments. The low-energy proton beams used in our experiment, however, required that thin foils be used to contain the gaseous  $^3\text{He}$ . This limited gas pressure to 1 bar, and precludes optical pumping of the actual target. This constraint was accommodated in our target, shown in Figure 3.1, by performing the optical pumping in an external polarizer at 8 bar and dispensing 1 bar at a time of polarized  $^3\text{He}$  into the scattering target.

### 3.1 Scattering Target

The design of the target cell used to hold polarized  $^3\text{He}$  during scattering measurement required significant care to minimize the various depolarization mechanisms [Wal97]. In general, magnetic materials must be avoided, since the presence of inhomogeneous magnetic fields would depolarize the gas. Depolarizing surface interactions, which are not well understood, further limit the choice of materials which come into contact with polarized gas. The target cells used in the experiment, one of which is shown in Figure 3.2, were 5.08 cm diameter Pyrex<sup>1</sup> bulbs. Windows were cut along each cell's mid-plane to allow the low-energy charged particles to emerge. Thin foils were epoxied over the windows to contain the gas. Kapton<sup>2</sup> foil and Torr Seal<sup>3</sup> epoxy were selected based on their empirically-determined compatibility

---

<sup>1</sup>Corning Inc.

<sup>2</sup>Free samples provided by DuPont, <http://www.dupont.com/kapton>

<sup>3</sup>Varian Inc., <http://www.varianinc.com>



Figure 3.1: Overview of the polarized target. The scattering chamber containing the sine-theta coil and target cell is on the right-hand side, with the beam coming in from the top of the picture toward the bottom-right. On the left is the polarizer, where optical pumping was performed, on a cart next to the chamber. The two are connected by a PFA fill-tube.

with  $^3\text{He}$  polarization.

Despite optimization for maintaining  $^3\text{He}$  polarization, the polarization  $P$  of gas in any container will decay over time  $t$  according to [Dri05]:

$$P(t) = P_0 e^{-t/T1}, \quad (3.1)$$

where  $P_0$  is the initial polarization and the decay constant  $T1$  is called the “spin-down” time. The effect of optimizing the cell construction was to lengthen  $T1$  as much as possible, and the spin-down time of the cells used in the experiment was about 2 hours. The  $T1$  for target cells or optical pumping cells, discussed below, could be determined simply by making repeated target polarization measurements as a function of time and fitting Equation 3.1 to the data. A target cell example is shown in Figure 5.9.

As discussed in Chapter 5, target cells would eventually begin to leak through either the foil or the epoxy during the experiment. Further use required that the foil and epoxy be removed and new foils epoxied onto the cell. For a metal gas cell, the routine removal of foil and epoxy might be accomplished through the use of a pocket knife, bead-blaster, propane torch, or some combination thereof. This methods are inappropriate for use on a glass cell, and might leave residues which could deteriorate the  $T1$  of the cell. In this work, target cells were prepared for re-gluing by being baked to 538 C in a glassware oven, which is just below the annealing temperature for Pyrex. Afterward, the Kapton and Torr-seal were easily pulled



Figure 3.2: Pyrex target cell with Kapton windows. Part of the NMR coil used for measuring the target polarization is visible between the cell and its Delrin holder. Figure by T. Katabuchi.

off the cell, which was then placed in a sonic cleaner with a solution of Citronox<sup>4</sup> and distilled water.

A uniform magnetic holding field is necessary to define the quantization axis for a sample of polarized  $^3\text{He}$  gas. A Helmholtz coil pair, commonly used to provide uniform magnetic fields, failed to provide the necessary uniformity for this project because of steel structures<sup>5</sup> near the scattering chamber. A “sin-theta” coil, shown in Figure 3.3 was therefore developed, which was easily shielded with mu-metal because of its compact design, to provide a field of 0.7 mT with a fractional gradient of  $10^{-3}/\text{cm}$ . This device, 30 cm long and 7.5 cm in diameter, contained the target cell and actually fit inside the scattering chamber. It consisted of copper rods pressed onto a hollow cylindrical Delrin form, and each rod carried an electric current proportional to the sine of the angle between that rod and a point on the cylinder as viewed from one of its ends, as illustrated in Figure 3.4. Each current was hardware-regulated to within about 0.1% of its programmed value to maintain uniformity. A mu-metal shield around the outside of the coil prevented non-uniform external fields from reaching the interior. The rod currents were controlled by the polarized target computer through National Instruments LabVIEW FieldPoint modules. This approach allowed the magnetic field direction to be conveniently reversed by stepping through an automated sequence of intermediate field orientations. Similarly, the target spins could be aligned easily along either x or y axes transverse to the beam as necessary for measurements of  $A_{yy}$  and  $A_{xx}$ , respectively.

The target polarization was measured using pulsed nuclear magnetic resonance (NMR) as described in [Kat05]. A current pulse through a small coil of wire placed against the

<sup>4</sup>Alconox, Inc. 30 Glenn St. White Plains NY, 10603

<sup>5</sup>beam-stands and reinforcing rods

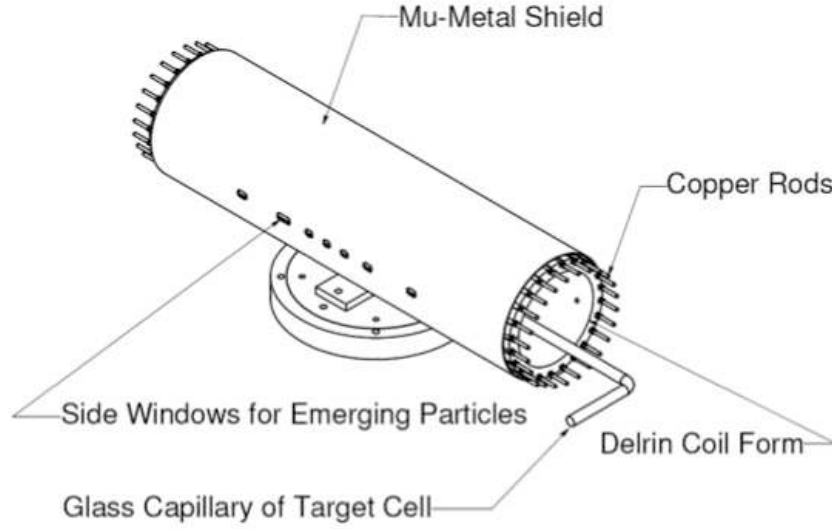


Figure 3.3: The sine-theta coil, shown with a target cell installed. Figure by T. Katabuchi.

cell beam-exit window caused  $^3\text{He}$  spins to precess coherently around the magnetic holding field, provided the pulse was at the Larmour frequency determined by the magnitude of the field. The induced voltage from the coherent precession was detected in the coil, and was proportional to both the  $^3\text{He}$  polarization and the cell pressure. The pressure-corrected signal, therefore, provided a relative polarization measurement which was calibrated by a separate scattering experiment as described in Chapter 5. Similar, though uncalibrated, measurements were made on the optical pumping cells described below.

## 3.2 Optical Pumping

In optical pumping, circularly polarized light is used to pump atoms placed in an external magnetic field into a particular hyperfine state, as illustrated in Figure 3.5. The wavelength of the light is tuned to the desired atomic transition, but its polarization only allows it to excite transitions to magnetic substates that differ from the ground state by  $1 \hbar$ . The excited atoms decay by collisions with  $\text{N}_2$  buffer gas to both ground hyperfine states. The fact that atoms are only pumped out of one ground hyperfine state means that more and more atoms collect in the other, thus creating polarization.

This technique has been exploited to produce nuclear spin-polarization in samples of noble gases since an optically pumped atomic polarization can transfer to nuclear polarization via spin-exchange collisions. MEOP systems optically pump metastable atoms excited by a weak RF discharge, while SEOP optically pump an admixture of alkali metal. In a typical SEOP  $^3\text{He}$  polarizing system, a glass cell is filled with a mixture of  $^3\text{He}$ ,  $\text{N}_2$ , and Rb and placed in

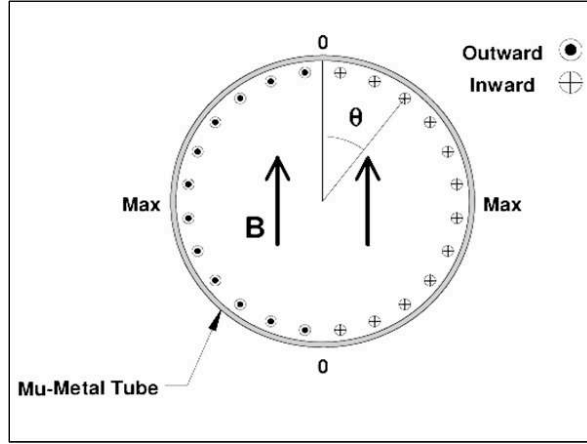


Figure 3.4: Schematic view of the sine-theta coil send end-on. The current in each rod is proportional to the sine of the angle from the intended magnetic field direction. Figure by T. Katabuchi.

the uniform magnetic field of a pair of Helmholtz coils. Circularly polarized laser light at 795 nm illuminates the cell and performs the optical pumping while the cell temperature is kept high enough to ensure sufficient Rb in the vapor phase.

In practice, the accumulation of  $^3\text{He}$  polarization  $p$  takes hours and saturates below unity according to:

$$p(t) = A \left( 1 - e^{(-t/\tau)} \right), \quad (3.2)$$

where  $t$  is time,  $A$  is the saturation polarization, and  $\tau$  is the “spin-up” time for the system. These limitations result from both the inherently small size of the spin-exchange cross-section and the environmentally dependent loss of accumulated  $^3\text{He}$  polarization. Depolarization mechanisms include the surface and magnetic gradient interactions discussed above, as well as dipole-dipole interactions between  $^3\text{He}$  nuclei and spin-destruction collisions between Rb and  $^3\text{He}$  [Wal97]. The typical parameters of 8 atm cell pressure and 180 C temperature reflect a balance between increasing the efficiency of optical pumping and minimizing these depolarization mechanisms [Dri05].

### 3.3 Optical Pumping Cells

The optical pumping cells used in the experiment were spherical bulbs 7.62 cm in diameter, as shown in Figure 3.6 and were made of either Ge-180 or Pyrex glass. A pneumatically-actuated anodized aluminum valve, specially ordered from Swagelok<sup>6</sup> by Amersham Health, sealed each cell, with a several-inch capillary between the valve and cell to minimize depolar-

---

<sup>6</sup><http://www.swagelok.com>

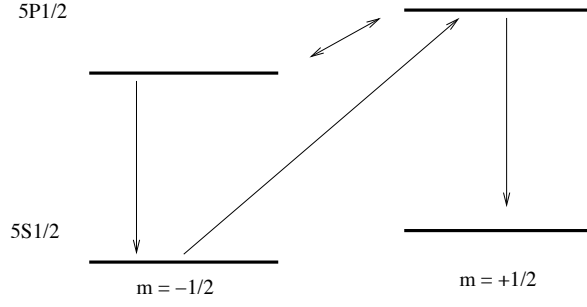


Figure 3.5: Atomic levels in Rb relevant to optical pumping. Circularly polarized light tuned to the D1 ( $5S_{1/2}$  to  $5P_{1/2}$ ) transition excites electrons from only one magnetic substate. The excited electrons decay to either substate through collisions with  $N_2$  buffer gas, but the population in the “pumped” state is depleted over time, producing polarization.



Figure 3.6: An optical pumping cell. Photo by A. Couture.

ization. The sharp bend in the capillary was made necessary by the tight constraints inside the polarizer solenoid.

The optical pumping cells were loaded with either Rb or a mixture of Rb and K. Though the intended Rb/K ratio was 1:10, the cells used in the experiment actually contained an estimated 1:2 mix [Cou06]. The admixture of K into the “hybrid” or “mixed-metal” cells decreased the “spin-up” time necessary for the  $^3\text{He}$  polarization to saturate by taking advantage of K’s larger cross-section for spin-exchange with  $^3\text{He}$  [Bab03]. Thus, Rb is optically pumped and spin-exchanges with K, which in turn spin-exchanges with  $^3\text{He}$ . Rb is retained in this scheme because there are readily available lasers with output at its 795 nm D1 line, and it has reasonable separation of its D1 and D2 lines [Cou06]. Figure 3.7 shows a spin-up curve for a Rb and a Rb/K cell. In practice, the time spent repolarizing gas during an experiment was about 24 hours for a Rb cell and about 12 hours for a mixed-metal cell.



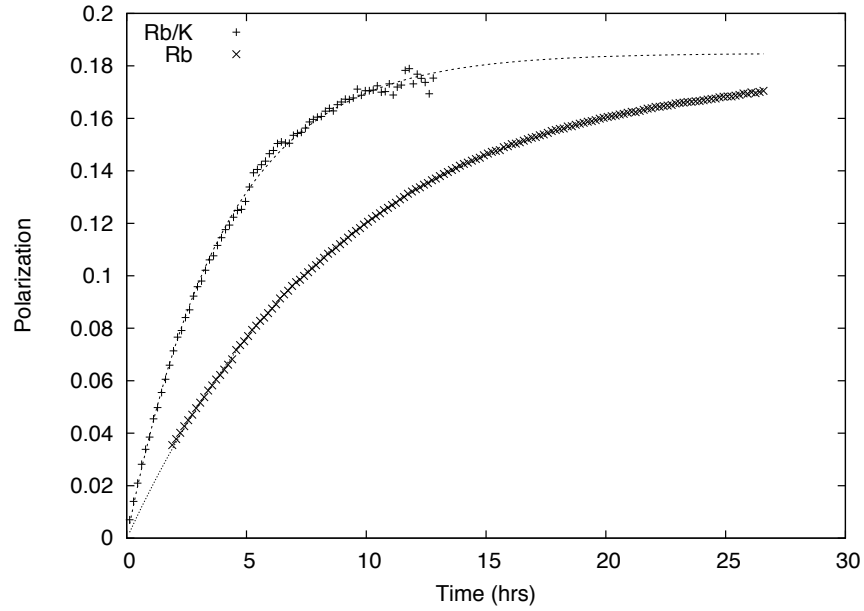


Figure 3.7: Accumulation of  $^3\text{He}$  polarization in two optical pumping cells, one of which contains Rb while the other contains Rb and K. The points are relative NMR polarization measurements, and the curves are fits of Equation 3.2 to the points. Because the NMR calibrations of pumping cells varied considerably, the vertical scale was set for each plot so that its saturated value was equal to the polarization initially dispensed to a calibrated target cell. The “spin-up” times were about 9 hours for the Rb cell and about 4 hours for the Rb/K cell.



Figure 3.8: Alex Couture, whose shoulder is visible in the upper left, filling optical pumping cells with alkali metal. The cells are shown with the bakeout oven lowered so that the torch can be used to move (“chase”) the metal down the glass tubes from a retort located out of the picture on the left. The manifold used for evacuation and purging with  $N_2$  is visible in the background toward the right. Photo by A. Couture.

The original pumping cell was prepared by Amersham Health<sup>7</sup>, and was used for data-taking until it was accidentally destroyed after Rb blocked its capillary. Replacement cells were loaded [Cou06] with alkali in a system designed to allow the cells, which were attached to a glass manifold, to be baked at 400 C for several days while they were evacuated to  $10^{-8}$  Torr. A turbo-pump backed by a diaphragm pump was used in order to eliminate the risk of introducing hydrocarbons. The alkali metal ampoules were introduced into the manifold before pumping, and during the bakeout were “distilled” by heating with an oxygen-methane torch. After the bake-out was complete, the alkali were “chased” with the torch into the pumping cells, as shown in Figure 3.8

The optical cell performances are summarized in Table 3.1. Several of the cells were unusable because of very short T1 times or because they wouldn’t fit into the oven. None of the replacement cells quite matched the T1 and saturation polarization of the original, and many of their performances degraded over time. Sadly, two of the usable cells were damaged when the oven temperature control failed, while another was destroyed by a malfunction of the computer valve-control. The mixed-metal cells had generally shorter T1 times than the Rb cells.

Interestingly, one cell’s T1 and polarization depended on how it was oriented in the solenoid. This apparent magnetization could be “degaussed” by connecting the solenoid to AC power through a variac and increasing and decreasing the current. Similar phenomena were reported for Pyrex cells in [Jac01], and were attributed to magnetic domains in the glass.

---

<sup>7</sup>2500 Meridian Parkway, Suite 150 Durham, NC 27713

Table 3.1: Performance and fate of the optical pumping cells used in this work. The amount of information on each cell varies, since those cells with a poor T1 time were never installed on the polarizer, while others would not physically fit into the solenoid. Some cells were accidentally destroyed, while the valves of some poorly performing cells were deliberately removed for use on new pumping cells.

Cell	Date Filled	Glass	Alkali	Relative Polarization (mV)	T1 (hrs.)	Fate
Original		GE-180	Rb	3200	36	Blockage Accident
Big Rb	7/05	Pyrex	Rb	?	6.4	Destroyed for valve
Little Rb (2C)	7/05	Pyrex	Rb	1800-2200	15	Oven failure
?	4/06	GE-180	Rb	?	33, 14	Valve board failure
1A	4/06	Pyrex	Rb	1200-3500	26	Oven failure, extant
3E	10/06	Pyrex	Rb/K	?	3	Extant
4P	10/06	Pyrex	Rb/K	?	5	Destroyed for valve
5P	10/06	GE-180	Rb/K	?	?	Destroyed for valve
6C	10/06	GE-180	Rb/K	3700	15	Destroyed on install
7Q	2/07	GE-180	Rb/K	?	?	Destroyed on install
8C	2/07	GE-180	Rb/K	1800, 1300	6	RTD failure, extant
9Q	3/07	GE-180	Rb/K	1700, 1000	33, 25	Extant
10P	3/07	GE-180	Rb/K	?	20	Destroyed on install

### 3.4 Polarizer

When actually used for data-taking, an optical pumping cell was placed in a gypsum oven, with the capillary and valve emerging from the side to connect to the gas-handling manifold. About 60 W of laser light from an Optopower<sup>8</sup> system of diode arrays tuned to the Rb D1 absorption line was fiber-optically coupled to the polarizer. The unpolarized light emerging from the fiber-optic was split into separate linear polarization states, each of which was circularly polarized with quarter-wave plates before passing down into the oven. The oven temperature was computer regulated by blowing laboratory compressed air into it whenever the temperature, measured with an RTD, exceeded a setpoint. The oven was located inside a mu-metal shielded solenoid, 29.4 cm in diameter and about 1m in height, to provide the 0.7 mT magnetic field. This location imposed strict constraints on the dimensions of the pumping cells, and care was required to accomodate the oven, with its electrical and air-cooling connections, as well as the gas-handling apparatus described below, inside the solenoid. A schematic of the polarizer is shown in Figure 3.9.

Gas-handling systems, including pneumatically-actuated valves operated by the target computer using LabVIEW, were used to perform a variety of tasks including charging the optical pumping cells with unpolarized <sup>3</sup>He, dispensing 1 atm of polaried gas to the target cell, re-

<sup>8</sup>Formerly of 3321 E. Global Loop Tuscon, AZ 85706

claiming depolarized gas from the target cell, and purifying reclaimed  $^3\text{He}$  in preparation for recharging the pumping cell. The pumping cell was filled with 8 bar of unpolarized  $^3\text{He}$  mixed with about 50 Torr of  $\text{N}_2$  using a rubber membrane stretched across the middle of a spherical plastic cavity. The diaphragm could be “inhaled” or “exhaled” by alternately connecting high-pressure  $\text{N}_2$  or a mechanical pump to the lower cavity portion. About 2 bar of gas in the upper cavity portion in the inhaled position would be compressed to 8 bar in the exhaled position. An aluminum manifold connected this “balloon pump” to the pumping cell. Polarized gas was dispensed to the target cell by first equalizing pressure between the pumping cell and that manifold, and then equalizing pressure between the manifold and the target cell, which was connected by a perfluoroalkoxy (PFA)<sup>9</sup> fill tube. An external manifold which included a oxygen getter, a liquid-nitrogen trap, and an oil-less diaphragm pump was used to remove impurities from gas reclaimed from the target. The entire system had to be leak-tight, since the presence of paramagnetic  $\text{O}_2$  was poisonous to the  $^3\text{He}$  polarization.

### 3.5 Narrowed Laser

Some fraction of the broadband laser light used for optical pumping is wasted by being outside the range of wavelengths where absorption by Rb occurs, as shown in Figure 3.10. Thus, concentrating laser power into a smaller bandwidth would put more power into the actual absorption. Motivated by the promising results of [Cha03], a frequency-narrowed laser system was developed as an alternative to the broadband laser for optical pumping [Arn06]. A nominally 50 W Quintessence<sup>10</sup> diode bar array was placed in an external Littrow cavity [Dua95], in which the first-order diffracted light from a diffraction grating is used for feedback. The grating used in this work had 2400 lines/mm. A system of lenses and mirrors, together with the laser and diffraction grating, was mounted on a standard optical table which fit on top of the optical polarizer to direct narrowed light onto the pumping cell. Narrowed light output was typically 0.3 nm FWHM and 30 W. The frequency of the narrowed light was tuned to 795 nm by controlling the temperature of the water-cooled diode array and by adjusting the orientation of the diffraction grating.

The resulting  $^3\text{He}$  polarization was typically comparable to, though somewhat smaller than, that achieved with the broadband laser. In practice, the optics table, which was magnetic, had to be removed from the polarizer for dispensing polarized gas to the target, and using the 30 W narrowed laser instead of the 60 W broadband laser required the use of a “hot-watt” resistive heater to keep the oven in the temperature range of 180-220 C necessary for optical pumping. Given the somewhat inferior performance of this system, together with the inconveniences of its use, the broadband laser was used for the majority of data-taking.

---

<sup>9</sup>Obtained from Whitey Co. 318 Bishop Rd. Highland Heights, OH 44143

<sup>10</sup><http://www.qpclasers.com>

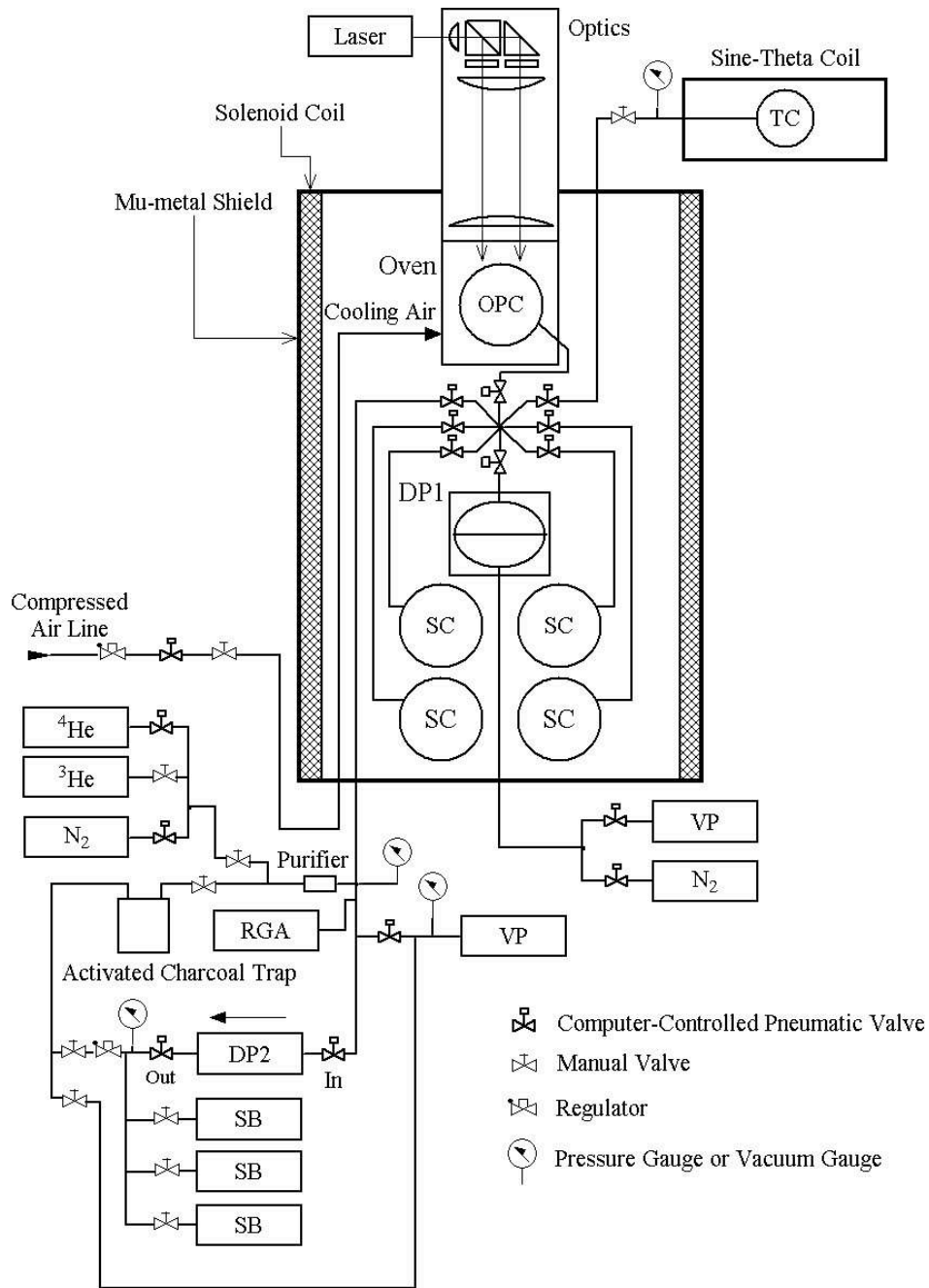


Figure 3.9: Schematic of the polarizer, not to scale. Computer-controlled valves were used to dispense polarized  $^3\text{He}$  from the pumping cell (OPC) inside the solenoid to the target cell (TC) through an intermediate manifold. A “balloon pump” (DP1) was used to compress unpolarized  $^3\text{He}$  to 8 atm when loaded into OPC. A diaphragm pump (DP2) was used to move depolarized  $^3\text{He}$  from TC to storage bottles (SB), as well as to cycle reclaimed gas through a charcoal trap and purifier to remove impurities. Figure by T. Katabuchi.

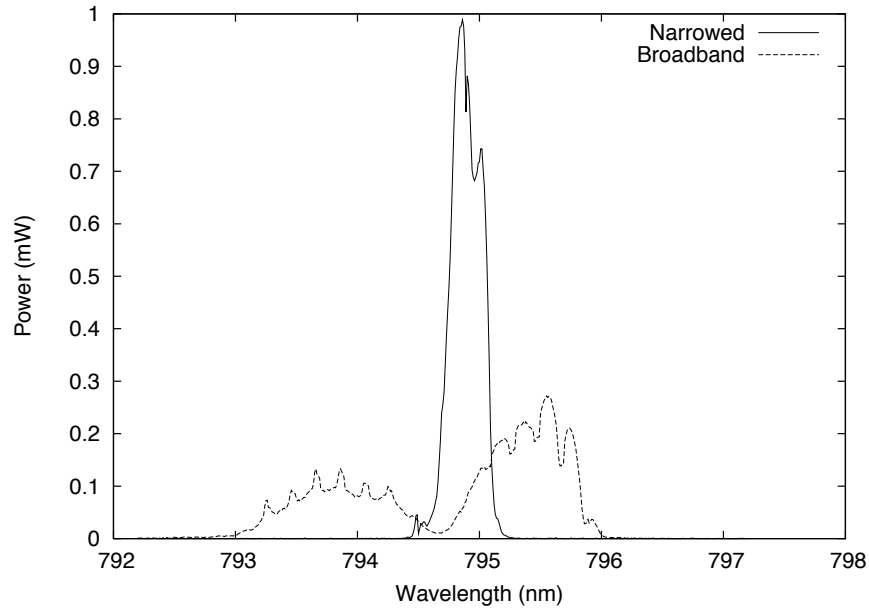


Figure 3.10: The output of the narrowed laser is plotted as a function of wavelength as determined by a high-resolution spectrometer. For comparison, the spectrum of light from the broadband system is shown after traversing the cell during optical pumping. All the power in this latter plot is wasted in the sense that it is outside of the Rb absorption, which is evident as the “dip”. In contrast, the power from the narrowed laser is concentrated in a range a wavelengths comparable to the absorption, so that very little narrowed light would be wasted. Figure adapted from [Arn06].

### 3.6 Performance Summary

The UNC polarized  $^3\text{He}$  was, in contrast to previous polarized targets for low-energy charged-particle scattering, a high-pressure (1 bar) target whose polarization could be clearly determined. The polarization of the gas dispensed to the target cell varied from 30% using the original optical pumping cell to as low as 10% using various replacement cells, including mixed-metal ones. Unlike systems polarized by continuous optical pumping, the target’s “duty cycle” included time, which was about 24 hours when Rb cells were used and about 12 hours for mixed-metal cells, to polarize new gas. This was generally necessary after 2 or 3 days of data-taking. As described in the remainder of this thesis, the target was used successfully to measure  $p + ^3\text{He}$  spin-correlation coefficients between 2 and 6 MeV.

Successful use of the target required the simultaneous operation of its many components, so that significant time during the experiment was lost to system failures. The frequent, and mostly beam-induced, failure of the target cell foil or epoxy was the largest culprit, since a separate alpha-scattering experiment had to be mounted for each recalibration, as discussed in Chapter 5. Failure of the various aspects of the computer control, including DAQ cards and Fieldpoint modules, as well as leaks in the various gas-handling connections, also contributed.

The compact, enclosed design of the polarizer was convenient for use in the target room, since no further precautions were necessary against the Class 4 laser. Efforts to replace the optical pumping cell, however, were hampered by the need to lift out of the solenoid and partially disassemble the polarizer systems. This was a laborious procedure involving significant wear on the components. Even such mundane tasks as ensuring that the pumping cell was fully illuminated by laser light during optical pumping were difficult. In short, significant “tinkering” was necessary on a system that was not designed to be easily modified.





## 4 Observables

---

This chapter describes the measurement of angular distributions of the beam and target analyzing powers,  $A_{y0}$  and  $A_{0y}$ , and spin-correlation coefficients  $A_{yy}$  and  $A_{xx}$  for protons elastically scattered from  $^3\text{He}$  at 5 proton energies between 2 and 6 MeV. These observables determine how the scattering at a given energy and angle depends on the spins of the beam and target. The precise definition of the observables and the methods used to measure them are discussed in detail.

### 4.1 Spin- $\frac{1}{2}$ Formalism

#### 4.1.1 One Particle

The spin state of a spin- $\frac{1}{2}$  particle can be described by a two-component spinor

$$\chi = \begin{pmatrix} a \\ b \end{pmatrix}, \quad (4.1)$$

where  $a$  and  $b$  represent the probability of the projection along a given axis being measured as “up” or “down”, respectively [Ohl72]. The expectation value for a given observable, represented by operator  $\Omega$ , is obtained from the spinor,

$$\langle \Omega \rangle = \chi^\dagger \Omega \chi. \quad (4.2)$$

We can also use a density matrix to describe the spin state,

$$\rho = \chi \chi^\dagger = \begin{pmatrix} |a|^2 & ab^* \\ a^*b & |b|^2 \end{pmatrix}. \quad (4.3)$$

This makes the expectation value of an operator  $\Omega$

$$\langle \Omega \rangle = \text{Tr} \rho \Omega. \quad (4.4)$$

The density matrix formalism has the advantage of immediately including the description of an *ensemble* of particles, since a density matrix for the ensemble can easily be constructed,

$$\rho = \begin{pmatrix} \sum |a|^2 & \sum ab^* \\ \sum a^*b & \sum |b|^2 \end{pmatrix}. \quad (4.5)$$

The ensemble average of an operator  $\Omega$  is likewise given by

$$\langle \Omega \rangle = \text{Tr} \rho \Omega, \quad (4.6)$$

and the total number of particles is given by

$$I = \text{Tr} \rho. \quad (4.7)$$

The polarization of the ensemble with respect to a given axis is given by the ensemble average of that component of the spin

$$P_i = \text{Tr} \rho \sigma_i. \quad (4.8)$$

Polarization varies between -1, when all particles are spin “down”, to +1, when all are spin “up”. A value of 0 indicates equal numbers of up and down.

For later use, the density matrix can be expanded in the basis of the Pauli spin matrices

$$\rho = \frac{1}{2} \sum_{j=0}^3 p_j \sigma_j, \quad (4.9)$$

where  $p_0 \sigma_0$  is defined as the identity matrix.

#### 4.1.2 Two Particles

In the usual spin-coupling scheme, the state of the combined system of two particles can be described in either the basis of the projections of the individual spins or the basis of the total spin and its projection. The density matrix formed from a spinor in the former basis is the same as that obtained from the direct product of the density matrices for the beam and target, and is the one used in the following. Using the expansion 4.9:

$$\rho = \frac{1}{4} \sum_{j,k=0}^3 p_j p_k^T \sigma_j \otimes \sigma_k^T. \quad (4.10)$$

The beam and target polarizations are obtained from the expectation values of the operators  $\sigma_j \otimes 1$  and  $1 \otimes \sigma_k^T$ , respectively, where 1 is the identity matrix.

## 4.2 Observables

The asymptotic wave-function for the elastic scattering of particles with spin is [Got66]:

$$\psi \sim \left( e^{i\vec{k}\cdot\vec{r}} + \frac{e^{ikr}}{r} M(E, \theta, \phi) \right) \chi = \psi_{inc} + \psi_{scatt}, \quad (4.11)$$

where

$$\psi_{inc} = e^{i\vec{k}\cdot\vec{r}} \chi$$

is the incoming plane wave describing the incoming beam and

$$\psi_{scatt} = \frac{e^{ikr}}{r} M(E, \theta, \phi) \chi$$

is the outgoing spherical wave that describes the outgoing particles. Both the overall magnitude and anisotropy with respect to angles  $\theta$  and  $\phi$  of this spherical wave are described by the matrix M.

The fundamental observable for a scattering experiment is the cross-section, which is defined as the ratio of the number of particles scattered into a given element of solid angle to the number of incident particles per area. In terms of particle flux  $\vec{j}$ :

$$\frac{d\sigma}{d\Omega} = \frac{\vec{j}^{scatt} \cdot d\vec{A}}{j^{inc}} = \frac{\vec{j}^{scatt} \cdot \hat{r} r^2 d\Omega}{j^{inc}}$$

Using 4.11 and ignoring interference between  $\psi_{inc}$  and  $\psi_{scatt}$ , we obtain:

$$\frac{d\sigma}{d\Omega} (\chi_i \rightarrow \chi_f) = |M_{fi}|^2, \quad (4.12)$$

where  $\frac{d\sigma}{d\Omega} (\chi_i \rightarrow \chi_f)$  is the cross-section for the transition between particular initial and final states  $\chi_i$  and  $\chi_f$ , respectively. The scattering matrix elements, which are functions of energy and angle, therefore contain all the available information about the scattering. For the scattering of spin-1/2 particles from spin-1/2 particles, as in  $p + {}^3\text{He}$  elastic scattering is,  $\chi$  is a four-component spinor and M is a 4 x 4 matrix.

Equation 4.12 suggests an experiment in which the beam and target are prepared in some polarization state, and then, after the scattering, the final polarization state is fully determined. From an experimental point of view, the latter step requires a second scattering from a known analyzer for both particles, and multiple scattering experiments suffer from low count rates. Fortunately, it is sufficient to determine only the scattered flux when using a polarized beam and target, provided that one can do so for several different initial states. This “spin-correlation” experiment is the type performed for this thesis <sup>1</sup>.

---

<sup>1</sup>A different set of experiments, called “spin-transfer” experiments, are also sufficient to determine the

The differential cross-section for such an experiment is the cross-section for scattering into any final state, and is given by the sum of the cross-sections for transition from each available initial state weighted by the fraction of the ensemble in that initial state:

$$\frac{d\sigma}{d\Omega} = \sum_{i,f} |M_{fi}|^2 \rho_{ii},$$

or, more generally,

$$\frac{d\sigma}{d\Omega} = \text{Tr} M \rho M^\dagger, \quad (4.13)$$

where  $\rho$  is the initial density matrix. Using 4.10, we can see how the scattered yield depends on each combination of each component of beam and target spin,

$$\frac{d\sigma}{d\Omega} = \frac{d\sigma_0}{d\Omega}(\theta) \frac{\sum p_j p_k^T \text{Tr} M \sigma_j \otimes \sigma_k^T M^\dagger}{\text{Tr} M M^\dagger},$$

where the T superscript refers to the target. The coefficients that control that dependence are

$$A_{jk}(\theta) = \frac{\text{Tr} M \sigma_j \otimes \sigma_k^T M^\dagger}{\text{Tr} M M^\dagger}, \quad (4.14)$$

so that the cross-section can be rewritten

$$\frac{d\sigma}{d\Omega} = \frac{d\sigma_0}{d\Omega}(\theta) \sum p_j p_k^T A_{jk}(\theta), \quad (4.15)$$

where  $\sigma_0$  is the unpolarized cross-section.

This expression must be referred to a specific coordinate system in order to fix the meaning of the observables  $A_{jk}$ . The Madison Convention [Bar71] establishes the coordinate system for polarized scattering experiments. The z axis is along the incoming beam direction, the y axis is in the direction of the incoming beam direction crossed with the direction of scattering, and the x axis is in the direction which makes the system right-handed<sup>2</sup>. The constraints of time-reversal invariance, parity conservation, and rotational invariance make many of the coefficients identically zero, reducing the expression to

$$I = I_0(1 \pm p_y A_{y0} \pm p_y^T A_{0y} + p_x p_x^T A_{xx} \pm p_z p_x^T A_{zx} + p_y p_y^T A_{yy} + p_z p_z^T A_{zz} \pm p_x p_z^T A_{xz}). \quad (4.16)$$

The  $\pm$  refers to scattering to the left or right of the beam, respectively, as necessary to preserve invariance under rotation about the z axis.

---

scattering elements. In spin-transfer experiments, an unpolarized beam is scattered from an unpolarized target, and the resulting polarization for one of the scattered particles is measured. This type of experiment suffers from requiring two scatterings, as described above.

<sup>2</sup>This coordinate system has the curious property of having its x and y axes point in different directions for particles which scatter to the left or right of the beam. The y axis, for instance, points “up” in the laboratory when particles are scattered to the left of the beam, while it points “down” when the scattering is to the right. In this way, left/right scattering is explicitly equated with “flipping” the spin directions.

### 4.3 Detector Yields

The number of particles detected by a detector at a scattering angle  $\theta$  from a beam incident on a gas cell target is proportional to the cross-section,

$$N = \epsilon b p G I. \quad (4.17)$$

The experimental factors are  $b$ , the number of incident beam particles,  $p$ , the target pressure, the detector efficiency  $\epsilon$  which describes what fraction of particles entering the detector are actually detected, and the detector “G-factor” [Sil59]. The G-factor describes both the geometrical effects of the detector collimation and the size of the target.

The detector yield as a function of arbitrary spin orientations is therefore

$$N = \epsilon G b p I_0 (1 \pm p_y A_{y0} \pm p_y^T A_{0y} + p_x p_x^T A_{xx} \pm p_z p_x^T A_{zx} + p_y p_y^T A_{yy} + p_z p_z^T A_{zz} \pm p_x p_z^T A_{xz}). \quad (4.18)$$

For left and right detectors, the yields for different combinations of the beam and target spin orientations as a function of the average polarizations are

$$\begin{aligned} L \uparrow\uparrow &= \epsilon_L G_L b_{\uparrow\uparrow} p_{\uparrow\uparrow} I_0 (1 + p_y A_{y0} + p_y^T A_{0y} + p_y p_y^T A_{yy}) \\ L \uparrow\downarrow &= \epsilon_L G_L b_{\uparrow\downarrow} p_{\uparrow\downarrow} I_0 (1 + p_y A_{y0} - p_y^T A_{0y} - p_y p_y^T A_{yy}) \\ L \downarrow\uparrow &= \epsilon_L G_L b_{\downarrow\uparrow} p_{\downarrow\uparrow} I_0 (1 - p_y A_{y0} + p_y^T A_{0y} - p_y p_y^T A_{yy}) \\ L \downarrow\downarrow &= \epsilon_L G_L b_{\downarrow\downarrow} p_{\downarrow\downarrow} I_0 (1 - p_y A_{y0} - p_y^T A_{0y} + p_y p_y^T A_{yy}) \\ \\ R \uparrow\uparrow &= \epsilon_R G_R b_{\uparrow\uparrow} p_{\uparrow\uparrow} I_0 (1 - p_y A_{y0} - p_y^T A_{0y} + p_y p_y^T A_{yy}) \\ R \uparrow\downarrow &= \epsilon_R G_R b_{\uparrow\downarrow} p_{\uparrow\downarrow} I_0 (1 - p_y A_{y0} + p_y^T A_{0y} - p_y p_y^T A_{yy}) \\ R \downarrow\uparrow &= \epsilon_R G_R b_{\downarrow\uparrow} p_{\downarrow\uparrow} I_0 (1 + p_y A_{y0} - p_y^T A_{0y} - p_y p_y^T A_{yy}) \\ R \downarrow\downarrow &= \epsilon_R G_R b_{\downarrow\downarrow} p_{\downarrow\downarrow} I_0 (1 + p_y A_{y0} + p_y^T A_{0y} + p_y p_y^T A_{yy}), \end{aligned}$$

Using these yields, we form the following cross-ratios:

$$\begin{aligned} X_1 &= \sqrt{\left(\frac{L' \uparrow\uparrow + L' \uparrow\downarrow}{L' \downarrow\uparrow + L' \downarrow\downarrow}\right) \left(\frac{R' \downarrow\uparrow + R' \downarrow\downarrow}{R' \uparrow\uparrow + R' \uparrow\downarrow}\right)} = \frac{1 + p_y A_{y0}}{1 - p_y A_{y0}} \\ X_2 &= \sqrt{\left(\frac{L' \uparrow\uparrow + L' \downarrow\uparrow}{L' \uparrow\downarrow + L' \downarrow\downarrow}\right) \left(\frac{R' \uparrow\downarrow + R' \downarrow\downarrow}{R' \uparrow\uparrow + R' \downarrow\uparrow}\right)} = \frac{1 + p_y^T A_{0y}}{1 - p_y^T A_{0y}} \\ X_3 &= \sqrt{\left(\frac{L' \uparrow\uparrow + L' \downarrow\downarrow}{L' \uparrow\downarrow + L' \downarrow\uparrow}\right) \left(\frac{R' \uparrow\uparrow + R' \downarrow\downarrow}{R' \uparrow\downarrow + R' \downarrow\uparrow}\right)} = \frac{1 + p_y p_y^T A_{yy}}{1 - p_y p_y^T A_{yy}}, \end{aligned}$$

where the primes indicate that we have normalized the yields to the appropriate b and p. The observables are therefore

$$A_{y0} = \frac{1}{p_y} \left( \frac{X_1 - 1}{X_1 + 1} \right) \quad (4.19)$$

$$A_{0y} = \frac{1}{p_y^T} \left( \frac{X_2 - 1}{X_2 + 1} \right) \quad (4.20)$$

$$A_{yy} = \frac{1}{p_y p_y^T} \left( \frac{X_3 - 1}{X_3 + 1} \right). \quad (4.21)$$

Similarly, when the beam and target spins are aligned along the x-axis,

$$A_{xx} = \frac{1}{p_x p_x^T} \frac{X_3 - 1}{X_3 + 1}. \quad (4.22)$$

If either the beam or target is unpolarized, only one analyzing power will be non-zero, and the expression 4.19 reduces to the usual cross-ratio expression for analyzing powers,

$$A_y = \frac{\sqrt{\frac{L'\uparrow R'\downarrow}{L'\downarrow R'\uparrow}} - 1}{\sqrt{\frac{L'\uparrow R'\downarrow}{L'\downarrow R'\uparrow}} + 1}. \quad (4.23)$$

The same is true for the scattering of spin-1/2 particles from spin-0 particles.

## 5 Data Collection and Analysis

---

Spin-correlation coefficients for  $p+{}^3\text{He}$  scattering were measured according to equations 4.19 through 4.22 using a polarized beam and target. To better understand systematic effects, additional measurements were made of both unpolarized target instrumental asymmetries with either polarized or unpolarized proton beams and the observable  $A_{0y}$  with an unpolarized proton beam. Several other scattering experiments were made in support of these measurements. Briefly, a target cell calibration point was found by the location of an absolute minimum in  $\alpha+{}^3\text{He}$  scattering, frequent target cell calibrations were made using that scattering, the Wein filter spin-precession of the polarized beam was calibrated by maximizing the  $p+{}^4\text{He}$  asymmetry, and beam polarization was measured with that scattering during data-taking. The performance and analysis of all these measurements are described in detail in this chapter.

### 5.1 Experimental Set-Up

The measurements were performed using the Triangle Universities Nuclear Laboratory (TUNL) tandem accelerator. Accelerated beams were directed by an analyzing magnet down the  $52^\circ$  beam line to the 62cm scattering chamber, where the Pyrex target cell was installed inside the sin-theta coil as described in the Chapter 3. The chamber set-up is illustrated in Figure 5.1. Beam intensity on the target cell was initially limited to 100nA to avoid damaging the Kapton entrance foils. Experience with failure of the epoxy, especially on the beam exit foils, prompted us to further limit the intensity to 50nA. Even with this reduction, cells lasted no more than a few days.

Proton beam measurements were taken at 5 energies below 6 MeV which overlap the data of both [Fis06] and [All93a]. Analyzing magnet settings were determined according to the calibration of [Fis03], and the uncertainty in the beam energy was calculated by propagating the calibration uncertainty through equation B.1 of [Fis03]. Energy loss in the Kapton foils and  ${}^3\text{He}$  gas was modeled with TRIM [Zie85], and the results are summarized in Table 5.1.

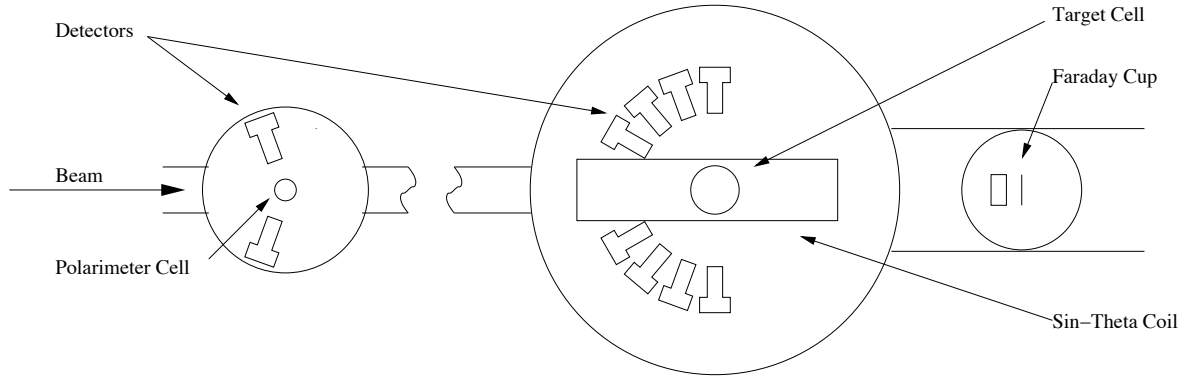


Figure 5.1: Diagram of Chamber Setup. The polarimeter chamber could be configured with the detectors either horizontal, as shown, or vertical. The polarimeter cell was removed from the beam during data-taking to allow beam to reach the target chamber.

The beam energy was set high enough to offset energy loss, so that the proton energy at the cell's center was as desired. The bombarding energies for data taken with different thickness entrance foils were slightly different, and the average value, weighted by the error-bars according to Equation 5.25, was adopted. The uncertainty in the TRIM stopping powers was estimated by comparison with experimental stopping powers [Sri08], as summarized in Table 5.2. A precision of 10% was assigned to cases where no data were present in the relevant energy range.

Polarized beam and target spins were reversed frequently. The beam spin was reversed during data-taking at either 1 or 10 Hz in the sequence  $+ - + - + -$ , where “+” means “spin-up” and “-” means “spin-down”. The target spin was reversed less frequently, since it required a few seconds to reverse the target's magnetic field. Polarized target data was collected in the following sequence: the data were collected for about 2.5 minutes with the target spin in one orientation, an NMR measurement was taken, then the spin was flipped, another NMR was taken, and data collection then proceeded with the spin in the second orientation. The target polarization decayed with a 2-3 hour time constant, so this process was stopped when the gas was judged to be too depolarized, generally after about an hour. At that time the gas was exhausted from the target, the target was flushed with research-grade  $N_2$ , and new polarized gas, called a “shot”, was dispensed to the target cell.

Scattered particles emerging from the target were detected by four pairs of Si detectors (a mix of surface-barrier and ion-implanted), which could be rotated to the desired angle. The available angles were restricted by the windows in the sin-theta coil's mu-metal shield to  $20^\circ$  increments between  $30^\circ$  and  $150^\circ$ . The shield could be moved axially so that the “intermediate” angles offset by  $10^\circ$  were available. The detectors were placed in Al holders and each one had two brass collimators spaced 5cm from each other in an Al “snout”, which restricted the range of scattering angle visible to the detector to  $1.5^\circ$ . Detectors were as close as possible to



Table 5.1: Calculation of target cell bombarding energies for beam which passes first through a Kapton entrance foil and then through the target He gas. The energy at the center of the cell is reported as the bombarding energy. Slightly different bombarding energies which result from the variety of foil thicknesses are averaged together.

Incoming Beam Energy (MeV)	Kapton Entrance Foil Thickness ( $\mu\text{m}$ )	Energy After Entrance Foil (MeV)	Energy at Cell Center (MeV)	Average Energy (MeV)
5.77 $\pm$ 0.04	25.4	5.54 $\pm$ 0.04	5.51 $\pm$ 0.04	5.54 $\pm$ 0.03
5.66 $\pm$ 0.04	7.62	5.59 $\pm$ 0.04	5.56 $\pm$ 0.04	
4.15 $\pm$ 0.03	7.62	4.06 $\pm$ 0.03	4.02 $\pm$ 0.03	4.02 $\pm$ 0.03
3.54 $\pm$ 0.03	25.4	3.19 $\pm$ 0.03	3.15 $\pm$ 0.03	3.15 $\pm$ 0.02
3.31 $\pm$ 0.03	7.62	3.20 $\pm$ 0.02	3.16 $\pm$ 0.02	
3.13 $\pm$ 0.03	17.8	2.86 $\pm$ 0.03	2.81 $\pm$ 0.03	2.77 $\pm$ 0.02
3.13 $\pm$ 0.03	25.4	2.75 $\pm$ 0.03	2.70 $\pm$ 0.03	
2.75 $\pm$ 0.02	25.4	2.33 $\pm$ 0.03	2.27 $\pm$ 0.03	2.28 $\pm$ 0.02
2.48 $\pm$ 0.02	7.62	2.34 $\pm$ 0.02	2.29 $\pm$ 0.02	

Table 5.2: Estimated precision for TRIM stopping powers

Ion	Kapton	Havar	He
proton	7%	5%	3%
$\alpha$	10%	10%	4%

the target without the 30° snout’s touching the sin-theta coil. The distance from the center of the target cell to the front collimators was about 10.2 cm. Beam current on target was measured by a Faraday cup located about 0.5 m behind the target cell, which was suppressed to -100V. Charge went to ground through a current integrator, which produced the beam current integration (BCI) scaler used as a measure of the relative number of beam particles in each spin state.

Signals from each detector were processed and read into a MicroVAX II<sup>1</sup> computer running XSYS, as described in [Fis03]. As in that work, spin-routing bits at the ADC interface were used to route data to different data-areas for different spin-states. The use of a polarized target as well as a polarized beam, however, required allocating more data areas, installing an extra scaler module, and modifying the EVL detector sorting codes. Our use of 8 detectors with 6 ADC modules required using two modules for two pairs of detectors, so that the left and right detectors in the first and fourth detector pairs were each routed through a different module, but the left and right detectors for the second and third pairs went through the same module. A logic module was designed and constructed to sort scalers, which in XSYS is done by enabling and disabling the hardware scaler modules as appropriate. A diagram of the

---

<sup>1</sup>Digital Equipment Corporation, circa 1985

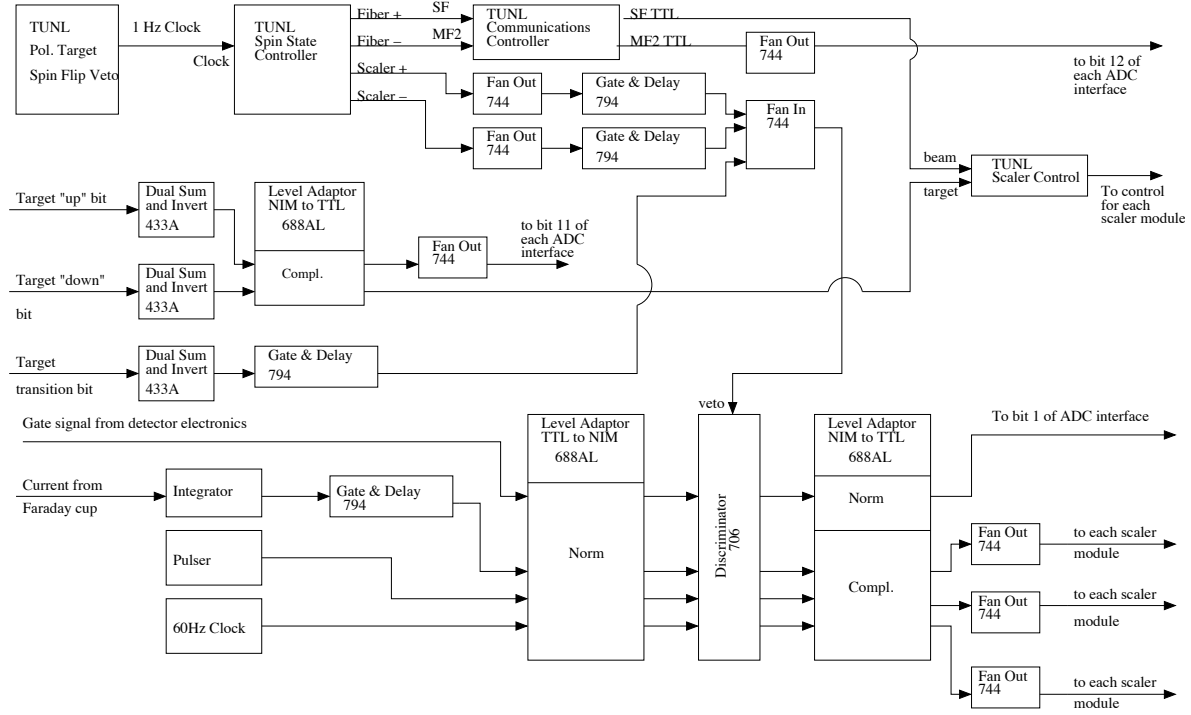


Figure 5.2: Diagram of spin-flip electronics. The scheme is that of [Gei98] with an added signal describing the target spin state.

spin-sorting electronics is given in Figure 5.2.

## 5.2 Spectra

Spectra obtained from the Si detectors represent histograms of the number of detected particles vs. energy. Typical spectra are shown in Figures 5.3-5.5. The existence of well-defined peaks results from the kinematic determination of the energy of a scattered particle by its mass, its incoming energy, the mass of the target, and the angle of scattering. Knowledge of these factors allows peaks to be identified. The finite width of the peaks is primarily the result of energy straggling in the target. This also causes peak asymmetry, since more energy is lost to straggling by lower-energy particles. The peaks also have a long low-energy tail which arises from scattering on the snout slits.

### 5.2.1 Peak Sums

The number of particles scattered into the detector, then, is determined by the number of counts in the corresponding spectral peak. This was simply accomplished in the many cases like Figure 5.3 by summing the value of all channels within an analysis “gate” set around the

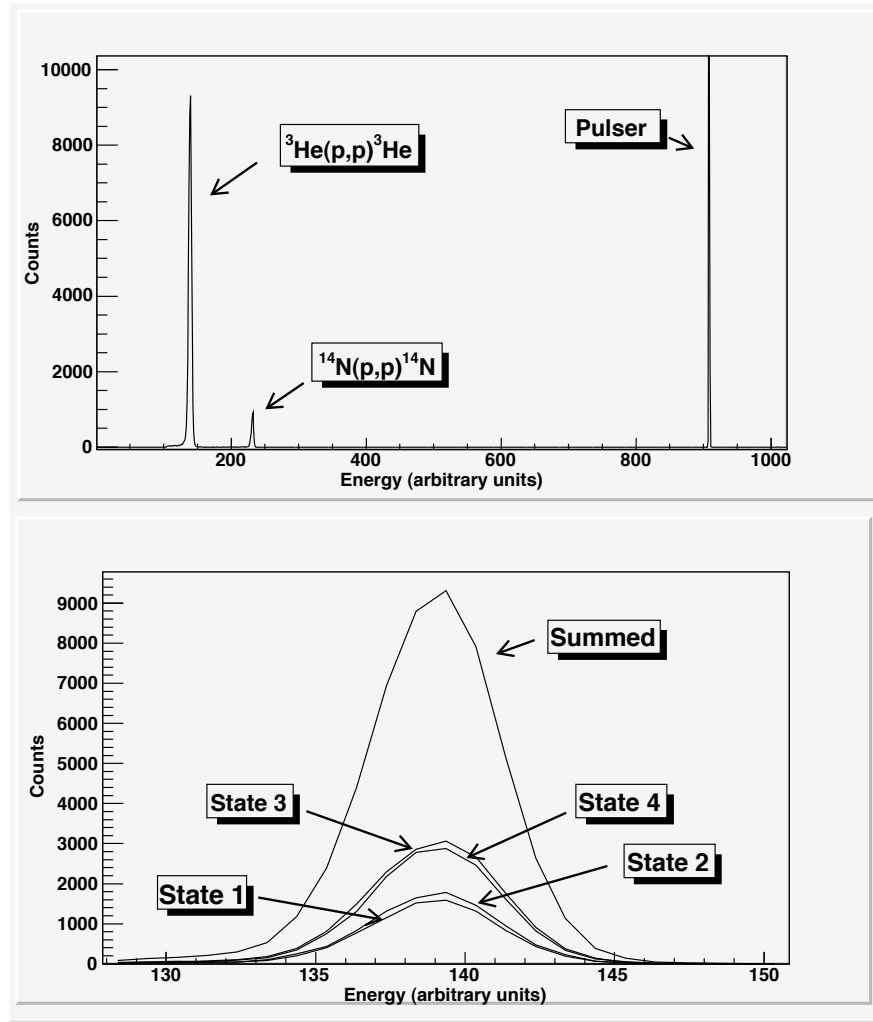


Figure 5.3:  ${}^3\text{He}(p,p){}^3\text{He}$  spectrum taken at 5.54 Mev and  $90^\circ$ . The upper plot shows the summed spectra from all combinations of beam and target spin “up” and “down” over the entire detector energy range. Individual spin states, as well as the summed spectrum, are shown in the lower plot for the  ${}^3\text{He}$  peak.

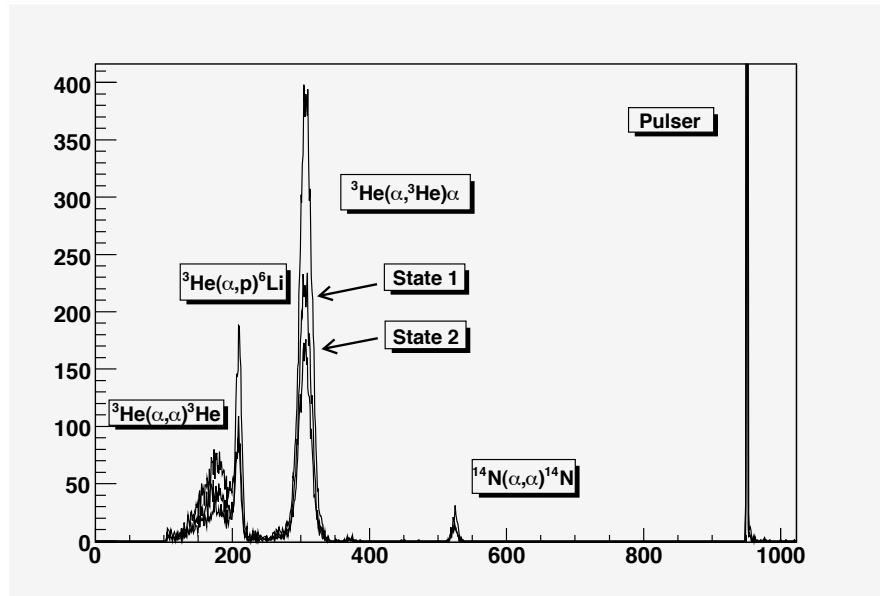


Figure 5.4:  ${}^3\text{He}(\alpha, \alpha){}^3\text{He}$  spectrum at 15.44 MeV and  $45^\circ$ . Individual target spin-states are shown with the summed spectrum

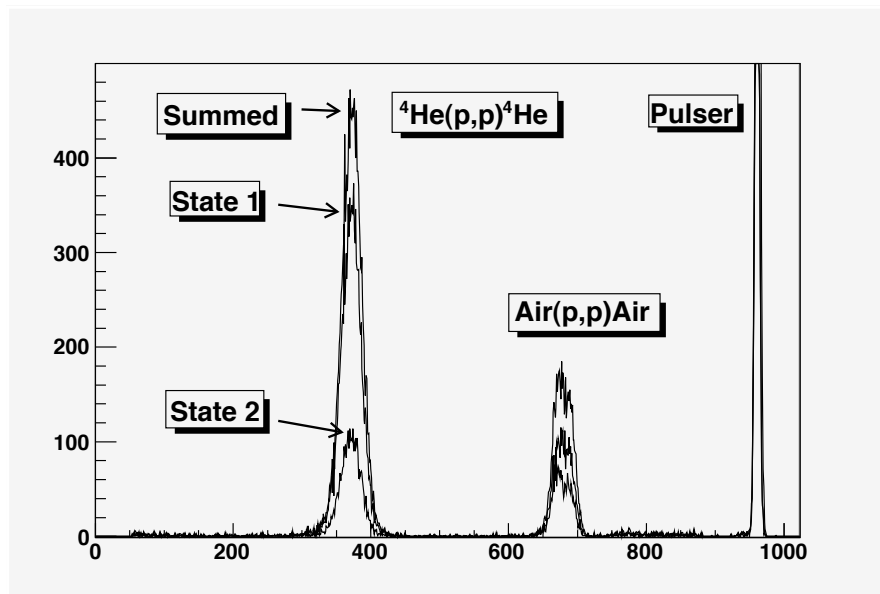


Figure 5.5:  ${}^4\text{He}(p, p){}^4\text{He}$  spectrum taken at 5.54 MeV and  $110^\circ$  in the polarimeter. Individual beam spin states, as well as the summed spectrum, are shown.

peak. Gate sums, scalers, and gate limits were exported from XSYS in text files, which were read into a ROOT script. All further analysis was performed by this script.

Scattering is a random process, so that peak yields are governed by Poisson statistics. The uncertainty in peak area is therefore the square-root of the number of counts. Uncertainties in calculated quantities are determined from uncertainties in peak areas using the standard propagation of error formula [Bev92]. The uncertainty of a function  $f$  of  $n$  independent quantities  $a_i$  is

$$\sigma_f = \sqrt{\sum_{i=0}^n \left( \frac{\partial f}{\partial a_i} \sigma_i \right)^2 + 2 \sum_i^n \sum_{j>i}^n \sigma_{ij}^2 \frac{\partial f}{\partial a_i} \frac{\partial f}{\partial a_j}} \quad (5.1)$$

where the  $\sigma_i^2$  are the variances in the  $a_i$  and the  $\sigma_{ij}^2$  are the covariances between them. The random scattering process insures that there are no correlations between peak yields, so the second term under the radical was often assumed to be zero for this work. When a fitted function was used during analysis, however, correlations between fit parameters were obtained from the error matrix and used in the error propagation.

### 5.2.2 Background

Two types of background had to be subtracted from the number of counts obtained from summing gates. The first was a flat background, which happened either when a pulser was set below the highest energy peak in the spectrum or when protons scattered from the polarimeter cell itself in addition to the  $^4\text{He}$  gas, as in Figure 5.6. The number of background counts,  $N_A$ , inside a gate A of width  $w_A$  set around the peak was estimated from the number of counts  $N_B$  in a gate B of width  $w_B$  set to one side of the peak.

$$N_A = N_B \frac{w_A}{w_B} \quad (5.2)$$

$$\sigma_{N_A} = \sqrt{N_B} \frac{w_A}{w_B} \quad (5.3)$$

Sometimes two background gates were used, one on either side of the peak. When both gates were used, the sums were averaged.

The second type of background occurred when the  $^3\text{He}$  and  $^4\text{He}$  peaks overlapped in chamber spectra at 30° and 40°. The  $^4\text{He}$  gas was sometimes added to the cell to measure beam polarization. Two Gaussian peaks modified to mimic energy-loss were fit to these spectra, as in Figure 5.7.

The functional form for a single Gaussian peak with energy loss as a function of channel number  $x$  was

$$y = Ae^{-\frac{1}{2}((x+\Delta x(x))-x_0)/\sigma)^2}, \quad (5.4)$$

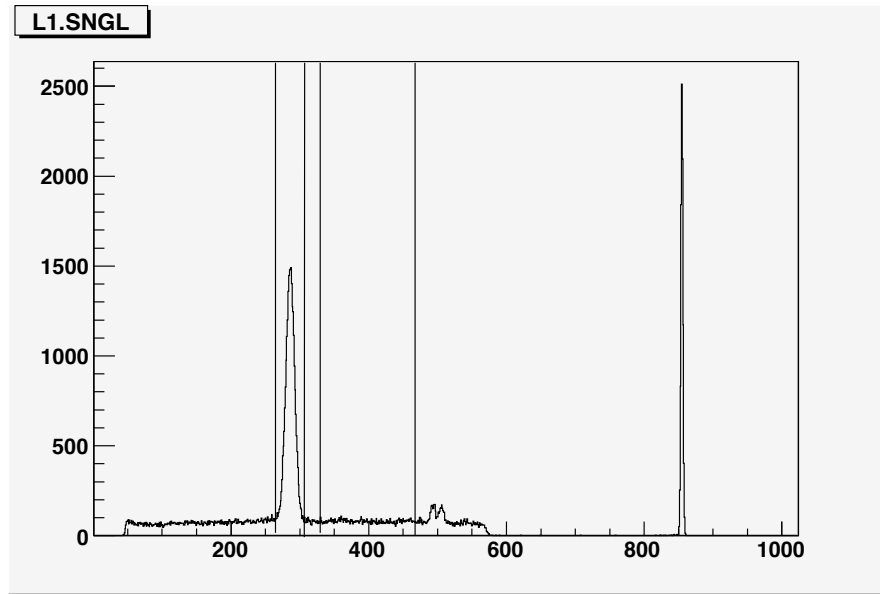


Figure 5.6: Polarimeter spectrum at 5.54 MeV showing the flat background from scattering on the polarimeter cell. This background was present occasionally, and the spectrum shown has the largest ratio of background to peak height. The background around the peak was estimated using the higher-energy gate as described in the text.

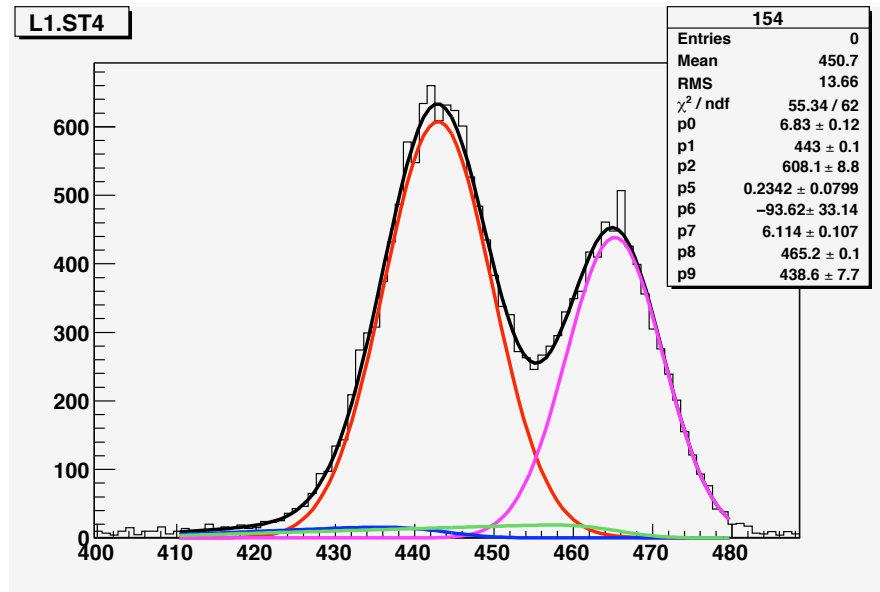


Figure 5.7:  $^3\text{He}(p,p)^3\text{He}$  spectrum taken at 2.28 Mev and  $40^\circ$ . The  $^4\text{He}$  peak is at higher energy than the  $^3\text{He}$  peak. The fit is described in the text.

where  $A$ ,  $x_0$ , and  $\sigma$  were the usual amplitude, mean, and width, respectively. Here  $\Delta x(x)$  represented the amount of energy lost by the particles, and was parameterized crudely as a linear function

$$\Delta(x) = c(mx + b). \quad (5.5)$$

This dependence of energy loss on the energy meant that not only was the mean of the peak affected by energy loss, but the shape also, since the higher energy part of the peak lost less energy than the lower energy part. The parameters  $m$  and  $b$  were fit to TRIM data and found to be  $m = -3.44 \times 10^{-6} \text{ m}^{-1}$  and  $b = 25.5 \times 10^{-6} \text{ keV/m}$  in the relevant energy range. The overall length scale  $c$  (in meters) was adjusted for energy loss during actual fitting. The integral over all  $x$  of the peak function is [Spi92]

$$I = \frac{\sqrt{2\pi} A \sigma}{1 - 3.44c}, \quad (5.6)$$

with uncertainty

$$\sigma_I = I \sqrt{\left(\frac{\sigma_A}{A}\right)^2 + \left(\frac{\sigma_\sigma}{\sigma}\right)^2 + \left(\frac{-3.44\sigma_c}{1 - 3.44c}\right)^2}. \quad (5.7)$$

In practice, including the effect of energy loss was not always necessary to obtain a good fit, so that in those cases the fitted value of  $c$  was consistent with 0.

A slit scattering tail was added to each peak. The tail was assumed to be linear, except that the probability of a particle's being scattered out of the peak and into a given tail channel was assumed to be proportional to the fraction of the peak area at higher channels,

$$\begin{aligned} \text{tail} &= P(x) * (m_t x + b_t) = \left( \frac{\int_x^{+\infty} f(x) dx}{\int_{-\infty}^{+\infty} f(x) dx} \right) * (m_t x + b_t) \\ &= \left( \text{erf}\left(\frac{x_0 - x - \Delta x(x)}{\sqrt{2}\sigma}\right) + 1 \right) * (m_t x + b_t), \end{aligned} \quad (5.8)$$

where  $\text{erf}()$  is the error function. Effectively, this meant that the tail was a linear function that went smoothly to zero under the peak.

The function actually used to fit was a combination of 2 Gaussians with energy loss and with tails. For consistency,  $\Delta x(x)$  was assumed to be the same for both peaks. Since the tail of the  $^4\text{He}$  peak wasn't visible by itself, it was assumed to have the same  $m_t$  and  $b_t$  as the  $^3\text{He}$  tail, but an amplitude equal to the ratio of the peak amplitudes multiplied by the  $^3\text{He}$  tail amplitude. The full function was therefore the sum of the following four functions:

$$\text{peak}_1 = A_1 e^{-\frac{1}{2}((x + \Delta x(x) - x_{01})/\sigma_1)^2}, \quad (5.9)$$

$$\text{tail}_1 = \left( \text{erf} \left( \frac{x_{01} - x - \Delta x(x)}{\sqrt{2}\sigma_1} \right) + 1 \right) * (m_t x + b_t), \quad (5.10)$$

$$\text{peak}_2 = A_2 e^{-\frac{1}{2}((x + \Delta x(x) - x_{02})/\sigma_2)^2}, \quad (5.11)$$

$$\text{tail}_2 = \frac{A_2}{A_2} \left( \text{erf} \left( \frac{x_{02} - x - \Delta x(x)}{\sqrt{2}\sigma_2} \right) + 1 \right) * (m_t x + b_t). \quad (5.12)$$

### 5.2.3 Dead Time

The number of counts in a spectral peak is related to the number of particles actually scattered into the detector, but is not identical with it, since the data-acquisition system is sometimes “busy” when the detector produces a signal. This “dead-time”, produced primarily by the length of time required by the ADC to digitize the signal, means that there are fewer counts in the spectrum than there were protons scattered into the detector. To obtain the latter, the former must be corrected by the fraction of time the data-acquisition system (DAQ) was busy. We obtained this dead-time correction (dtc) by adding a pulser signal to the data at the pre-amp, while from the same module sending a scaler to the DAQ. The dtc was taken to be the ratio of the number of pulser scaler counts  $n_{pul}$ , which did not go through the ADC to the number of the pulser signals  $N_{pul}$ , which did,

$$\text{dtc} = \frac{n_{pul}}{N_{pul}}. \quad (5.13)$$

The uncertainty of the dead-time correction was calculated by assuming that the number of missing pulser signals,  $n_{pul} - N_{pul}$ , was randomly distributed,

$$\sigma_{\text{dtc}} = \text{dtc} \frac{\sigma_{N_{pul}}}{N_{pul}} = \text{dtc} \frac{\sqrt{n_{pul} - N_{pul}}}{N_{pul}}. \quad (5.14)$$

We then took the number of particles scattered into the detector to be the number of peak counts times this correction factor, and propagate the uncertainty accordingly. Typical dead-time corrections were less than 1%, and were less than 10% in all cases. Two of the detector pairs share a single ADC, so that separate dead-time corrections were not possible for both detectors in those pairs. Since the ADC itself was assumed to be the primary source of dead-time, the correction from one detector was applied to both.



### 5.3 Asymmetries

Once the relative number of particles scattered in each spin state has been found, the asymmetries for each run can be calculated according to equations 4.19-4.22. Each asymmetry is of the form

$$Asym = \frac{x - 1}{x + 1}, \quad (5.15)$$

where

$$x = \sqrt{\frac{S_1 S_2}{S_3 S_4}}. \quad (5.16)$$

The uncertainty in the asymmetry is therefore

$$\sigma_{Asym} = \frac{x}{(x + 1)^2} \sqrt{\sum_{i=1}^4 \left( \frac{\sigma_{S_i}}{S_i} \right)^2}. \quad (5.17)$$

Each of the factors  $S_i$  is the sum of the BCI-normalized yields in two spin-states, e.g.

$$S_i = \frac{N_1}{b_1} + \frac{N_2}{b_2}, \quad (5.18)$$

with uncertainty

$$\sigma_S = \sqrt{\left( \frac{\sigma_{N_1}}{b_1} \right)^2 + \left( \frac{\sigma_{N_2}}{b_2} \right)^2}. \quad (5.19)$$

The detector yields  $N$  and their uncertainties  $\sigma_n$  were discussed above. Since the target cell pressure was assumed constant over the length of a run, the yields were only explicitly normalized to target pressure in the case where different target spin states were measured with different shots of polarized gas.

### 5.4 Polarized Beam Preparation

The polarized beam was produced by the TUNL Atomic Beam Polarized Ion Source [Cle95]. The ABPIS produces a polarized beam whose quantization axis is parallel to the beam direction. A Wein filter, which makes crossed electric and magnetic fields, produces other spin orientations as desired. Essentially, the filter's dipole magnetic field precesses beam spins to the new orientation as they pass through it, and the amount of precession is determined by the strength of the field. The dipole electric field corrects for the  $\vec{v} \times \vec{B}$  beam steering introduced by the magnetic field.

A calibration of the Wein filter's precession was performed just prior to the beginning of the main data-taking, in which the magnetic field setting corresponding to the maximum y-component of the beam spin was determined. The calibration was performed by measuring the  $p+^4\text{He}$  scattering asymmetry for various Wein filter settings. The asymmetry was measured at a lab bombarding energy of  $5.51 \pm 0.04$  MeV and a lab scattering angle of  $120^\circ$ , where the analyzing power is known to be large [Sch71].

Figure 5.8 shows the  $p+^4\text{He}$  scattering asymmetry, proportional to the beam polarization, vs. Wein filter magnetic field strength. The error bar includes a 2% uncertainty as an estimate of the stability of the overall polarization at the source, which was added in quadrature with the statistical uncertainties. A sine function,

$$f(x) = a \sin(bx + c), \quad (5.20)$$

fit to the data was used to determine the magnetic field value corresponding to maximum polarization, which occurs when the sine argument equals  $90^\circ$ :

$$x_{max} = \frac{1}{b} \left( \frac{\pi}{2} - c \right). \quad (5.21)$$

The uncertainty, according to Equation 5.1, is

$$\sigma_{x_{max}} = \frac{1}{b} \sqrt{\left( \frac{\pi}{2} * \frac{\sigma_b}{b} \right)^2 + \sigma_c^2}. \quad (5.22)$$

The result was  $405.8 \pm 1.7$  G.

## 5.5 Measurement of Beam Polarization

Beam polarization measurements were made with  $p+^4\text{He}$  elastic scattering in either the target cell or in an Al polarimeter chamber installed upstream of the target chamber. Detectors in the latter could be mounted in the horizontal or vertical scattering planes, so that either polarization component could be measured. The detectors were mounted at  $110^\circ$  in holders which held brass collimators with circular apertures in a snout. Havar foils, either 6.35 or 2.54  $\mu\text{m}$  thick, were epoxied with Armstrong A-12 epoxy to a 2.54 cm diameter target cell to contain the  $^4\text{He}$  gas. The cell could be moved several centimeters inside the chamber from the outside, allowing it to be inserted periodically into the beam for polarization measurements and removed to allow beam to pass unobstructed to the scattering chamber. Proton bombarding energies in the polarimeter were somewhat different than in the target cell, and are tabulated in Table 5.3.

The  $p+^4\text{He}$  asymmetries were divided by  $A_y$  to obtain the beam polarization. Phase-shifts obtained from smooth curves fit to the published values of [Sch71] were used in a

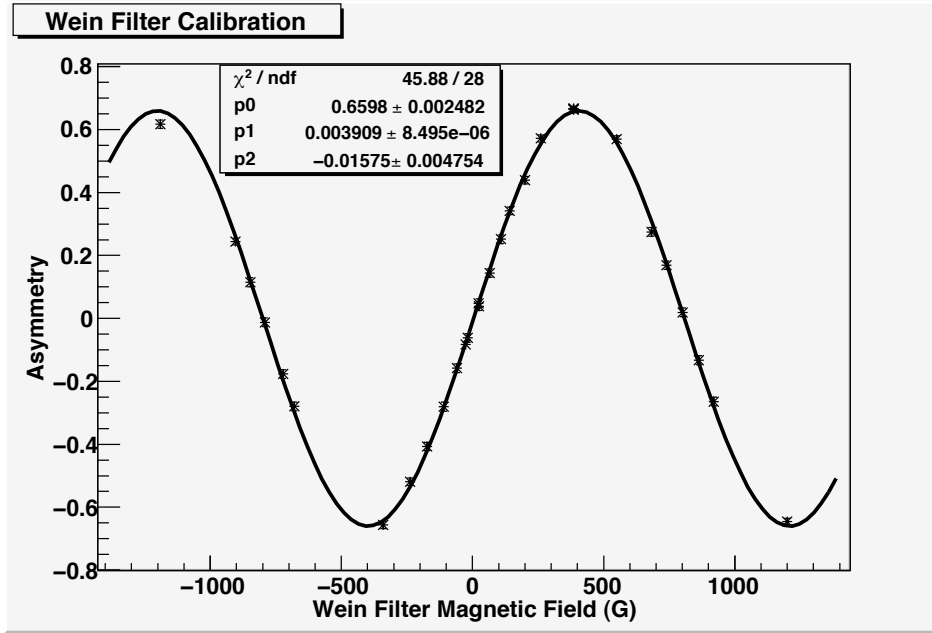


Figure 5.8: Wein Filter Calibration

Table 5.3: Polarimeter cell bombarding energies

Incoming Beam Energy (MeV)	Havar Entrance Foil Thickness ( $\mu\text{m}$ )	Energy After Entrance Foil (MeV)	Energy at Cell Center (MeV)
5.77 $\pm$ 0.04	6.35	5.55 $\pm$ 0.04	5.52 $\pm$ 0.04
5.66 $\pm$ 0.04	2.54	5.57 $\pm$ 0.04	5.54 $\pm$ 0.04
4.15 $\pm$ 0.03	2.54	4.04 $\pm$ 0.03	4.00 $\pm$ 0.03
3.54 $\pm$ 0.03	6.35	3.23 $\pm$ 0.03	3.19 $\pm$ 0.03
3.31 $\pm$ 0.03	2.54	3.18 $\pm$ 0.02	3.13 $\pm$ 0.02
2.75 $\pm$ 0.02	6.35	2.39 $\pm$ 0.03	2.33 $\pm$ 0.03
2.48 $\pm$ 0.02	2.54	2.32 $\pm$ 0.02	2.27 $\pm$ 0.02

Table 5.4: Polarimeter cell analyzing powers

Bombarding Energy (MeV)	$A_y$
$5.54 \pm 0.04$	$0.956 \pm 0.016$
$5.52 \pm 0.04$	$0.956 \pm 0.016$
$3.19 \pm 0.03$	$0.863 \pm 0.018$
$2.33 \pm 0.03$	$0.650 \pm 0.021$

spin $\frac{1}{2}$ -on-spin0 phase-shift code [Pri03] to obtain  $A_y$  at the energies listed in Table 5.4.

For much of the spin-correlation data taken in 2007, however, the beam polarization was unstable, so that periodic monitoring would not necessarily determine the average polarization. It was therefore decided to determine the polarization along the y-axis by normalizing our relative  $A_{y0}$  measurements to those of [Fis03] or [All93a]. Each point in a relative  $A_{y0}$  angle set was divided by a value linearly interpolated from [Fis03] or [All93a] at the same energy, and the polarization was taken to be the average of these ratios. An uncertainty of 0.02 was assigned to the polarization and added in quadrature with our statistical uncertainties. No published data was available at 2.7 MeV, so smooth curves were fit through the existing distributions at each angle vs. energy and evaluated at 2.7 MeV. The normalization then proceeded as above.

The procedure was extended to  $A_{xx}$  for some distributions by “tipping” the spin 20° out of the plane with the Wein filter during data taking and applying the above analysis to the y-component. The x-component was obtained by multiplying the y-component by the ratio of the two components, which was calculated according to Equation A.1. Other  $A_{xx}$  data relied on polarimeter measurements.

## 5.6 Measurement of Target Polarization

As discussed in Chapter 3, pulsed NMR was used to give a relative measure of the target polarization. The NMR measurements for each “shot” of polarized gas were normalized by the partial  $^3\text{He}$  pressure in the target cell. The uncertainty for those N measurements  $y(t)$  was taken to be the average deviation,

$$\sigma_{NMR} = \sqrt{\frac{(y_i - f(t_i))^2}{N - 2}} \quad (5.23)$$

of the points from an exponential fit,

$$f(t) = Ae^{-\frac{t}{\tau}}, \quad (5.24)$$

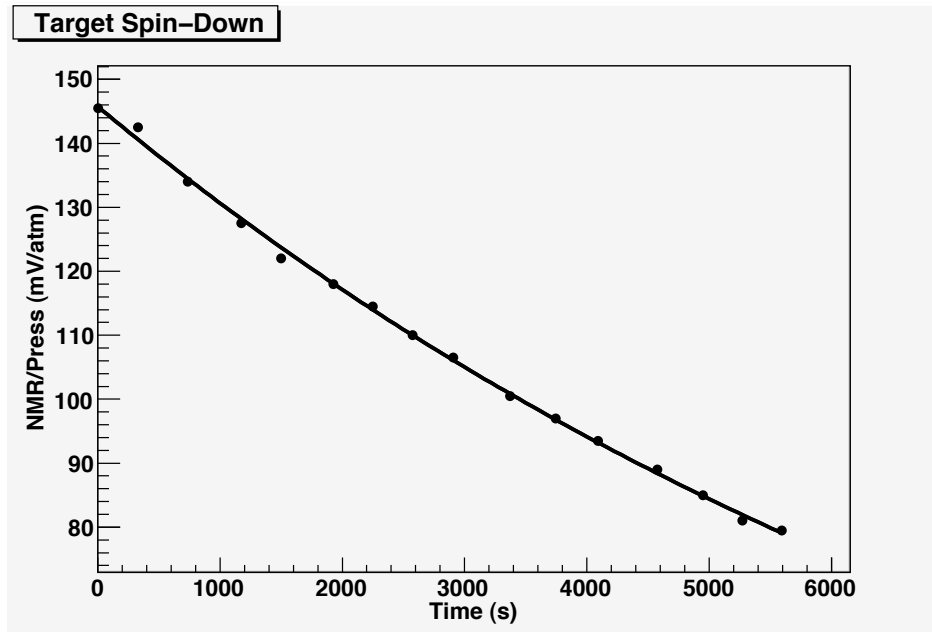


Figure 5.9: Relative target polarization vs. time for one “shot” of polarized gas

An example fit is shown in Figure 5.9. Those occasional runs whose NMR measurements failed were assigned values from the fit. To obtain target polarizations, the relative NMR measurements were divided by the target cell calibration constant, discussed below, and the uncertainty was propagated accordingly.

The calibration factor relating the relative pressure-normalized NMR reading to the target polarization was determined each time a target cell was glued with new foils and remounted in a target holder. Since the entrance and exit foils failed frequently, this procedure was performed a number of times<sup>2</sup>. As described in [Kat05], the calibration constants were determined by measuring the asymmetry of alpha particles, provided by the TUNL helium source, scattered from the polarized target at 45°, where we confirmed that the analyzing power is near an absolute minimum value of -1, as described below. This asymmetry, therefore, was a direct measure of the target polarization. The bombarding energies are listed in Table 5.5. During calibrations, relative NMR measurements of the target polarization were made together with measurements of the alpha asymmetry. The polarization of the target decayed during calibrations, so that each calibration spanned a range of target polarization values.

The target asymmetries were plotted as a function of pressure-normalized target NMR, and the calibration factor was extracted as the slope from a linear fit to the plot, as shown in Figure 5.10. Typical statistical uncertainties for calibration measurements were about 2%,

<sup>2</sup>28 calibrations were actually analyzed, though some other unsuccessful attempts were made. These usually ended when the cell began to leak. The necessity of using an additional beam source for these calibrations, and one which often required maintenance, was one of the more painful aspects of the experiment.

Table 5.5: Bombarding energies for target cell calibrations

Incoming Beam Energy (MeV)	Kapton Entrance Foil Thickness ( $\mu\text{m}$ )	Energy After Entrance Foil (MeV)	Energy at Cell Center (MeV)
$16.82 \pm 0.12$	25.4	$15.60 \pm 0.14$	$15.44 \pm 0.14$
$16.82 \pm 0.12$	17.8	$15.97 \pm 0.13$	$15.82 \pm 0.13$
$16.15 \pm 0.11$	7.62	$15.78 \pm 0.11$	$15.62 \pm 0.15$

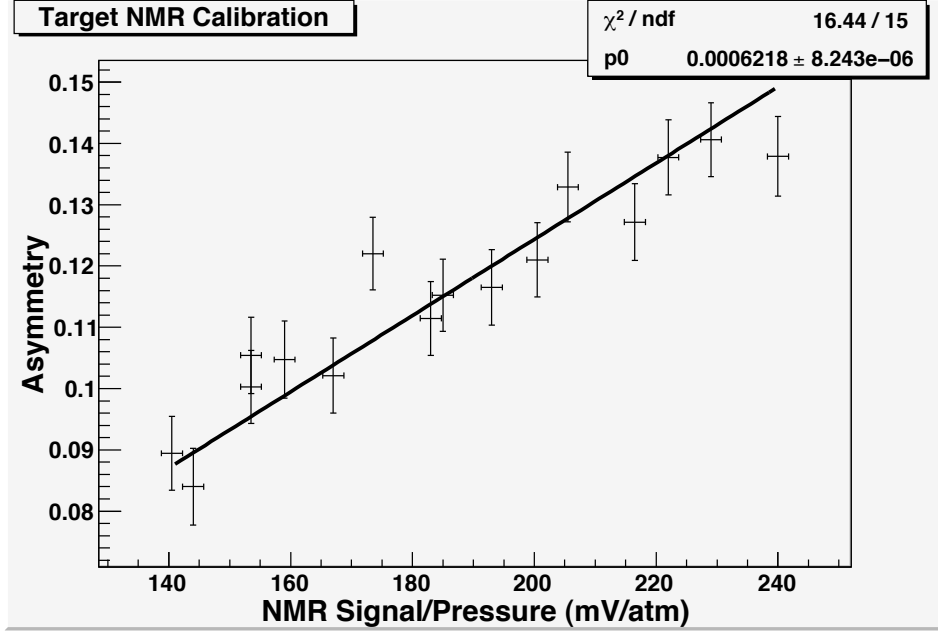


Figure 5.10: Determination of target nmr calibration constant.

and the variation of different calibrations was about 10%.

## 5.7 Location of Calibration Point

Our determination of the calibration point in  $\alpha + {}^3\text{He}$  elastic scattering followed the prediction of [Pla71] of an  $A_y = -1$  point near 15.33 MeV  ${}^3\text{He}$  lab energy and  $47^\circ$   ${}^3\text{He}$  lab scattering angle. The authors cautioned that their prediction for the location of the minimum, based on the phase-shifts of [Har70], was only approximate. Since absolute measurements of the analyzing power were impossible without a calibrated target cell, *relative* measurements of  $\alpha + {}^3\text{He}$   $A_y$  as a function of angle and energy near that location were used to determine a local minimum, and a value of -1 was assigned to that point. The energies used are in Table 5.6.

Figure 5.11 shows our relative measurements of  $\alpha + {}^3\text{He}$   $A_y$  at 15.44 MeV. The observ-

Table 5.6: Bombarding energies for  $\alpha+{}^3\text{He}$   $A_y$  minimum

Incoming Beam Energy (MeV)	Kapton Entrance Foil Thickness ( $\mu\text{m}$ )	Energy After Entrance Foil (MeV)	Energy at Cell Center (MeV)
$15.51\pm 0.11$	25.4	$14.21\pm 0.14$	$14.04\pm 0.14$
$16.17\pm 0.11$	25.4	$14.92\pm 0.14$	$14.74\pm 0.14$
$16.82\pm 0.12$	25.4	$15.60\pm 0.14$	$15.44\pm 0.14$
$17.40\pm 0.12$	25.4	$16.22\pm 0.14$	$16.06\pm 0.14$
$18.22\pm 0.13$	25.4	$17.08\pm 0.15$	$16.92\pm 0.15$
$18.64\pm 0.13$	25.4	$17.52\pm 0.15$	$17.37\pm 0.15$
$19.40\pm 0.14$	25.4	$18.31\pm 0.15$	$18.17\pm 0.15$

able was calculated according to Equation 4.19, except that the relative NMR measurements of target polarization were used without applying the target cell calibration constant. Repeated angles were averaged together, weighted by their error bars. The weighted mean of  $N$  measurements  $y_i$  with uncertainties  $\sigma_i$  is [Leo94]

$$\mu = \sum_{i=0}^N \frac{y_i}{\sigma_i^2} \bigg/ \sum_{i=0}^N \frac{1}{\sigma_i^2}, \quad (5.25)$$

with uncertainty

$$\sigma_\mu = \sqrt{\left( \sum_{i=0}^N \frac{1}{\sigma_i^2} \right)^{-1}}. \quad (5.26)$$

A fourth-order polynomial was fit to the data and the minimum angle determined to be  $46.64 \pm 0.22^\circ$ . Measurements of  $A_y$  vs energy are shown in Figure 5.12. The present measurements agree with the prediction of [Har70] of a very shallow minimum, but did not extend to low enough energy to constrain a fit.

Our calibrations were performed at  $45^\circ$  and between 15.44 and 15.82 MeV. We assign a value of  $A_y$  for the calibrations relative to the minimum, and assume the value at the minimum is -1. This was straightforward with respect to angle, where we use values from the fit, obtaining

$$\frac{f(45)}{f(46.64)} = 0.993 \pm 0.008. \quad (5.27)$$

With respect to energy, however, there was no fit, but the value during any of the calibrations must be within 3% (the precision of the data in that region) of the minimum. The value assigned to  $A_y$  for calibrations was therefore  $-0.99 \pm 0.01$ .

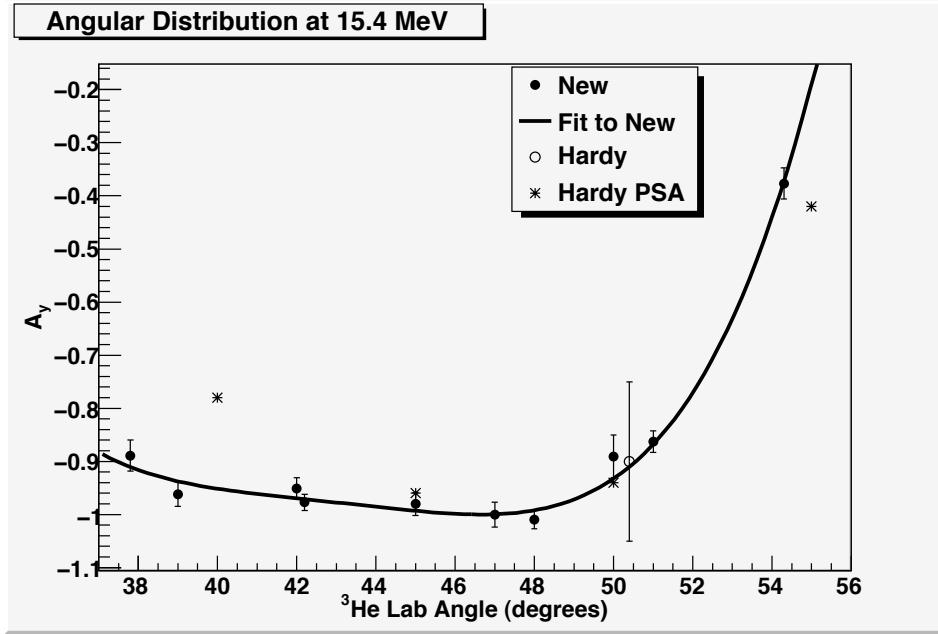


Figure 5.11:  $^4\text{He} + ^3\text{He}$   $A_y$  measurements with respect to angle. The present relative data are shown normalized so that minimum of the fitted curve, described in the text, is equal to -1. A data point from [Har70] is also shown, as well as results from their phase-shift analysis

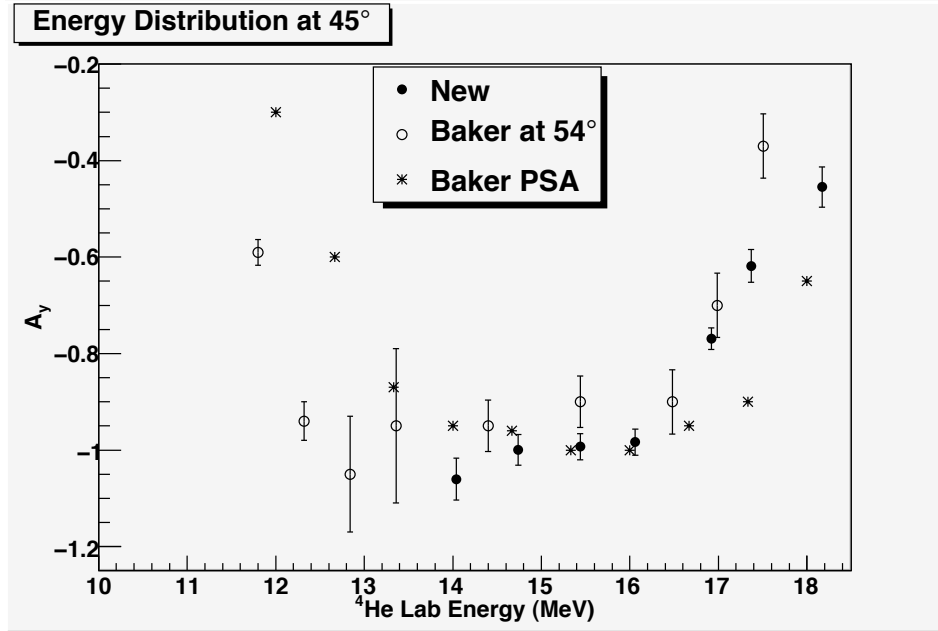


Figure 5.12:  $^4\text{He} + ^3\text{He}$   $A_y$  measurements with respect to energy. The present relative data are shown normalized so that the 15.4 MeV point is equal to -1. Results from the phase-shift analysis of [Har70] are shown along with data from that work at 54°.



## 5.8 Spin-Correlation Coefficients

Spin-correlation coefficients were measured simultaneously by four pairs of movable detectors, with the target and spin-correlation asymmetries for each run divided by the corresponding target polarization. Asymmetries from repeated runs with the detectors in the same position were averaged together according to Equation 5.25 into four-point angle-sets. This procedure was modified for those data taken without flipping the target spin during each run. An average target polarization was calculated for each polarized gas shot, and the total number of counts for each spin-state for the shot was divided by the  $^3\text{He}$  partial pressure. Asymmetries were then calculated using one shot with each spin orientation and the average target polarization of the two shots.

Angle sets at the same energy were combined into angular distributions by averaging together asymmetries at common angles. Angular distributions for  $A_{y0}$ ,  $A_{yy}$ , and  $A_{xx}$  were divided by the beam polarization as described above. Finally, angular distributions of the same observable at the same energy from different experimental runs were averaged together. The results are presented in the next chapter.

## 5.9 Steering Effect

An unexpected systematic error was discovered during data-taking. Figure 5.13 shows observables extracted from data taken while the target was unpolarized, when the asymmetries corresponding to the target analyzing power and spin-correlation coefficients should be zero. While this was true for  $A_{0y}$  calculated with the sine-theta coil's magnetic field turned off, non-zero asymmetries were obtained with the field on. The asymmetries for  $A_{yy}$ , on the other hand, were consistent with zero even with the field on.

The target magnetic field is believed to cause this effect by steering the incoming and scattered protons through the Lorentz force, as sketched in Figure 5.14. This steering can produce scattering asymmetries in at least two ways. First, it changes the solid angle subtended by the detectors about the scattering center by changing the location of that center. Thus, for a given orientation of the magnetic field, one detector of a left/right pair will be closer to the scattering and therefore detect more particles than it would without magnetic steering, while the other will be further away and see fewer. When the field orientation is reversed, the particles are steered in the opposite direction, and relationship between detector yields reverses. Thus, the steering introduces a systematic effect into scattering asymmetries which is *not* cancelled by reversing the target spin as other systematic effects are [Ohl72].

The magnetic steering also affects the measurement of scattering asymmetries by changing the effective scattering angle of the detectors, as illustrated in Figure 5.15. With the magnetic

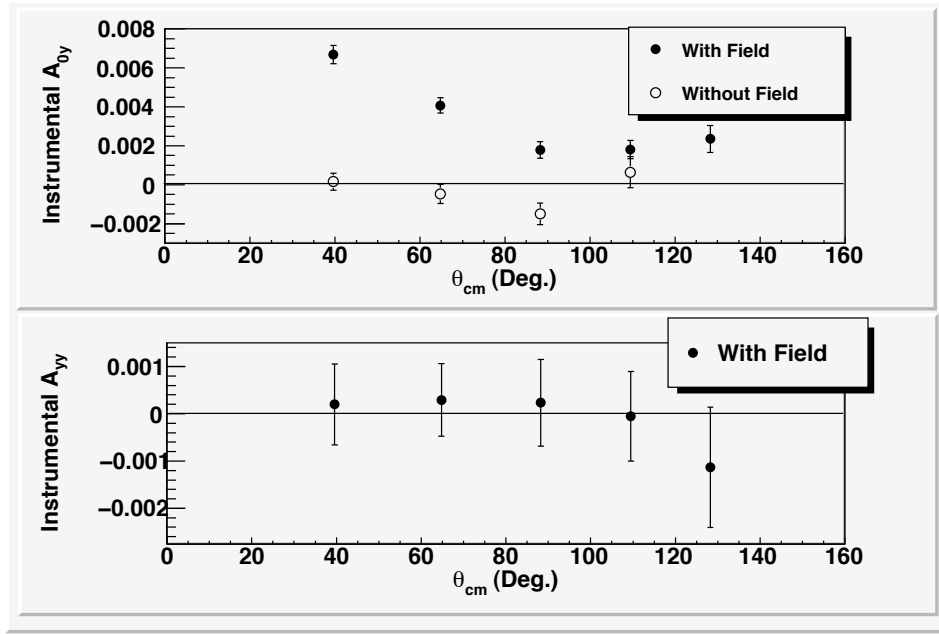


Figure 5.13: Instrumental effect. The upper panel shows asymmetries taken at 2.25 MeV for  $A_{0y}$  calculated according to Equation 4.19, except that the target is unpolarized. Asymmetries taken with the sine-theta coil magnetic field both on and off are shown. The lower panel shows asymmetries for  $A_{yy}$  with the field on. Note the difference in vertical scales for the two panels.

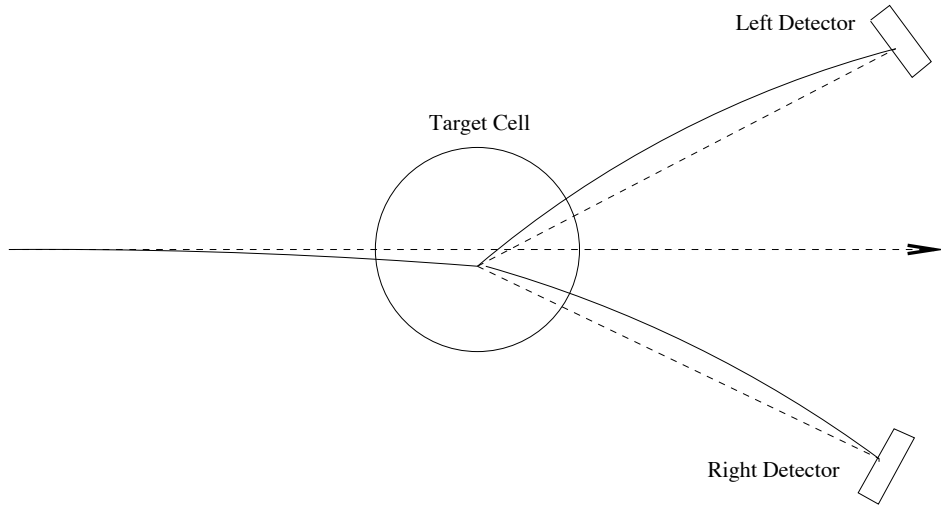


Figure 5.14: Steering of the incoming proton beam and scattered particles by the sine-theta coil magnetic field. The target cell and detectors are shown from above. The beam is incident from the left on the gas cell along the dotted line, but deflected as shown by the magnetic field, which is oriented out of the page. Similarly, the scattered particles travel along curved paths to the detectors. The figure is not to scale, and the size of the effect is exaggerated for clarity.

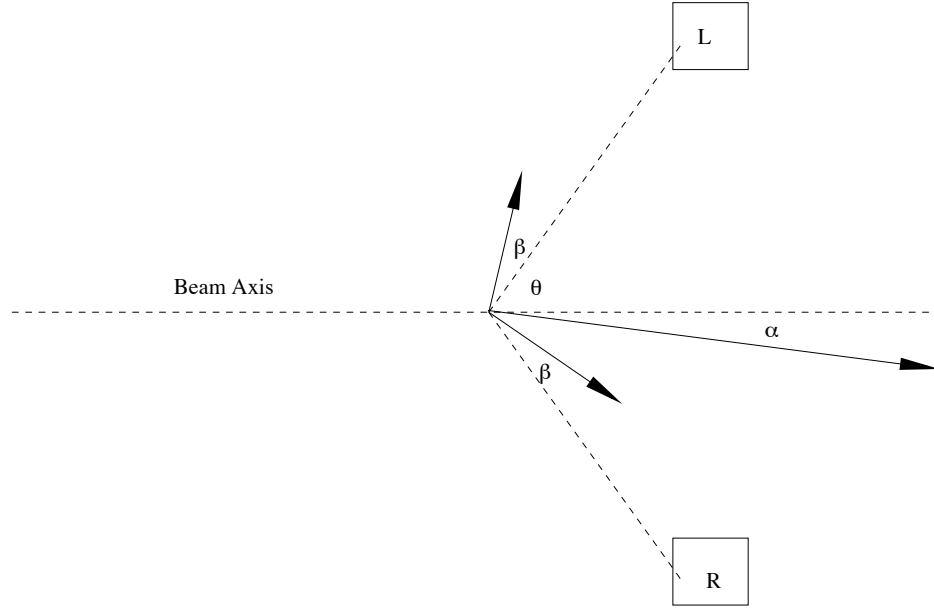


Figure 5.15: Deflection of the incoming beam and scattered particles through angles  $\alpha$  and  $\beta$ , respectively, by the sine-theta coil magnetic field.

field oriented “up”, the scattering angle of particles reaching the left detector is:

$$\theta'_L = \theta + \alpha + \beta, \quad (5.28)$$

where  $\theta$  is the detector angle,  $\alpha$  is the deflection of the incoming beam, and  $\beta$  is the deflection of the scattered particles. Similarly, the scattering angle for particles reaching the right detector is:

$$\theta'_R = \theta - \alpha - \beta. \quad (5.29)$$

This change in scattering angle produces an instrumental asymmetry through the angular dependence of the differential cross-section, a distribution of which is shown in Figure 5.16. Since the left and right detectors are effectively at different angles, they will have different yields. Once again, the situation reverses with the target magnetic field, so that this effect is not canceled in a cross-ratio calculation of the observable.

The result of a simple calculation of these two effects at 2.25 MeV is shown in Figure 5.17, along with the measured instrumental asymmetry. Though the largest deflection angle calculated was  $0.1^\circ$ , the resulting asymmetries are large enough to interfere with polarized target measurements. For example, the measurement of an observable equal to 0.1 with 20% target polarization would yield an asymmetry of 0.02. The instrumental effect was measured to be largest at the lowest beam energy of 2.25 MeV, where the particles would be most deflected by the magnetic field. The calculation neglects the finite size of the beam and

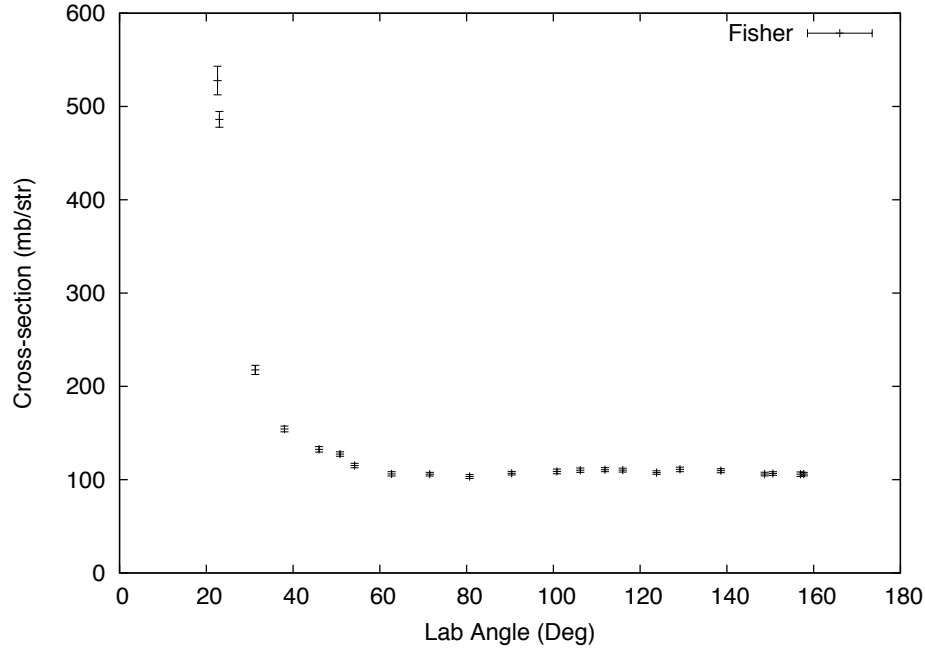


Figure 5.16: Angular distribution for  $A_{y0}$  [Fis06] for  $p+{}^3\text{He}$  elastic scattering at 2.25 MeV. The dependence is very strong at forward angles.

target, and simply determines the energy loss, modeled in TRIM, and magnetic steering of incoming and scattered protons in small steps as they proceed through the magnetic field. The calculation reproduces the general size and forward-angle trend of the effect, but not in sufficient detail to be used to correct the data. An initial attempt to model the effect in GEANT4 was abandoned because of the length of time that would have been required to obtain sufficiently accurate results.

Instead, measurements of the effect like those in Figure 5.17 are subtracted from polarized target asymmetries. The effect was measured both directly, on the target with unpolarized gas, and indirectly, from extrapolating polarized target asymmetries to zero polarization. This indirect approach is illustrated in Figure 5.18. Since the target polarization degrades during measurements, data are collected at a range of polarization values. The instrumental asymmetry is extracted as the y-intercept of a linear fit to asymmetry vs. polarization. Direct and indirect measurements were averaged together to obtain the measurements used to correct the polarized data. Since no non-zero effect was observed for spin-correlation data, the correction was only applied to  $A_{0y}$ .

An example of the correction is shown in Figure 5.19 for  $A_{0y}$  at 2.25 MeV. The uncorrected points are extracted from the raw data according to Equation 4.19. The corrected points are obtained by subtracting from the uncorrected points the measured instrumental asymmetries shown in Figure 5.17, divided by the average target polarization of the uncorrected points.

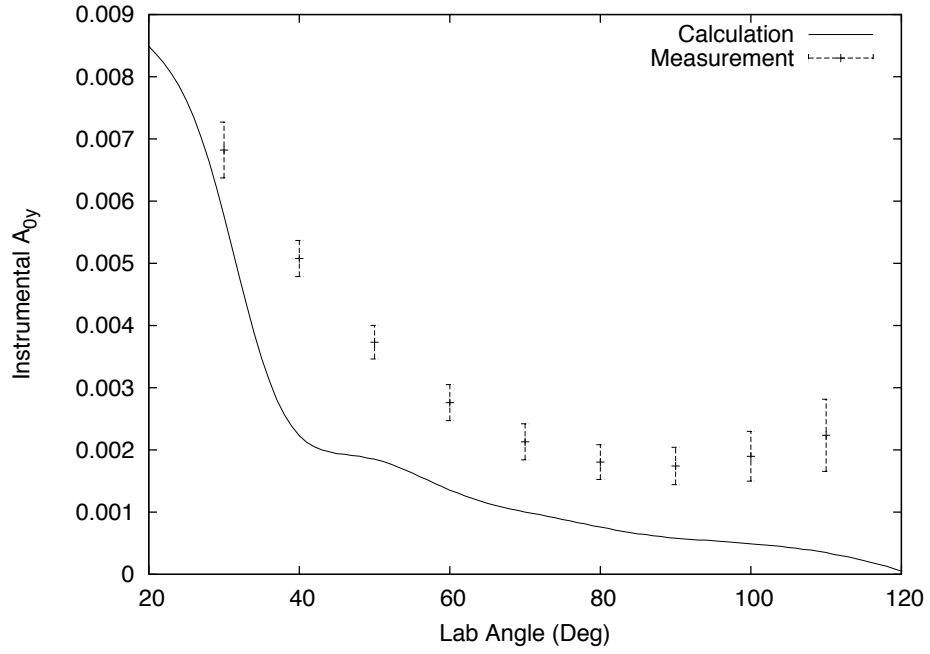


Figure 5.17: The calculated instrumental effect for  $A_{y0}$  at 2.25 MeV as discussed in the text, shown with measured values.

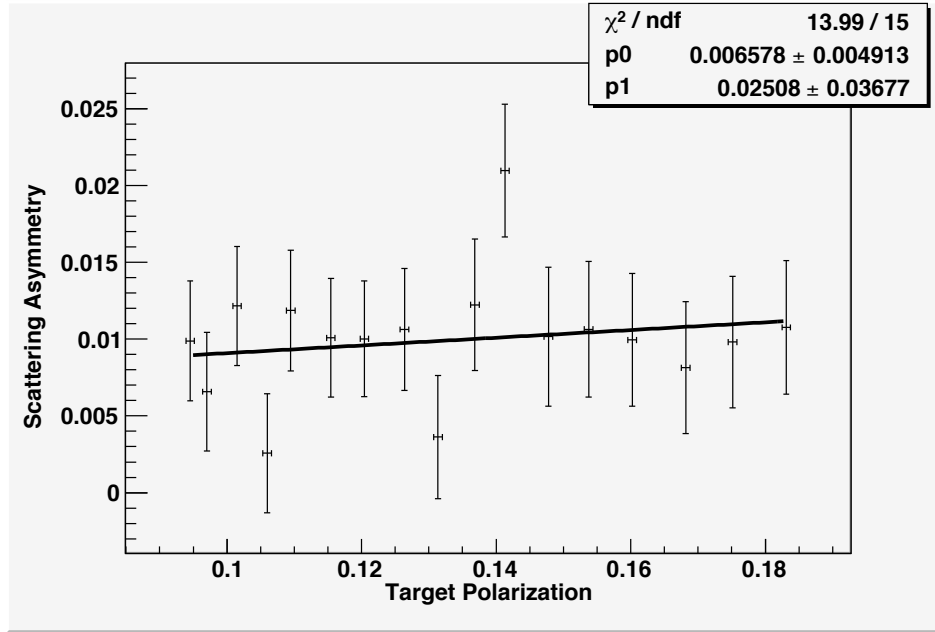


Figure 5.18: Target asymmetries measured during one “shot” of polarized gas, plotted as a function of polarization. The y-intercept,  $p_0$ , of the fitted line, which would be consistent with zero in the absence of an instrumental effect, is an indirect measurement of that effect.

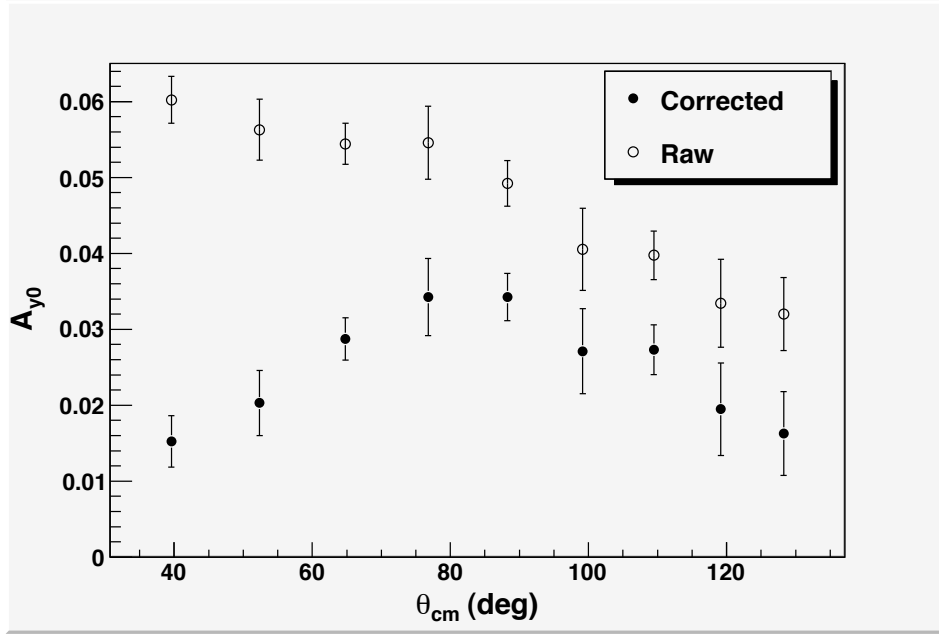


Figure 5.19: Correction for systematic asymmetry for  $A_{y0}$  at 2.25 MeV. The final, corrected distribution is shown along with the uncorrected one.

Thus, these corrections obtained are very large. The uncertainty of the uncorrected points and the instrumental asymmetries are propagated through this calculation according to Equation 5.1.

## 6 Phase-Shift Analysis

---

A phase-shift analysis of the global  $p+{}^3\text{He}$  elastic scattering database below  $E_p = 12\text{MeV}$  was performed. This analysis was a repetition of the [Geo03] analysis, the database for which is listed in Table 1.1, with the addition of the  $\frac{d\sigma}{d\Omega}$  and  $A_{y0}$  measurements of [Fis06] and the new  $A_{0y}$ ,  $A_{yy}$ , and  $A_{xx}$  measurements made for this work. These additional data all fell between 1.0 and 5.54 MeV. The search routine used in [Geo03] was provided by Elizabeth George [Geo06].

### 6.1 Calculation of Observables

In a phase-shift analysis, the scattering amplitude is expanded in powers of orbital angular momentum, and the coefficients of that expansion are determined by fitting observables calculated from the scattering amplitude to data. This is useful because, especially at low energies, only a few angular-momentum states are usually necessary, so that a small number of experimental parameters can be used to describe all the scattering observables. For spin-polarized scattering, the scattering matrix fills the role of the usual scattering amplitude, and its elements are expanded in partial waves for the analysis. As we will see, the fact that the nuclear Hamiltonian preserves only the total angular momentum  $j$  and parity  $\pi$ , and not the initial spins or relative angular momentum, complicates the expansion.

Equation 4.14 provides the connection between the scattering matrix elements and the scattering observables. A parameterization of the scattering matrix by LaFrance and Winternitz [Fra80] in terms of the Pauli spin matrices is used. The parameterization is

$$M(\vec{k}', \vec{k}) = \frac{1}{2} \left[ (a+b) + (a-b)(\vec{\sigma}_1 \cdot \hat{n})(\vec{\sigma}_2 \cdot \hat{n}) + (c+d)(\vec{\sigma}_1 \cdot \hat{m})(\vec{\sigma}_2 \cdot \hat{m}) \right. \\ \left. + (c-d)(\vec{\sigma}_1 \cdot \hat{l})(\vec{\sigma}_2 \cdot \hat{l}) + e(\vec{\sigma}_1 + \vec{\sigma}_2) \cdot \hat{n} + f(\vec{\sigma}_1 - \vec{\sigma}_2) \cdot \hat{n} \right], \quad (6.1)$$

where the complex amplitudes  $a$  through  $f$  are functions of energy and angle. The unit vectors  $\hat{l}$ ,  $\hat{m}$ , and  $\hat{n}$  are defined according to

$$\hat{l} = \frac{\vec{k}' + \vec{k}}{|\vec{k}' + \vec{k}|}, \quad \hat{m} = \frac{\vec{k}' - \vec{k}}{|\vec{k}' - \vec{k}|}, \quad \text{and} \quad \hat{n} = \frac{\vec{k}' \times \vec{k}}{|\vec{k}' \times \vec{k}|}. \quad (6.2)$$

The  $4 \times 4$  matrices  $\vec{\sigma}_1$  and  $\vec{\sigma}_2$  describe the spin of the proton and  $^3\text{He}$  nucleus, respectively. They are formed from the usual  $2 \times 2$  Pauli matrices  $\vec{\sigma}(2)$ :

$$\vec{\sigma}_1 = \vec{\sigma}_1(2) \otimes 1 \quad \text{and} \quad \vec{\sigma}_2 = 1 \otimes \vec{\sigma}_2(2). \quad (6.3)$$

The observables can be expressed in terms of the six complex amplitudes by combining Equations 4.14 and 6.1:

$$\frac{d\sigma_0}{d\Omega} = \frac{1}{2} (|a|^2 + |b|^2 + |c|^2 + |d|^2 + |e|^2 + |f|^2) \quad (6.4a)$$

$$\frac{d\sigma_0}{d\Omega} A_{y0} = \text{Re}(a * e + b * f) \quad (6.4b)$$

$$\frac{d\sigma_0}{d\Omega} A_{0y} = \text{Re}(a * e - b * f) \quad (6.4c)$$

$$\frac{d\sigma_0}{d\Omega} A_{yy} = \frac{1}{2} (|a|^2 - |b|^2 - |c|^2 + |d|^2 + |e|^2 - |f|^2) \quad (6.4d)$$

$$\frac{d\sigma_0}{d\Omega} A_{xz} = -\text{Re}(a * d) \sin \theta + \text{Im}(c * f) - \text{Im}(d * e) \cos \theta \quad (6.4e)$$

$$\frac{d\sigma_0}{d\Omega} A_{zx} = -\text{Re}(a * d) \sin \theta - \text{Im}(c * f) - \text{Im}(d * e) \cos \theta \quad (6.4f)$$

$$\frac{d\sigma_0}{d\Omega} A_{xx} = \text{Re}(a * d) \cos \theta + \text{Re}(b * c) - \text{Im}(d * e) \sin \theta \quad (6.4g)$$

$$\frac{d\sigma_0}{d\Omega} A_{zz} = -\text{Re}(a * d) \cos \theta + \text{Re}(b * c) + \text{Im}(d * e) \sin \theta \quad (6.4h)$$

The coefficients are expressed in terms of the scattering matrix elements by solving Equation 6.1:

$$a = \frac{1}{2} (M_{1010} + M_{1111} - M_{1-111}) \quad (6.5a)$$

$$b = \frac{1}{2} (M_{1010} + M_{1111} - M_{1-111}) \quad (6.5b)$$

$$c = \frac{1}{2} (-M_{0000} + M_{1111} + M_{1-111}) \quad (6.5c)$$

$$d = \frac{-1}{\sqrt{2} \sin \theta} (M_{1110} + M_{1011}) \quad (6.5d)$$

$$e = \frac{i}{\sqrt{2}} (M_{1110} - M_{1011}) \quad (6.5e)$$



$$f = -i\sqrt{2}(M_{1100}) \quad (6.5f)$$

In this way, the parameterization of Eq. 6.1 provides a convenient bridge between the experimental observables and scattering matrix elements via the scattering amplitudes.

In Equations 6.5, the scattering matrix elements are expressed in the basis of the coupled spin  $s$  of the two particles and its projection  $s_z$ . This may seem unnatural, since the beam and target particles have been prepared in definite states of their individual projections, but the fact that the total angular momentum is the conserved quantity in the scattering makes the coupled spin representation preferable.

## 6.2 Partial-Wave Expansion

In preparation for the partial-wave expansion, the Coulomb scattering amplitude  $C(\theta)$ , which preserves the entrance channel spins, is separated from the term containing nuclear physics information that mixes spins:

$$M_{ss_zs's'_z} = \frac{i\sqrt{\pi}}{k} \left[ iC(\theta) \delta_{ss'} \delta_{s_zs'_z} + B_{ss_zs's'_z} \right], \quad (6.6)$$

where  $s'$  is the coupled outgoing spin and  $s'_z$  is its projection. The c.m. wave number  $k$  is given by

$$k = \frac{\mu\nu}{\hbar}, \quad (6.7)$$

where  $\mu$  is the reduced mass and  $\nu$  is the relative velocity between the two particles. The Coulomb scattering amplitude can be calculated directly:

$$C(\theta) = \frac{\eta}{4\pi} \csc^2\left(\frac{\theta}{2}\right) e^{i\eta \ln \csc^2\left(\frac{\theta}{2}\right)}, \quad (6.8)$$

where  $\eta$  is the Coulomb penetration factor,

$$\eta = \frac{Z_1 Z_2 e^2}{\hbar\nu}. \quad (6.9)$$

The charges of the beam and target particles are  $Z_1 e$  and  $Z_2 e$ , respectively.

The matrix  $B$  is expanded in partial waves:

$$B_{ss_zs's'_z} = \sum_{l'l'j} \sqrt{2l+1} \langle sls_z 0 | js_z \rangle \langle s'l's'_z s_z - s'_z | js_z \rangle i^{|l-l'|} U_{l's',ls}^j Y_{l'}^{s_z-s'_z}(\theta, 0), \quad (6.10)$$

where the sum is carried out over not only the initial angular momentum  $l$ , as it would be for scattering for a spherically symmetric potential, but also over the outgoing values  $l'$  that

share the same  $j^\pi$ , as discussed in Appendix B. The terms  $\langle sls_z 0 | js_z \rangle$  and  $\langle s' l' s'_z s_z - s'_z | js_z \rangle$  are Clebsch-Gordan coefficients and the  $Y_{l' s'_z}^{s_z - s'_z}(\theta, 0)$  are the spherical harmonics. The matrix  $U$  contains the phase-shifts, and is given by:

$$U_{l' s', ls}^j = e^{i(\alpha_l + \alpha_{l'})} \left( \delta_{l, l'} \delta_{s, s'} - S_{l' s', ls}^j \right), \quad (6.11)$$

where the  $\alpha_l$  are the modified Coulomb phase-shifts,

$$\alpha_l = \sum_{s=1}^l \arctan \left( \frac{\eta}{s} \right), \quad (6.12)$$

and  $\alpha_0 = 0$ .

The S-matrix contains the nuclear phase-shifts, and is in that sense the heart of the expansion. It is a 4x4 matrix connecting incoming and outgoing orbital angular momenta that couple to a given value of total angular momentum, as listed in Appendix B. The nuclear interaction must preserve parity, however, so the S-matrix doesn't connect states for which  $|l - l'|$  is odd. This means that the S-matrix breaks down into two 2x2 submatrices, as discussed in [All92]. These submatrices are parameterized according to the convention of Blatt and Biedenharn [Bla52]:

$$S = \begin{pmatrix} \cos^2(\epsilon) e^{2i\delta_1} + \sin^2(\epsilon) e^{2i\delta_2} & \frac{1}{2} \sin 2\epsilon [e^{2i\delta_1} - e^{2i\delta_2}] \\ \frac{1}{2} \sin 2\epsilon [e^{2i\delta_1} - e^{2i\delta_2}] & \cos^2(\epsilon) e^{2i\delta_2} + \sin^2(\epsilon) e^{2i\delta_1} \end{pmatrix}, \quad (6.13)$$

where  $\delta_1$  and  $\delta_2$  are the “eigenphase-shifts”, which would resolve into the usual phase-shifts in absence of mixing, which is described by  $\epsilon$ . The freedom to choose which eigenphase-shift will be  $\delta_1$  leaves the sign of the mixing parameter undetermined. The eigenphase-shift  $\delta_1$  is therefore chosen to be the parameter with a smaller value of either  $l$  or  $s$ .

### 6.3 Effective Range Expansion

This analysis included data from proton energies between 1 and 12 MeV. While many previous phase-shift analyses have been conducted at individual energies and smooth curves fit through the results, this analysis follows [All93b] and is conducted in an energy-dependent way, so that all data are fit at once. This requires a parameterization of the energy dependence of the phase-shifts. The following “effective range expansion”, or expansion in  $k^2$  is used:

$$C_l^2 k^{2l+1} \left[ \cot \delta_{ls}^j + \frac{2\eta H(\eta)}{C_0^2(\eta)} \right] = \sum_{n=0} a_n^{jls} k^{2n}, \quad (6.14)$$

where

$$C_0^2(\eta) = \frac{2\pi\eta}{e^{2\pi\eta} - 1}, \quad (6.15)$$

$$C_l^2(\eta) = C_{l-1}^2(\eta) \left(1 + \frac{\eta^2}{l^2}\right), \text{ and} \quad (6.16)$$

$$H(\eta) = \eta^2 \sum_{s=1}^{\infty} \frac{1}{s(s^2 + \eta^2)} - \ln \eta - \gamma. \quad (6.17)$$

The parameter  $\gamma$  is Euler's constant (0.577216). The mixing parameters are expanded according to:

$$\tan \epsilon(j^\pi) = \sum_{i=1} a_i^j k^{2i} \quad (6.18)$$

Alley and Knutson [All93b] point out that neither of these expansions is strictly correct for use in  $p+^3\text{He}$  elastic scattering, but are merely convenient forms for parameterizing the energy dependence. Equation 6.18 does not include Coulomb effects, and has nowhere been proven accurate, while Equation 6.14 has long been established for scattering, but only in the absence of angular-momentum mixing.

## 6.4 Procedure

We have therefore linked the experimental observables to the effective range parameters through a chain of intermediate quantities, so that any given set of parameter values may be used to calculate corresponding angular distributions of observables. The actual phase-shift analysis consists of finding the set of parameters which best reproduces the experimental measurements. The number of parameters used was kept to a minimum to reduce both the ambiguity between parameters and the overall size of the parameters space to be searched. The phase-shifts and mixing parameters actually used were  $^1\text{S}_0$ ,  $^3\text{S}_1$ ,  $^1\text{P}_0$ ,  $^3\text{P}_2$ ,  $^3\text{P}_1$ ,  $^3\text{P}_0$ ,  $^3\text{D}_j$ ,  $^3\text{F}_j$ ,  $\epsilon(1^-)$ ,  $\epsilon(1^+)$ , and  $\epsilon(2^-)$ . The triplet D phase-shifts were consolidated into a single parameter, since the possible splitting between them was small. The same was done for the triplet F parameters. Three effective range parameters were used to parameterize the energy-dependence of each phase-shift and mixing parameter, so that a total of 36 parameters were fit to the database.

The database was broken into groups of measurements thought to have common normalizations. For each group, labeled with index  $k$ , the  $\chi^2$  was calculated according to

$$\chi_k^2 = \sum_i \left[ \left( \frac{\nu_k f_{ki} - y_{ki}}{dy_{ki}} \right)^2 + \left( \frac{\nu_k - \nu_0}{d\nu_k} \right)^2 \right], \quad (6.19)$$

where the  $f_{ki}$  are the values calculated from effective range parameters and the  $y_{ki} \pm dy_{ki}$  are the experimental measurements. The scale factor for the measurements of group  $k$  is  $\nu_k$ .

The experimenter's estimate of the normalization is  $\nu_0$ , which is always taken to be 1, with uncertainty  $d\nu_k$ .

A FORTRAN computer program, provided by Elizabeth George, was used to perform the parameter search. The minimization package MINUIT was used to vary the effective range parameters in order to minimize the overall  $\chi^2$ :

$$\chi^2 = \sum_{k=1}^{21} \chi_k^2. \quad (6.20)$$

The search routine did not adjust the  $\nu_k$  as an additional search parameter. Rather, at every step in the parameter search, each  $\nu_k$  was analytically adjusted to minimize  $\chi_k^2$ :

$$\nu_k = \frac{\sum_i \frac{y_{ki} f_{ki}}{(dy_{li})^2} + \frac{\nu}{dv_k^2}}{\sum_i \left( \frac{f_{ki}}{dy_{ki}} \right)^2 + \frac{1}{dv_k^2}}. \quad (6.21)$$

Parameter searches were performed on the databases of [All93b] and [Geo03]. The two [Geo03] solutions were reproduced, while the result using the [All93b] database were slightly different from those in Alley's thesis. These three solutions were used as starting points for searches to the full database.

Initial searches of the full database resulted in multiple solutions which had  $\chi^2$ -per-datum between 2 and 3 for the new data, both the present results and those of [Fis06], added to the global database for this analysis. Those solutions were discontinuous in one or more of the  $^1D_2$ ,  $^3D_j$ , and  $^3F_j$  phase-shifts. Removing either the [Fis06] cross-section, [Fis06] analyzing power, or present spin-correlation data did not improve the fit to the remaining data. The fit was improved by removing from the analysis 14 of the approximately 300 new points which had  $\chi^2$  contributions of more than 10, as detailed in Table 6.1. About half of these points seemed simply to be outliers, while the other half were associated with systematic problems. These included some forward angle  $A_{0y}$  points which had been corrected for magnetic steering. Another apparent systematic problem was found for  $A_{y0}$  data at 1.60 MeV, shown in Figure 6.1, for which the four-most-forward angle points disagreed with the phase-shift analysis and were rejected. The resulting  $\chi^2$ -per-datum for the new data was about 1.5 after removing all these points. The effect of their removal on the phase-shifts was generally negligible, and in all cases within the range of systematic error indicated by the single-energy analyses described below.

A single, continuous solution was obtained by fixing the  $^3F_j$  phase-shift at the value obtained from the [All93b] database. This procedure is reasonable, since the F-wave parameters should be most sensitive to the higher-energy data, while the additions to the [All93b] database present in the total database are at energies between 1 and 6 MeV. The results are shown in Table 6.2.

Table 6.1: Points dropped from the phase-shift analysis

Observable	Proton Energy (MeV)	C.M. Angles (°)
$\frac{d\sigma}{d\Omega}$	4.00	49.9
$A_{y0}$	1.60	39.6, 46.1, 52.4, and 58.7
$A_{y0}$	2.25	33.1
$A_{y0}$	3.13	52.4, 136.8
$A_{y0}$	4.00	166.6
$A_{0y}$	3.15	39.6, 52.4
$A_{0y}$	4.02	39.6, 52.4

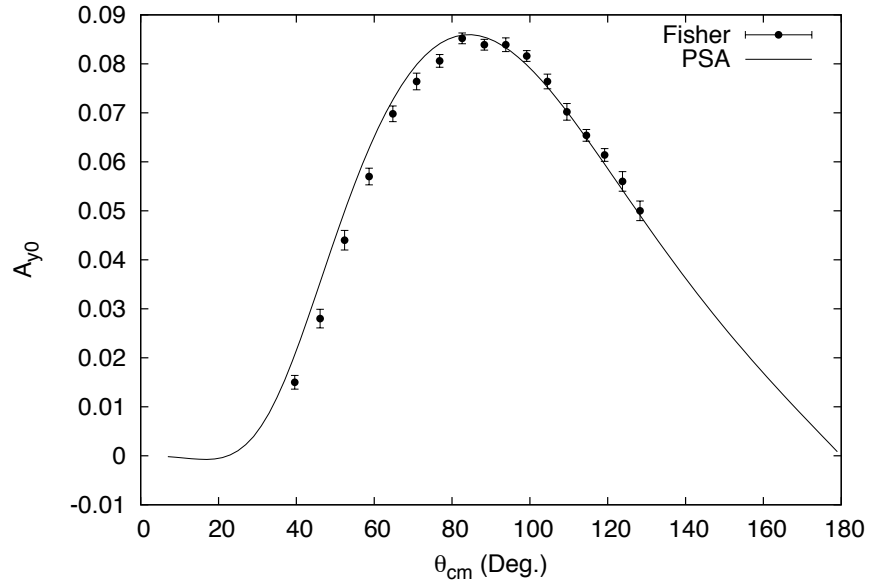


Figure 6.1: Measurements of  $A_{y0}$  at 1.60 MeV [Fis06] shown together with the phase-shift solution. The four most forward-angle points were dropped from the analysis.

Table 6.2: Best-fit effective-range parameters

Phase	$a1 \times 10^{-2}$	$a2 \times 10^{-1}$	a3
$^1S_0$	$-9.0 \pm 0.3$	$7.3 \pm 0.5$	$1.32 \pm 0.19$
$^3S_1$	$-11.02 \pm 0.13$	$7.6 \pm 0.2$	$-0.14 \pm 0.06$
$^1P_1$	$5.74 \pm 0.19$	$-2.4 \pm 0.3$	$4.30 \pm 0.15$
$^3P_2$	$2.108 \pm 0.018$	$1.60 \pm 0.03$	$0.358 \pm 0.014$
$^3P_1$	$1.60 \pm 0.03$	$2.08 \pm 0.06$	$0.59 \pm 0.03$
$^3P_0$	$8.8 \pm 0.2$	$-1.1 \pm 0.2$	$2.20 \pm 0.09$
$^1D_2$	$-31 \pm 7$	$34 \pm 7$	$-12.9 \pm 1.8$
$^3D_j$	$-0.01 \pm 0.23$	$-3.6 \pm 1.0$	$7.1 \pm 0.5$
$^3F_j$	2.29	39.6	-6.49
$\epsilon(1^+)$	$-12 \pm 7$	$42 \pm 8$	$-12.6 \pm 1.9$
$\epsilon(1^-)$	$-415 \pm 10$	$223 \pm 8$	$-39.0 \pm 1.9$
$\epsilon(2^-)$	$4 \pm 12$	$21 \pm 11$	$-9 \pm 3$

In order to gauge the effects of systematic errors, single-energy analyses were performed at energies where new spin-correlation and new or existing cross-section measurements were available, at nominal proton energies of 2.25, 3.13, 4.00, and 5.54 MeV. All measurements within 100 keV of the nominal energies were included. The same program was used for these single-energy fits as for the energy-dependent work, except that the phase-shifts were searched directly, instead of through the effective range parameters. The results are presented in Table 6.3. Phase-shifts and mixing parameters calculated from the global effective-range parameters at the same energies are shown in Table 6.4.

Table 6.3: Single-energy phase-shift results

Phase	2.25 MeV	3.13 MeV	4.00 MeV	5.54 MeV
$^1S_0$	$-37.5 \pm 1.0$	$-45.9 \pm 0.7$	$-56.1 \pm 1.1$	$-68.4 \pm 0.7$
$^3S_1$	$-33.8 \pm 0.5$	$-43.4 \pm 0.3$	$-48.9 \pm 0.3$	$-58.3 \pm 0.3$
$^1P_1$	$10.2 \pm 0.5$	$13.4 \pm 0.4$	$16.2 \pm 0.4$	$20.4 \pm 0.5$
$^3P_2$	$15.9 \pm 0.2$	$26.4 \pm 0.3$	$38.0 \pm 0.2$	$51.6 \pm 0.3$
$^3P_1$	$13.7 \pm 1.2$	$25.0 \pm 0.4$	$34.8 \pm 0.3$	$45.0 \pm 0.4$
$^3P_0$	$11 \pm 3$	$10.5 \pm 0.5$	$15.1 \pm 0.4$	$20.8 \pm 0.3$
$^1D_2$	$-1.0 \pm 0.4$	$-0.6 \pm 0.3$	$-2.2 \pm 0.4$	$-3.2 \pm 0.3$
$^3D_j$	$-0.34 \pm 0.16$	$-0.71 \pm 0.16$	$-1.08 \pm 0.09$	$1.55 \pm 0.09$
$^3F_j$	$-0.03 \pm 0.13$	$0.11 \pm 0.11$	$-0.04 \pm 0.07$	$-0.01 \pm 0.07$
$\epsilon(1^+)$	$0.4 \pm 0.4$	$0.2 \pm 0.3$	$0.8 \pm 0.5$	$1.7 \pm 0.2$
$\epsilon(1^-)$	$-30 \pm 20$	$-13.6 \pm 0.8$	$-11.8 \pm 0.5$	$-12.4 \pm 0.5$
$\epsilon(2^-)$	$-0.5 \pm 1.0$	$0.7 \pm 0.4$	$1.7 \pm 0.7$	$1.4 \pm 0.2$

Table 6.4: Global phase-shift results

Phase	2.25 MeV	3.13 MeV	4.00 MeV	5.54 MeV
$^1S_0$	$-38.6 \pm 0.2$	$-47.9 \pm 0.2$	$-55.7 \pm 0.3$	$-67.4 \pm 0.4$
$^3S_1$	$-34.56 \pm 0.09$	$-42.8 \pm 0.09$	$-49.41 \pm 0.10$	$-58.55 \pm 0.12$
$^1P_1$	$8.22 \pm 0.11$	$13.45 \pm 0.14$	$17.56 \pm 0.16$	$21.44 \pm 0.18$
$^3P_2$	$16.57 \pm 0.05$	$27.53 \pm 0.07$	$37.71 \pm 0.09$	$51.43 \pm 0.12$
$^3P_1$	$17.41 \pm 0.08$	$26.94 \pm 0.11$	$34.98 \pm 0.12$	$45.14 \pm 0.15$
$^3P_0$	$5.22 \pm 0.11$	$9.36 \pm 0.14$	$13.82 \pm 0.14$	$21.08 \pm 0.18$
$^1D_2$	$-0.17 \pm 0.04$	$-0.55 \pm 0.11$	$-1.29 \pm 0.19$	$-3.09 \pm 0.19$
$^3D_j$	$-0.55 \pm 0.03$	$-0.83 \pm 0.04$	$-1.09 \pm 0.04$	$1.51 \pm 0.04$
$^3F_j$	0.007	0.018	0.039	0.11
$\epsilon(1^+)$	$0.29 \pm 0.12$	$0.68 \pm 0.12$	$1.13 \pm 0.09$	$1.91 \pm 0.06$
$\epsilon(1^-)$	$-10.171 \pm 0.009$	$-12.194 \pm 0.017$	$-13.42 \pm 0.03$	$-14.26 \pm 0.05$
$\epsilon(2^-)$	$0.47 \pm 0.12$	$0.75 \pm 0.12$	$1.02 \pm 0.12$	$1.35 \pm 0.14$





## 7 Results

---

### 7.1 Observables

The new measurements of  $A_{0y}$ ,  $A_{yy}$ , and  $A_{xx}$  made for this thesis are shown in Figures 7.1-7.5. Each plot also includes a curve calculated from the best-fit effective range parameters of the global phase-shift analysis (PSA), as well as the measurements of [Sza78b] and [All93a] where available. The overall agreement with the previous measurements is good, with the most forward-angle  $A_{yy}$  points of [All93a] at 5.54 MeV being the only exception, and the present results have smaller error-bars. The new measurements are well-fit by the phase-shift analysis, except for the two most forward-angle  $A_{0y}$  points at 3.15 and 4.02 MeV. The forward-angle target analyzing-power points required the largest correction for magnetic steering, so the disagreement with the PSA may indicate that the correction to those points was not sufficiently accurate. These points, which were not included in the final phase-shift analysis, are plotted as “Outliers”.

Example comparisons of the new measurements and previous measurements of  $A_{y0}$  with the theoretical calculations of the Lisbon [Del07b, Del08] and Pisa [Viv05a] are shown in Figures 7.6-7.8. The numerical results were obtained from the authors. These calculations, discussed in the Chapter 2, are “microscopic” calculations using realistic nucleon-nucleon potential models. All calculations underpredict  $A_{y0}$  substantially. The Lisbon calculation of the ISuj model comes closest to the experimental values, as shown at 5.54 MeV in Figure 7.8, which may be expected since that model was adjusted to reproduce low-energy N-d scattering. The other NN models used by the Lisbon group, some of which are shown in Figure 7.7 at 3.13 MeV, give roughly the same result. The Pisa results for AV18 are similar but not identical to those from Lisbon, with Lisbon results closer to the data. The addition of the UR18 3NF to the Pisa AV18 calculation produces little or no improvement, while the Lisbon CD-Bonn +  $\Delta$  calculation at 5.54 MeV is actually further from the data than the result with only CD-Bonn.

The overall situation for  $A_{0y}$  is much the same, except that the typical underprediction

is a smaller fraction of the observable and the ISuj result actually reproduces the data. The same is true for the AV18+URIX result, in contrast to the Pisa calculation shown in [Fis06]. The spin-correlation coefficients, in contrast, are better described by the calculations, though there is a forward-angle underprediction. The results of each theoretical group show little sensitivity to the choice of model, but the two groups obtain substantial differences for the common potential AV18.

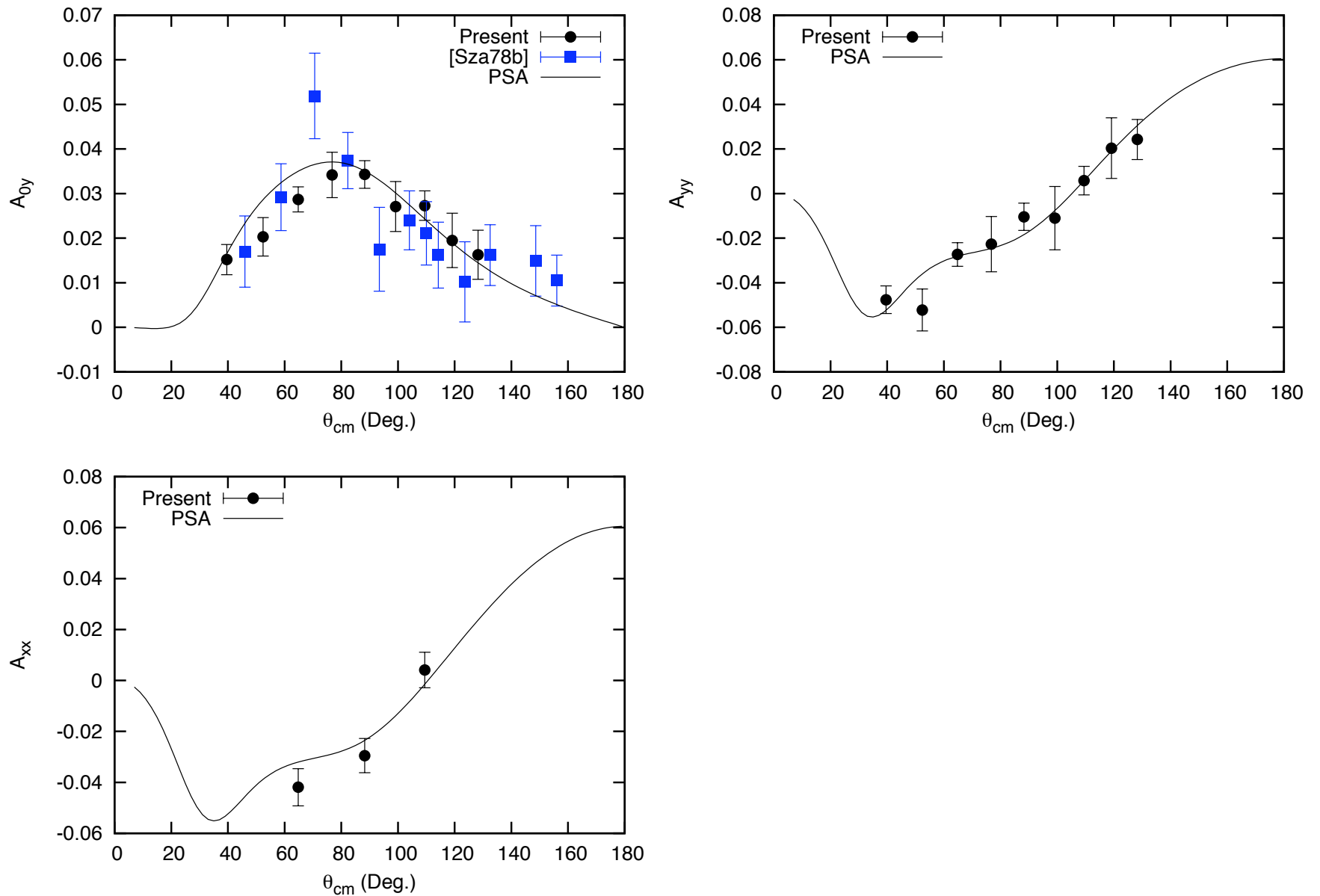


Figure 7.1: Present measurements at 2.28 MeV, together with the global PSA fit. The  $A_{0y}$  measurements of [Sza78b] are also shown.

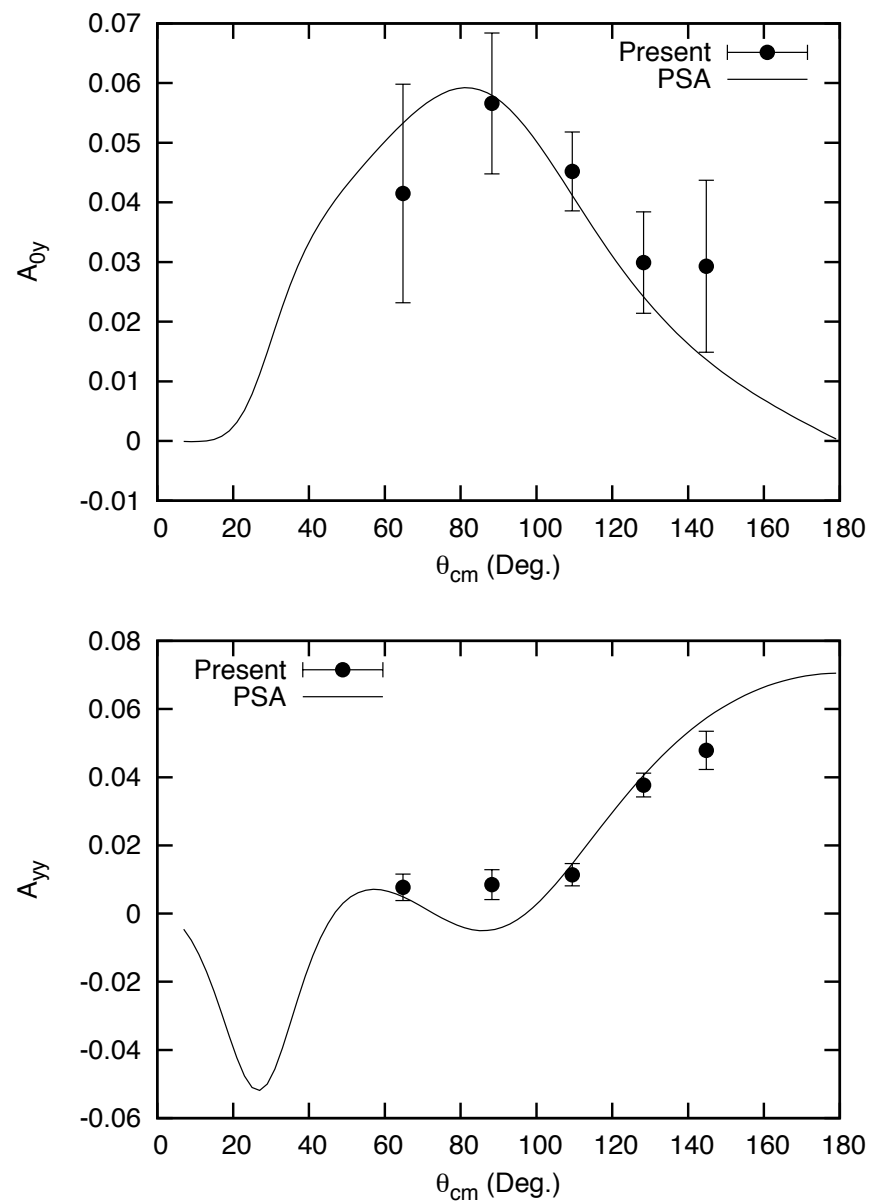


Figure 7.2: Present measurements at 2.77 MeV, together with the global PSA fit.

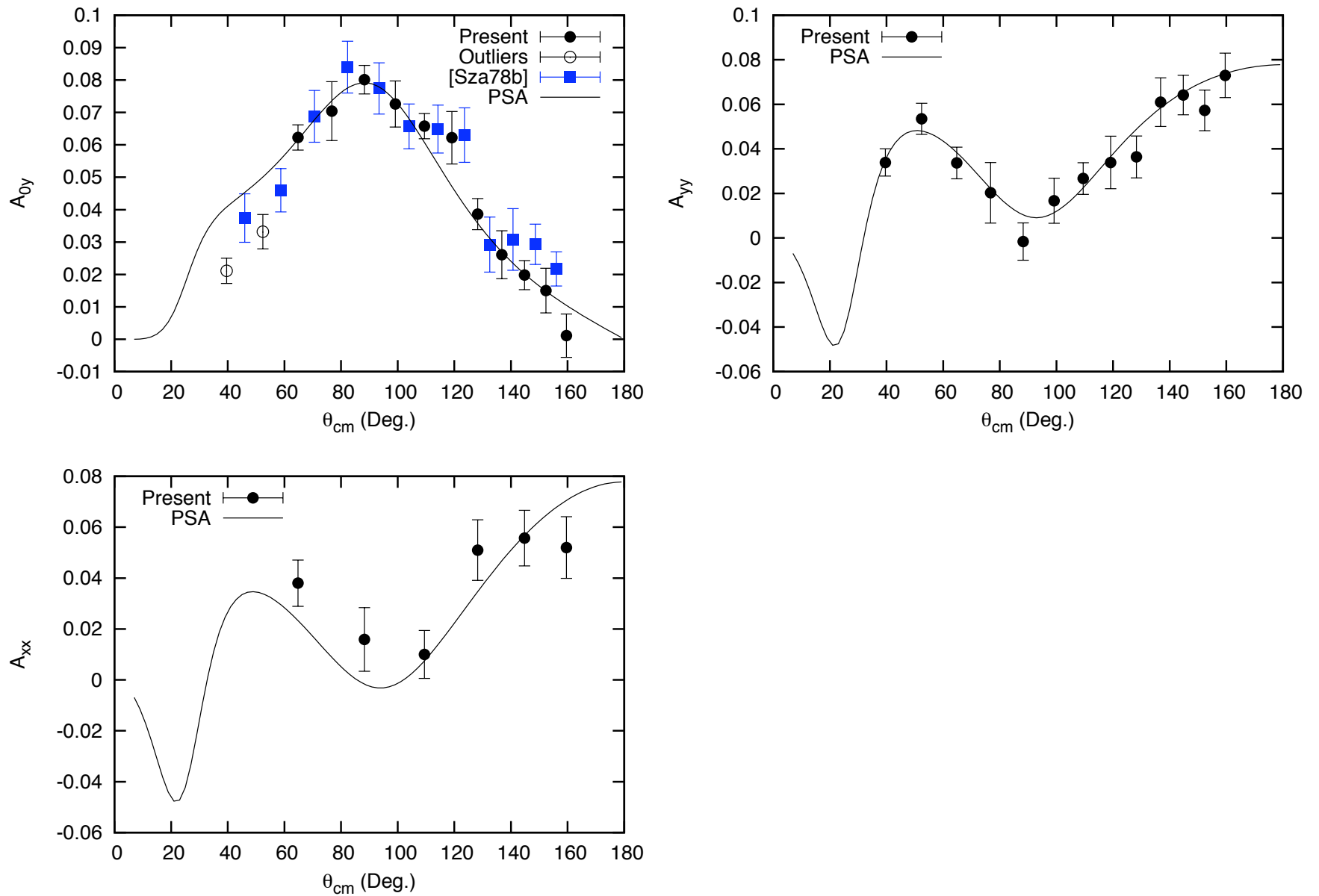


Figure 7.3: Present measurements at 3.15 MeV, together with the global PSA fit. The  $A_{0y}$  measurements of [Sza78b] are also shown.

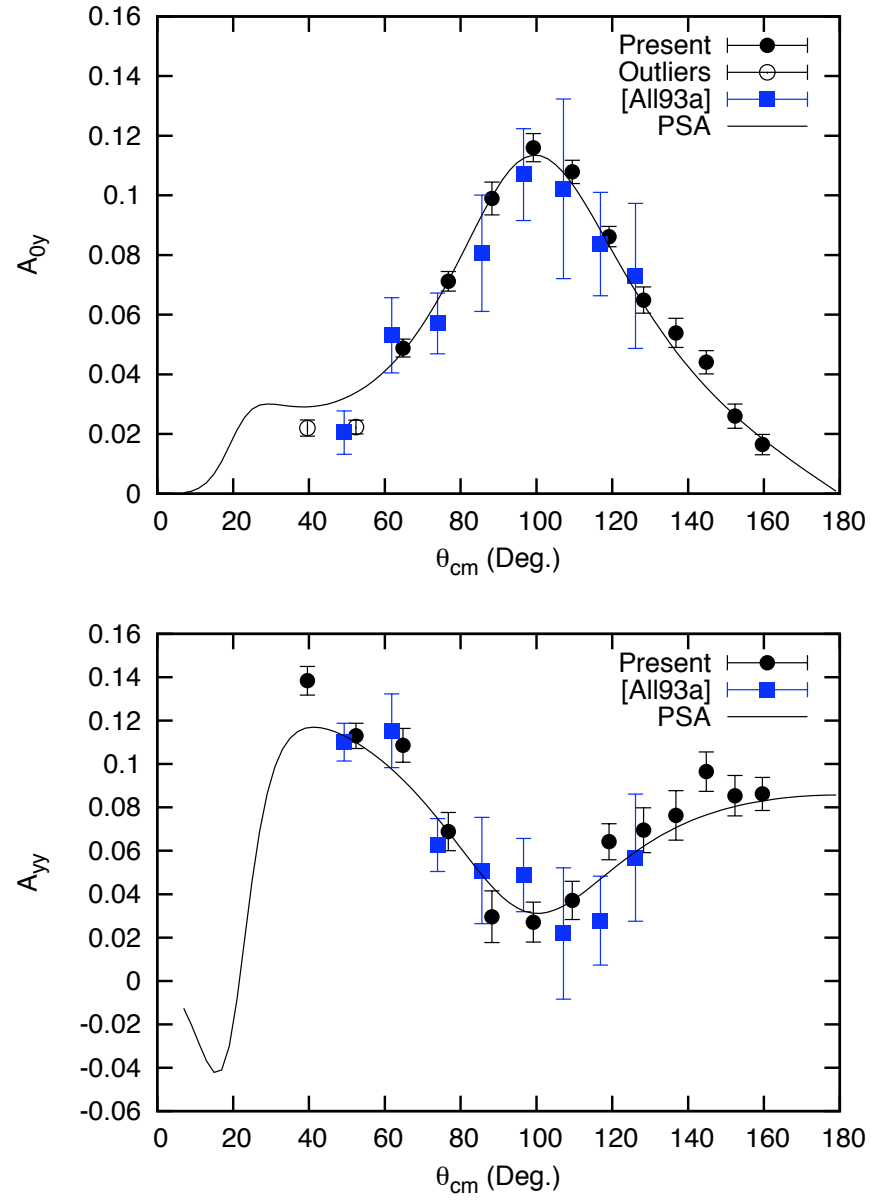


Figure 7.4: Present measurements at 4.02 MeV, together with the global PSA fit. The  $A_{0y}$  measurements of [All93a] are also shown.

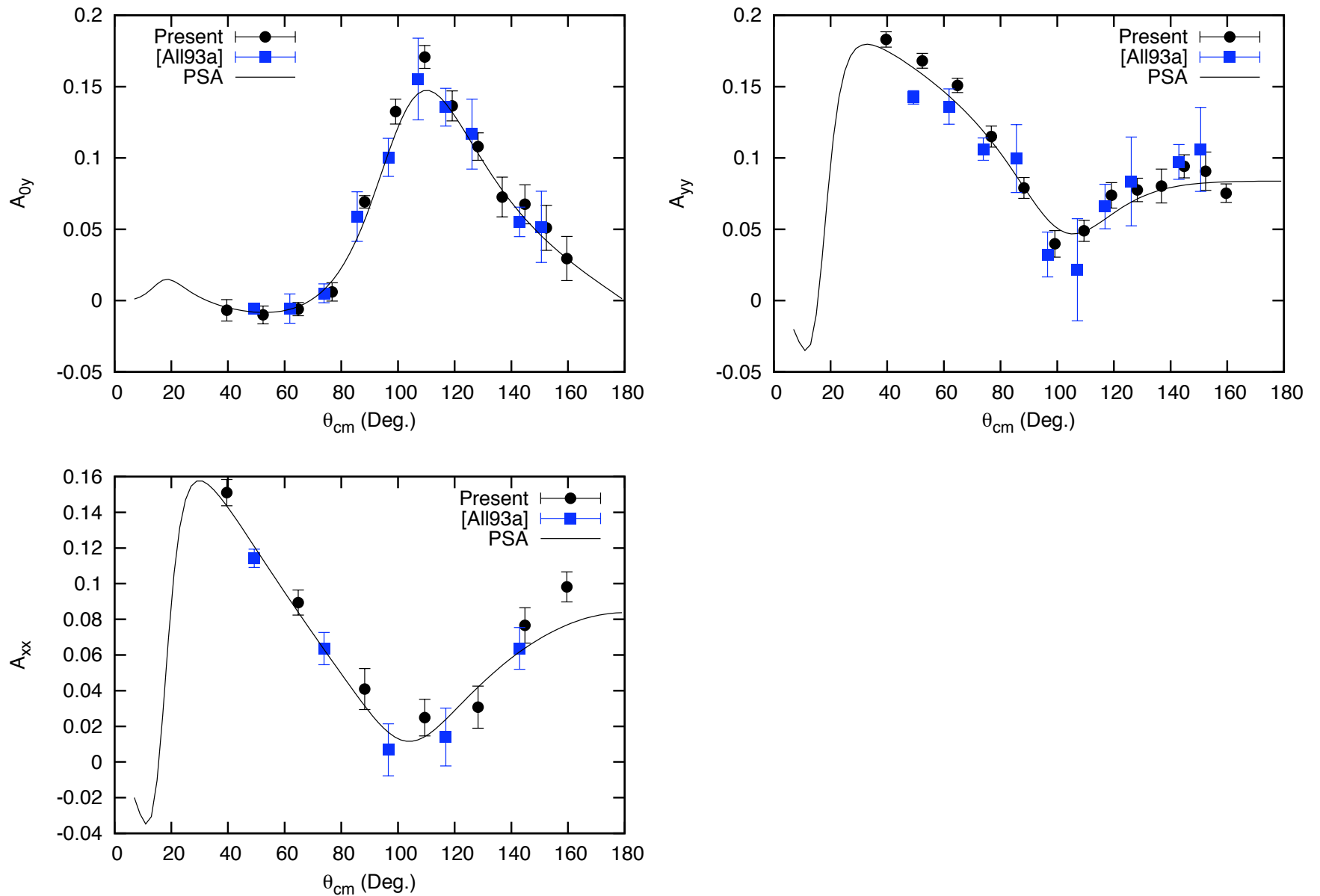


Figure 7.5: Present measurements at 5.54 MeV, together with the global PSA fit. The  $A_{0y}$  measurements of [All93a] are also shown.

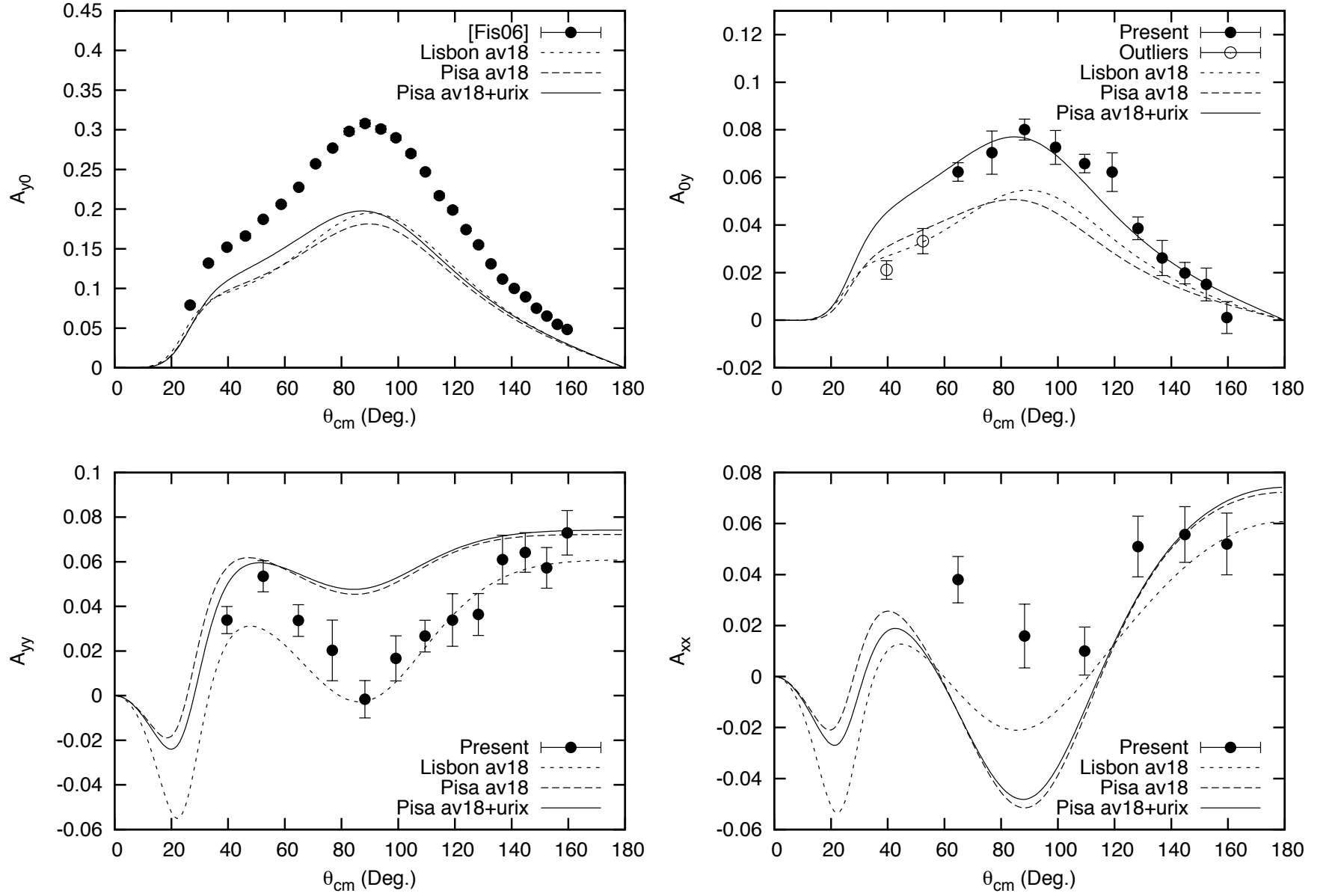


Figure 7.6: Present measurements, along with  $A_{y0}$  [Fis06], are shown with the Lisbon calculation using AV18 and the Pisa results using AV18 and AV18+URIX at 3.15 MeV.



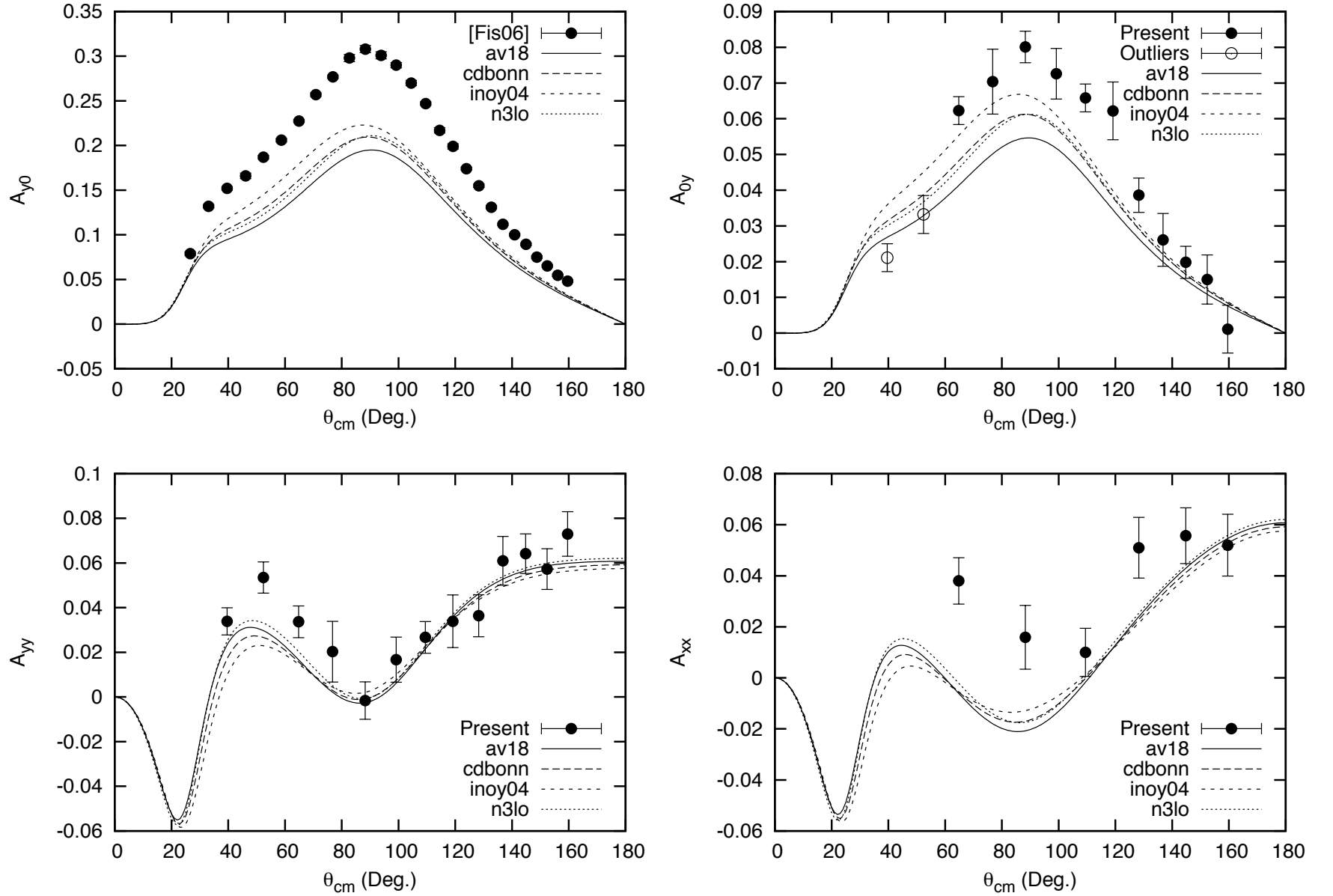


Figure 7.7: Present measurements, along with  $A_{y0}$  [Fis06], are shown with the calculations of [Del07b] using different NN models at 3.15 MeV.

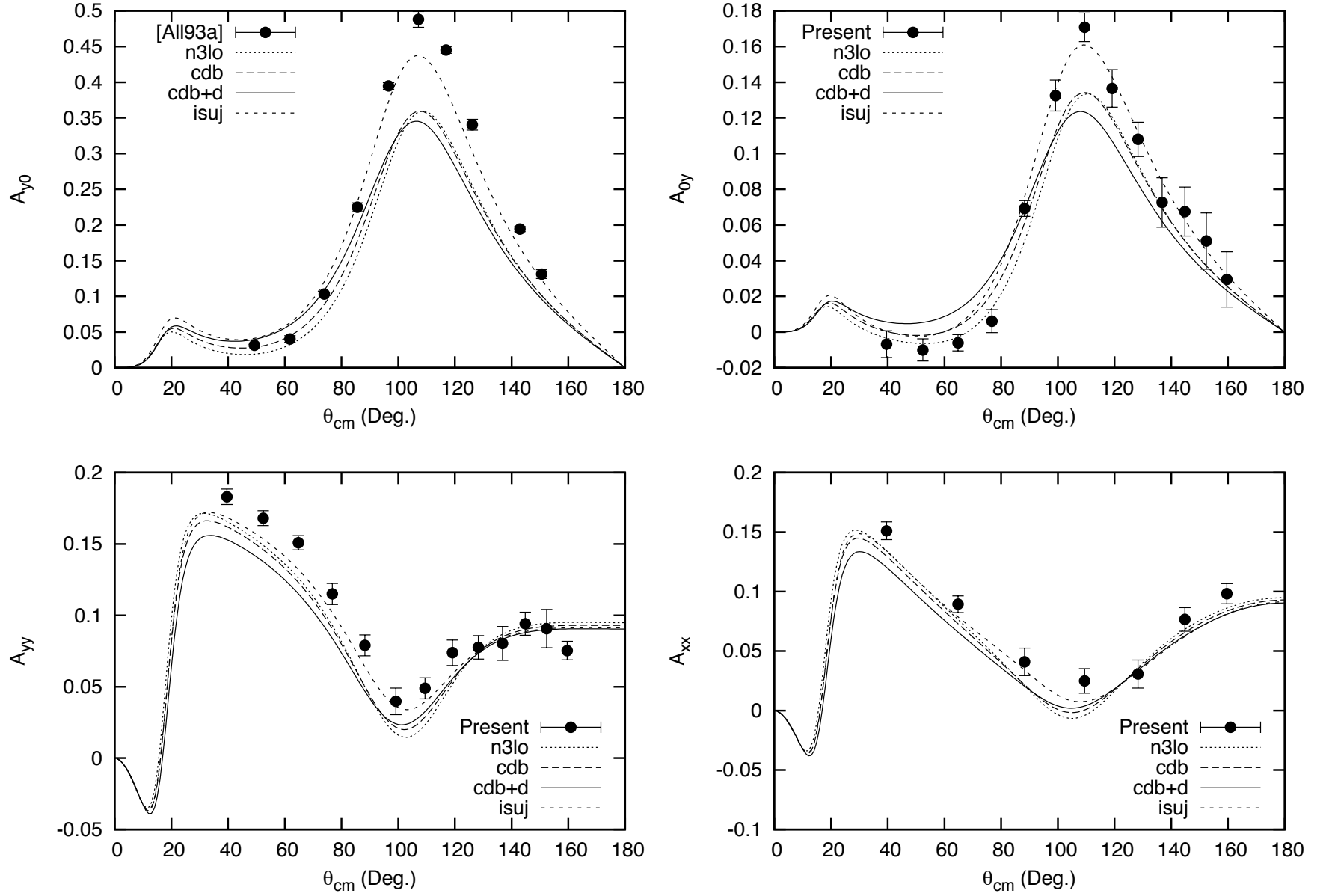


Figure 7.8: Present measurements, along with  $A_{y0}$  [All93a], are shown with the calculations of [Del07b] using different NN models at 5.54 MeV. The calculation using CD-Bonn +  $\Delta$  (“cdb+d”) includes three-nucleons forces.

## 7.2 Phase-Shifts

The phase-shifts and mixing parameters derived from the best-fit effective range parameters are shown vs. proton lab energy in Figures 7.9-7.12, together with the results of [Geo03] and [All93b]. The single-energy analyses performed for this work are also plotted, along with the results of single-energy analyses carried out in [All92] at 7.03, 8.52, and 10.01 MeV, and deviations of those points from the energy-dependent global curve are an indication of systematic errors in the data at those energies. The agreement between all results for  $^3S_1$ ,  $^3P_1$ , and  $^3P_2$  is very good, indicating that those parameters are well-established experimentally. For  $^1S_0$ ,  $^1P_1$ , and  $^3P_0$ , on the other hand, there is significant scatter of the single-energy results about the global result, as well as differences between the two previous analyses with the present one. The addition of the [Ber80] cross-section and proton-analyzing power measurements between 0.1 and 1 MeV to the [Geo03] analysis produces two solutions which differ most for the S-waves below 6 MeV. The present analysis, which includes the [Fis06] cross-sections and proton analyzing powers between 1 and 4 MeV, as well as new spin-correlation coefficients measured between 2 and 6 MeV, restores a single solution which favors the [All93b] S-waves and the [Geo03] P-waves.

In the higher partial waves,  $^1D_2$  shows the greatest sensitivity to systematic errors, while  $^3D_j$  seems well-established. For the global analysis, the  $^3F_j$  parameter was fixed at values obtained from searching the [All93b] database, but agrees well with the single-energy searches where it was a free parameter. The  $\epsilon(1^+)$  and  $\epsilon(2^+)$  mixing parameters were no larger than a few degrees in all analyses. The  $\epsilon(1^-)$  mixing parameter, which mixes singlet and triplet P-waves, differs slightly between the various analyses, and shows appreciable deviations between the single-energy and global fits.

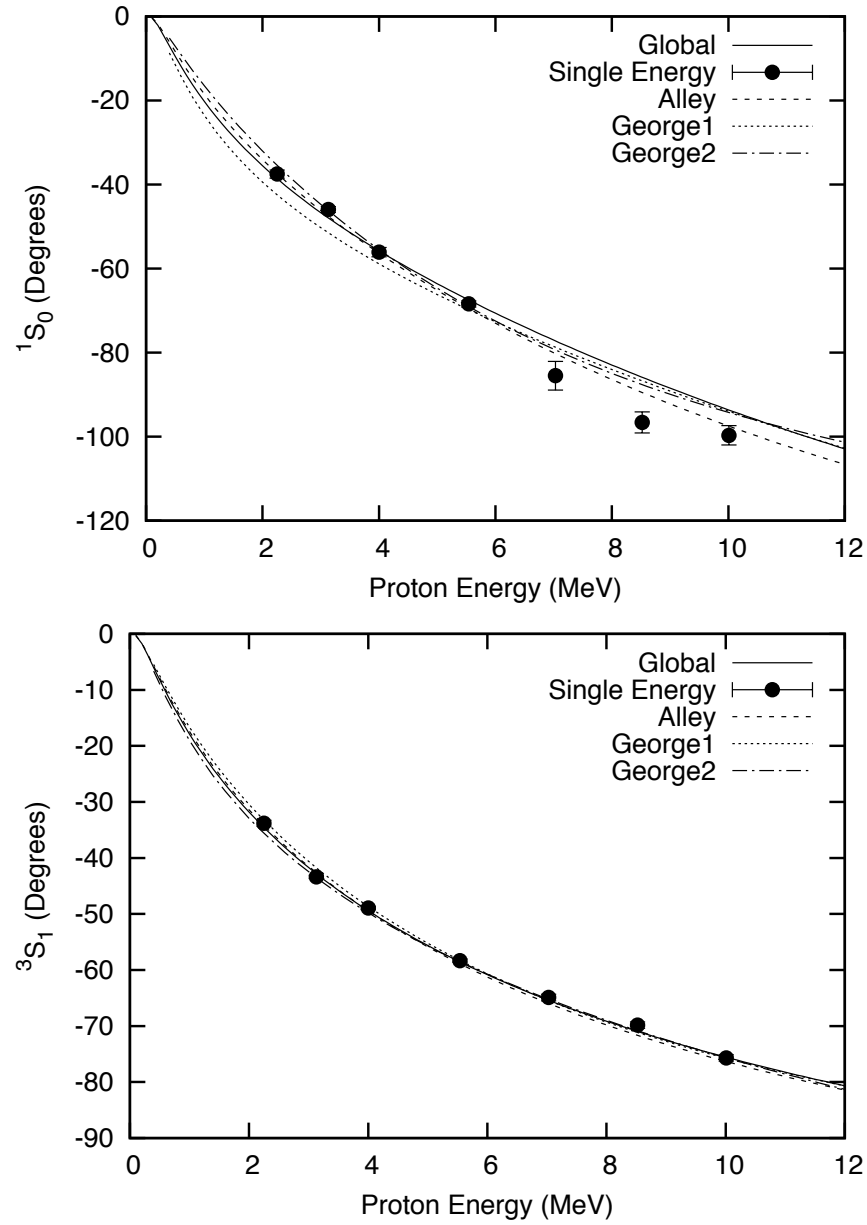


Figure 7.9: The energy-dependent S-wave phase-shift results (“Global”) shown with the single-energy solutions. Deviations between the two are a measure of systematic uncertainty. The previous solutions of [All93b] and [Geo03] are also shown.

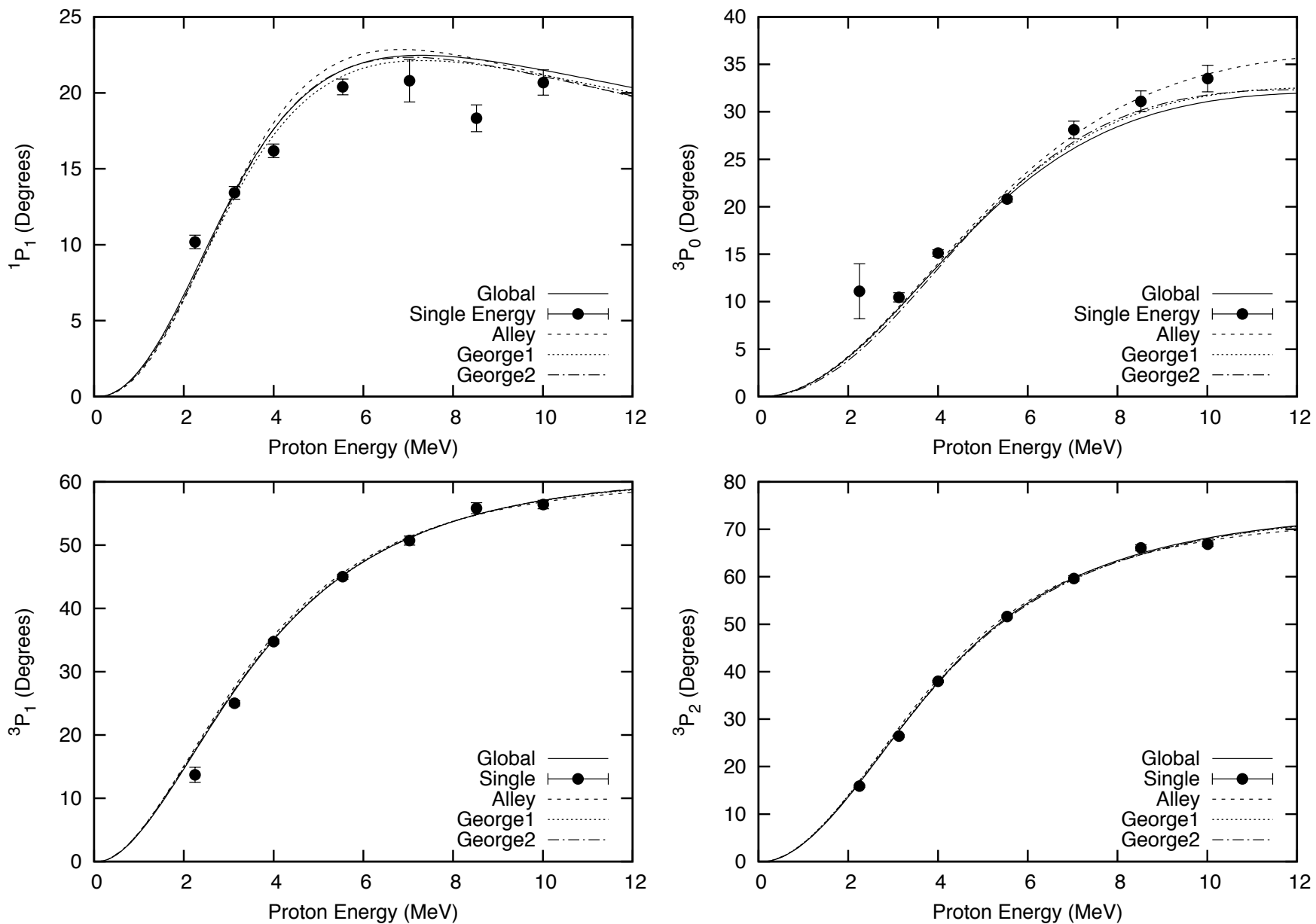


Figure 7.10: The same plots as Figure 7.9, but for P-wave phase-shifts.

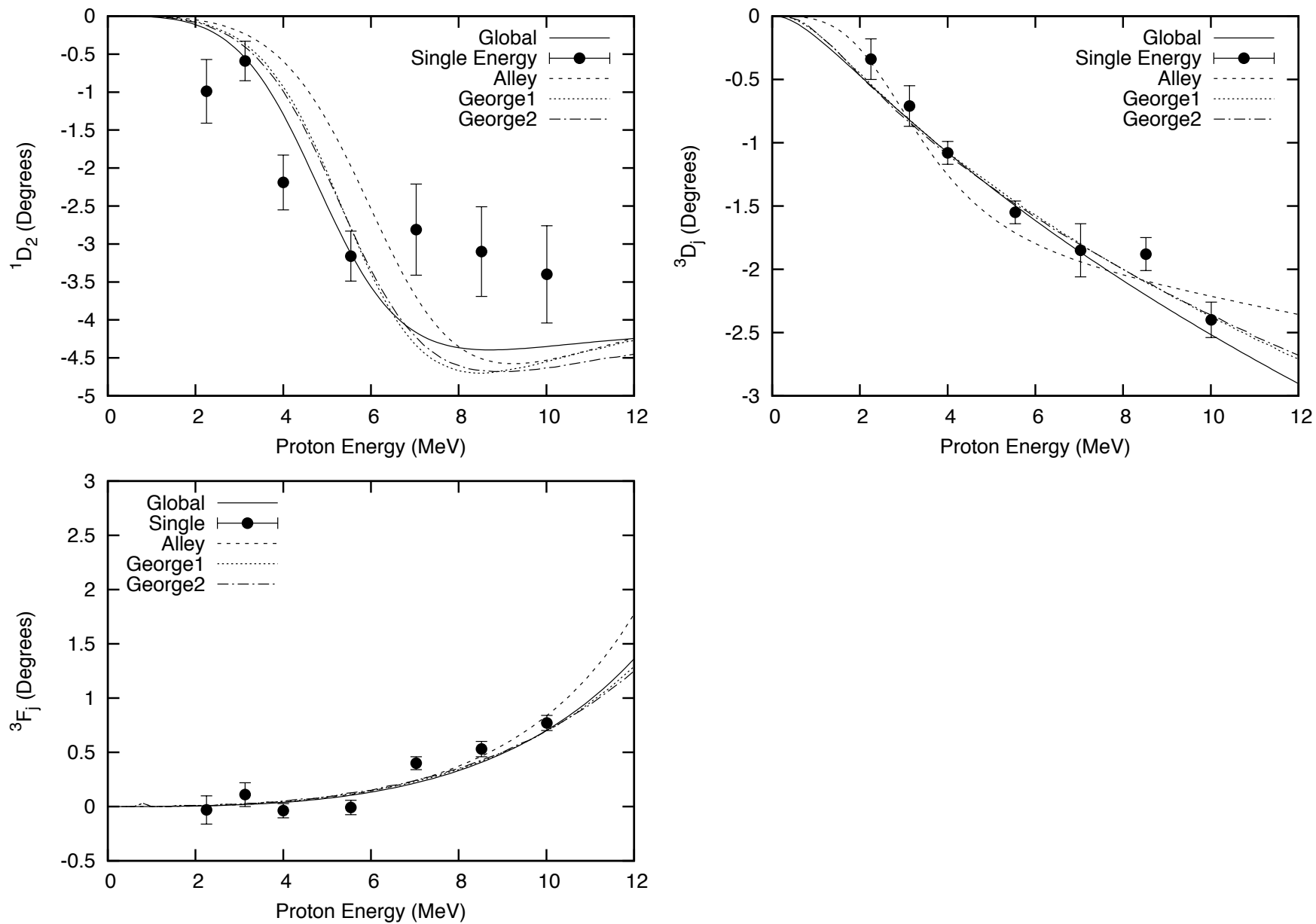


Figure 7.11: The same plots as Figure 7.9, but for D- and F-wave phase-shifts.

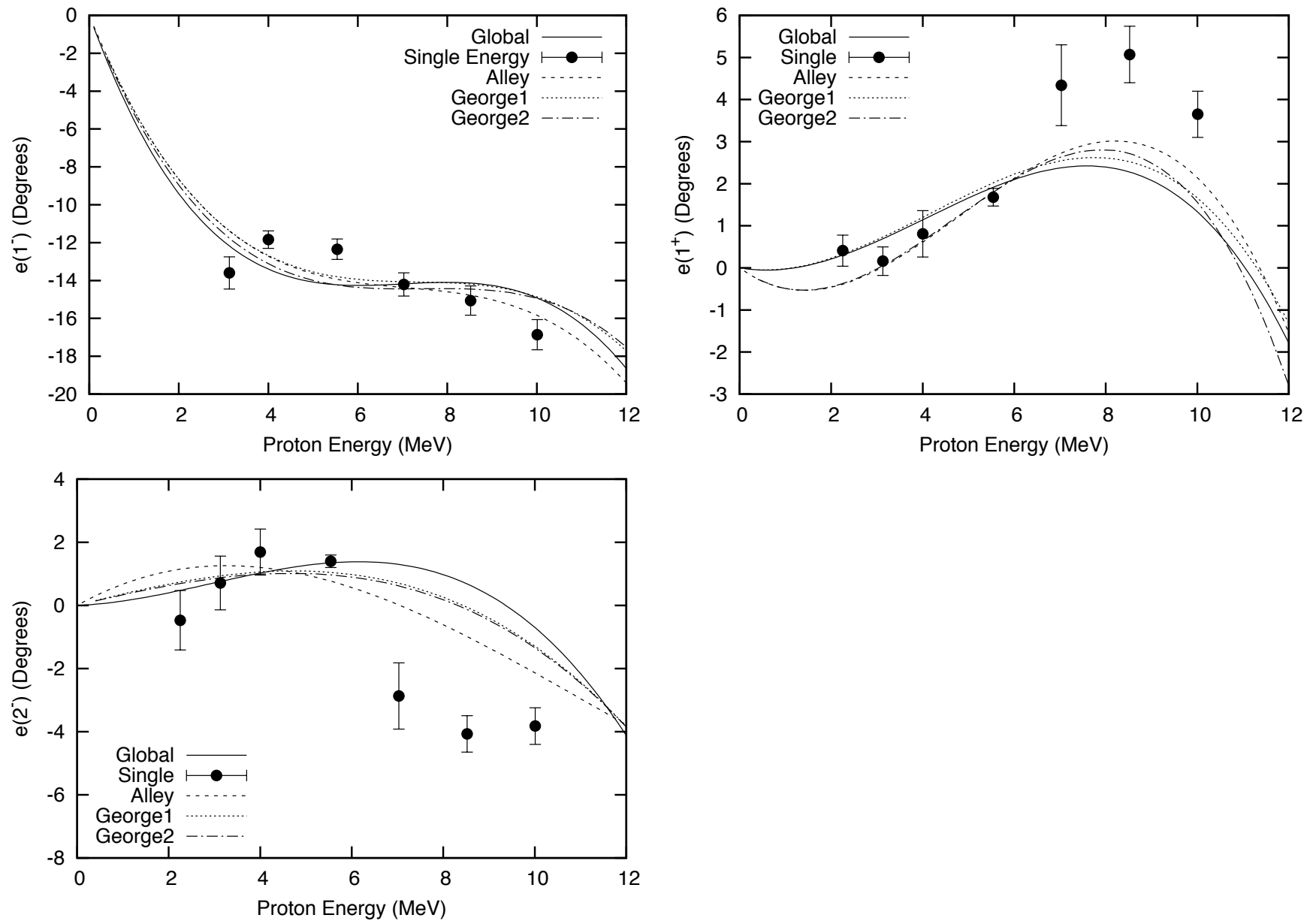


Figure 7.12: The same plots as Figure 7.9, but for the mixing parameters

### 7.2.1 Comparison with Theory

The comparison to the phase-shift results of the Lisbon [Del07b, Del08] and Pisa [Fis06, Viv08] groups is shown in Figures 7.13 - 7.17. The S-wave phase-shift agreement is good, although the theoretical singlet phase-shift calculated using only NN models is slightly more negative than the present experimental result. A similar, though larger, discrepancy was observed [Tor02] for p+d elastic scattering, which was linked to the underprediction of three-nucleon binding energies. A similar connection is observed here, since the p+ $^3\text{He}$  calculation from the Pisa group which includes the URIX three-nucleon force and reproduces the 3- and 4- nucleon binding energies more accurately reproduces  $^1\text{S}_0$ .

There are larger disagreements for the P-wave phase-shifts, however. In general,  $^1\text{P}_1$  and  $^3\text{P}_0$  are overpredicted and  $^3\text{P}_1$  and  $^3\text{P}_2$  are underpredicted. Interestingly, those calculations which agree well with one of those pairs of phase-shifts disagree with the other. For example, the AV18 calculations do well with  $^3\text{P}_1$  and  $^3\text{P}_2$  but poorly with  $^1\text{P}_1$  and  $^3\text{P}_0$ . The addition of the URIX three-nucleon force in the Pisa calculations improves the description of the latter pair of parameters at the cost of worsening the description of the former. This inability of any one calculation to correctly reproduce all the P-wave phase-shifts parallels their common failure to describe  $A_{y0}$ . The underprediction of  $A_{y0}$  in p+d elastic scattering was also linked to small P-wave discrepancies [Tor02, Woo02].

The proton analyzing power depends strongly on the triplet P-wave splitting, especially the combination  $\delta = ^3\text{P}_1 - (^3\text{P}_1 + ^3\text{P}_0)/2$  [Fis06]. That combination is plotted in Figure 7.18 both for the present global analysis and for the Pisa and Lisbon theoretical results, and all calculations produce insufficient splitting. The differences in accuracy between calculations of this splitting mirror the differences in their ability to predict  $A_{y0}$ .

The D- and F-wave parameters, which are small, are reasonably well described by both sets of calculations, though it is interesting to note that the Pisa group's AV18  $^3\text{D}_j$  results lie closer to those of this work than the Lisbon results using the same potential. The theoretical mixing-parameter results shown in Figure 7.17 have been multiplied by a minus sign in order to obtain approximate agreement for  $\epsilon(1^-)$ . This may reflect the ambiguity in the Blatt-Biedenharn parameterization discussed in Chapter 6. The trend of  $\epsilon(1^-)$ , which mixes  $^1\text{P}_1$  and  $^3\text{P}_1$  states, with respect to energy is not reproduced by either theoretical group, though initial results from forthcoming Pisa calculations seem to have better agreement [Viv09].

Our results are also shown in Figure 7.19 with selected calculations of [Ara08] and [Qua08]. Approximate agreement is found for the S-waves and  $\epsilon(1^-)$  over the whole energy range, and below about 2 MeV for the P-waves. The two calculations are roughly comparable in accuracy with respect to the new experimental results. It appears that the inclusion of the break-up channel and the use of multiple cluster states in [Ara08] offsets the use of a less realistic (G3RS) NN potential [Tam68] and simple cluster wave-functions. The agreement for the P-waves of both RGM calculations deteriorates at higher energy as other channels open and



higher cluster excitations become important [Qua08].

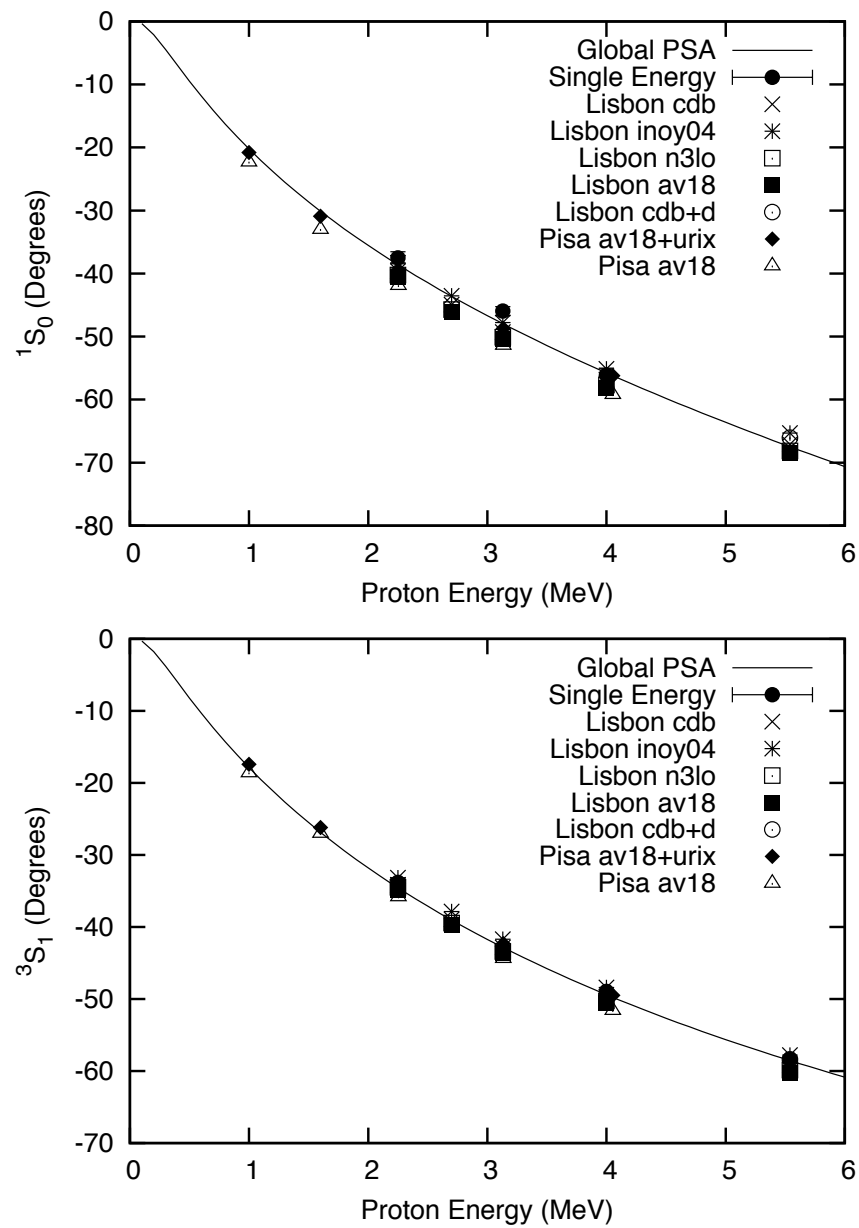


Figure 7.13: Comparison with theoretical S-wave phase-shifts.

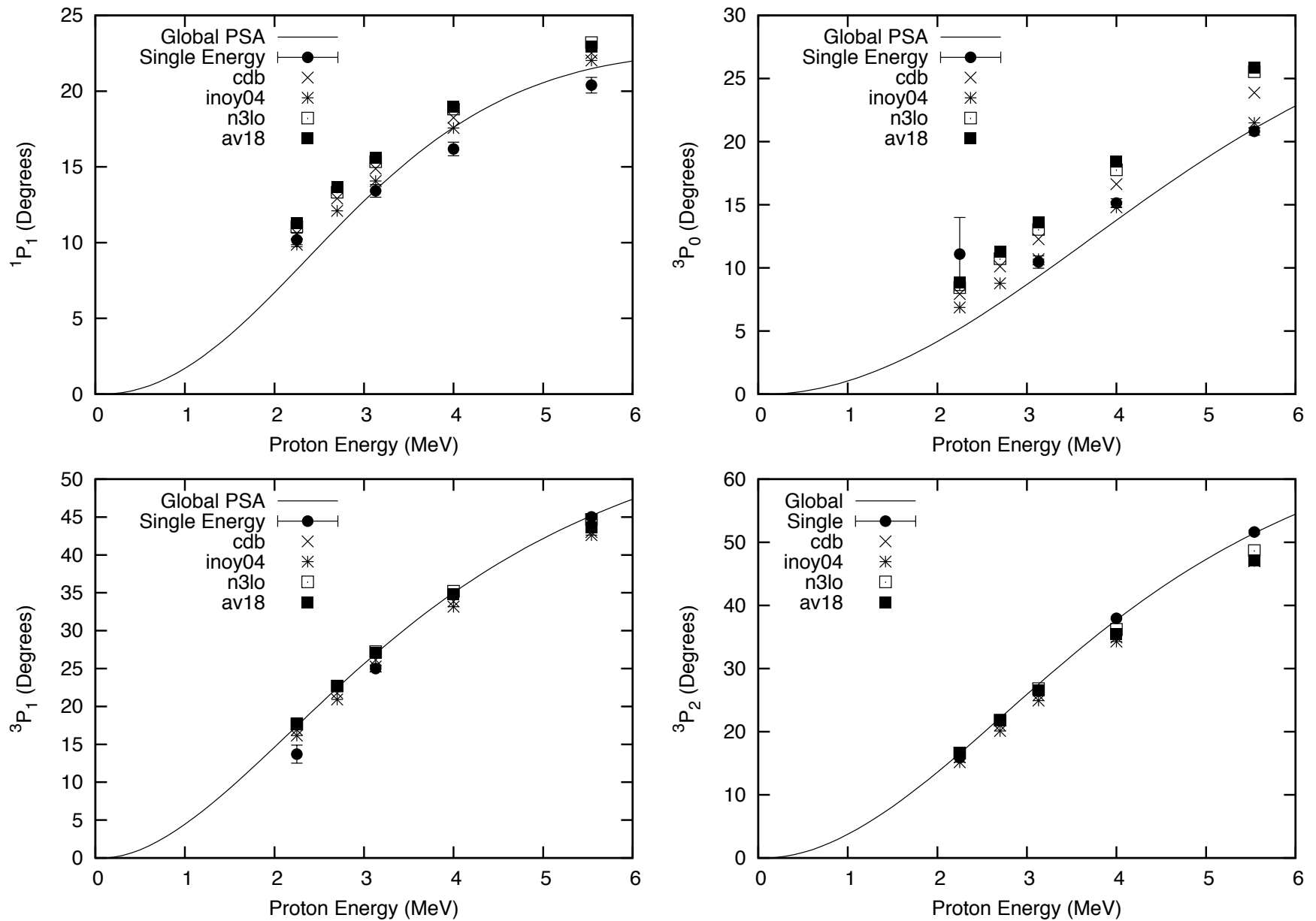


Figure 7.14: Comparison of P-wave phase-shifts with Lisbon NN calculations.

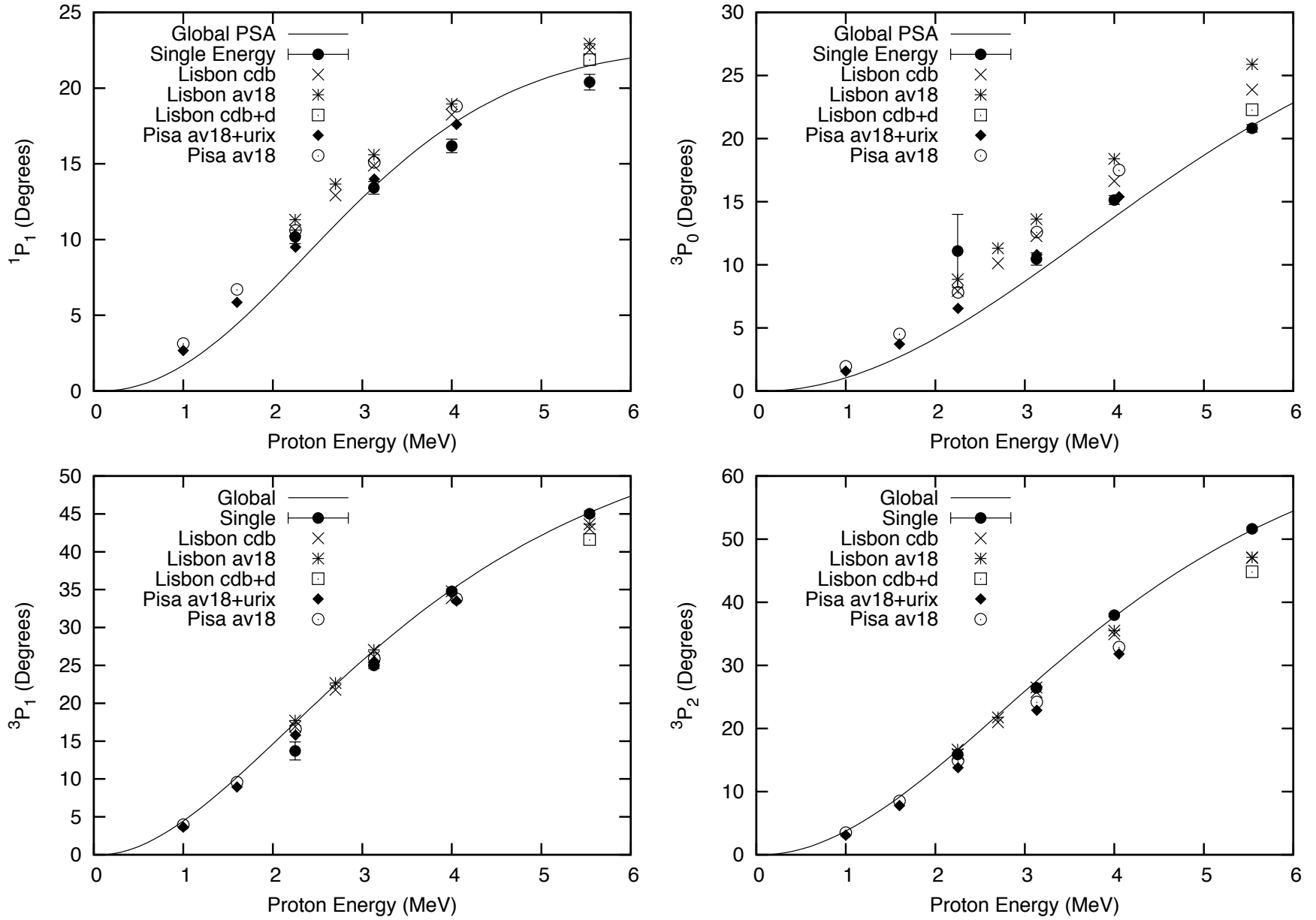


Figure 7.15: Comparison of P-wave phase shifts with Lisbon and Pisa [Viv08] results with and without three-nucleon forces.

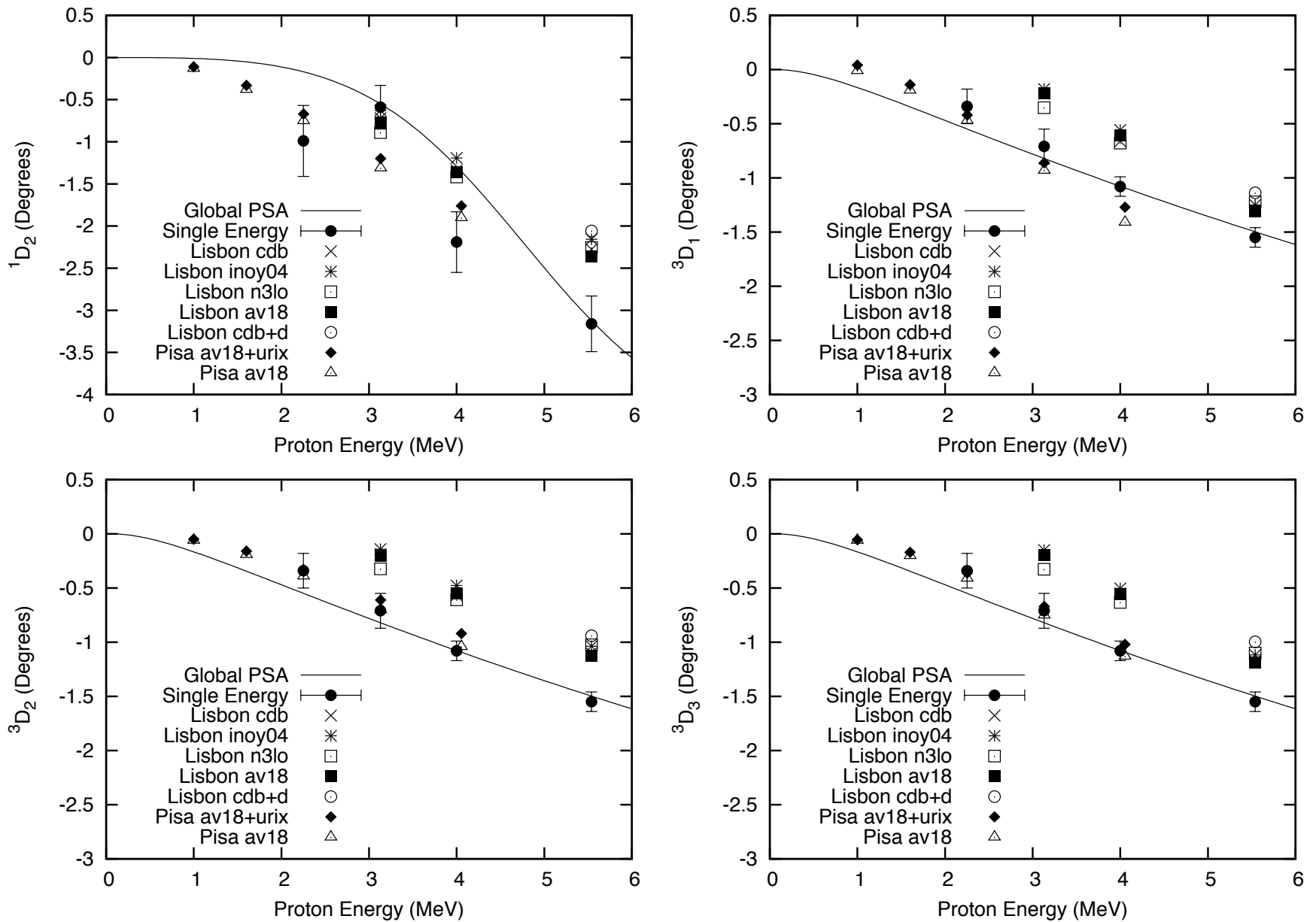
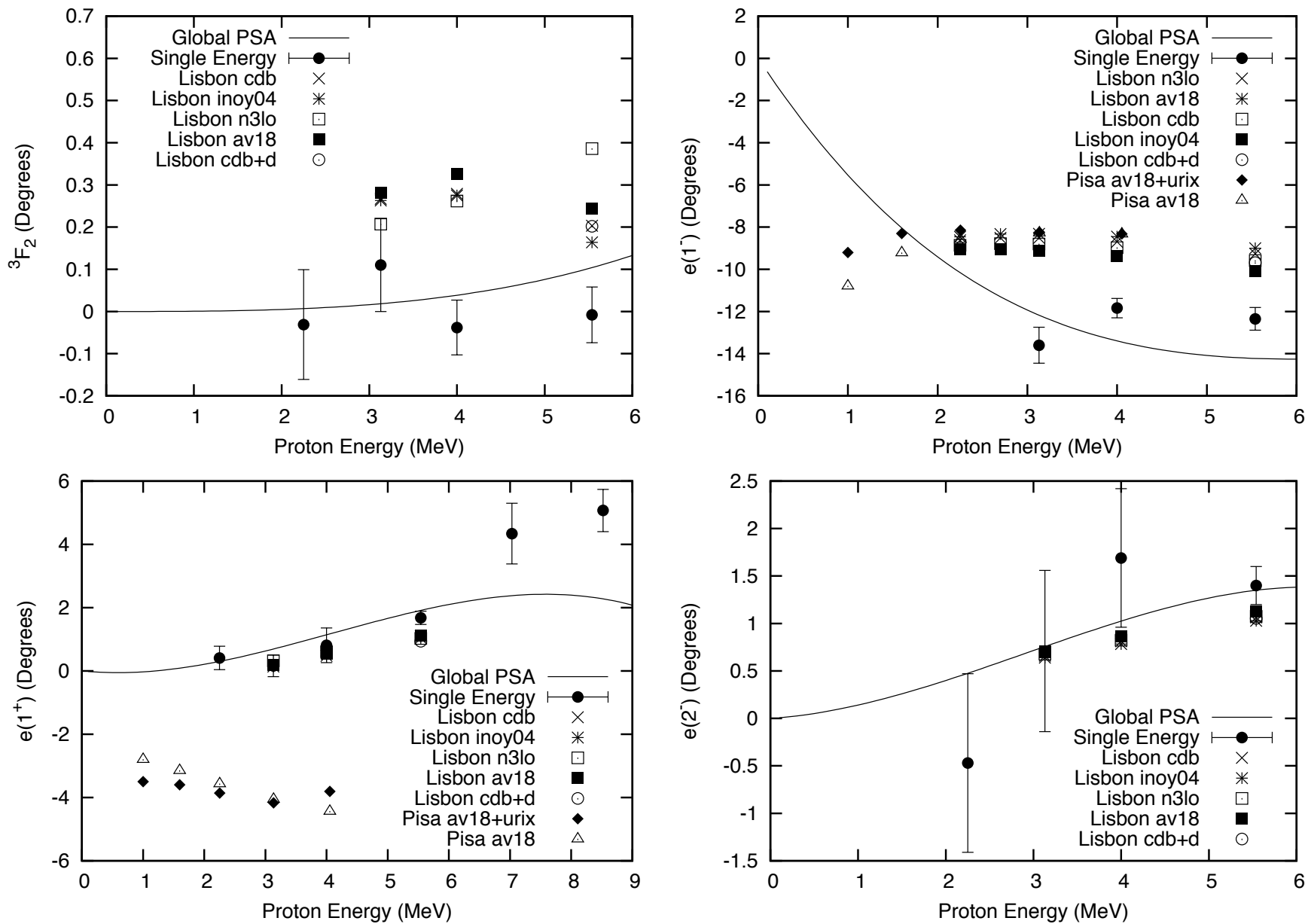


Figure 7.16: Comparison with theoretical D-wave phase-shifts.

Figure 7.17: Comparison with theoretical  ${}^3F_2$  and mixing parameters

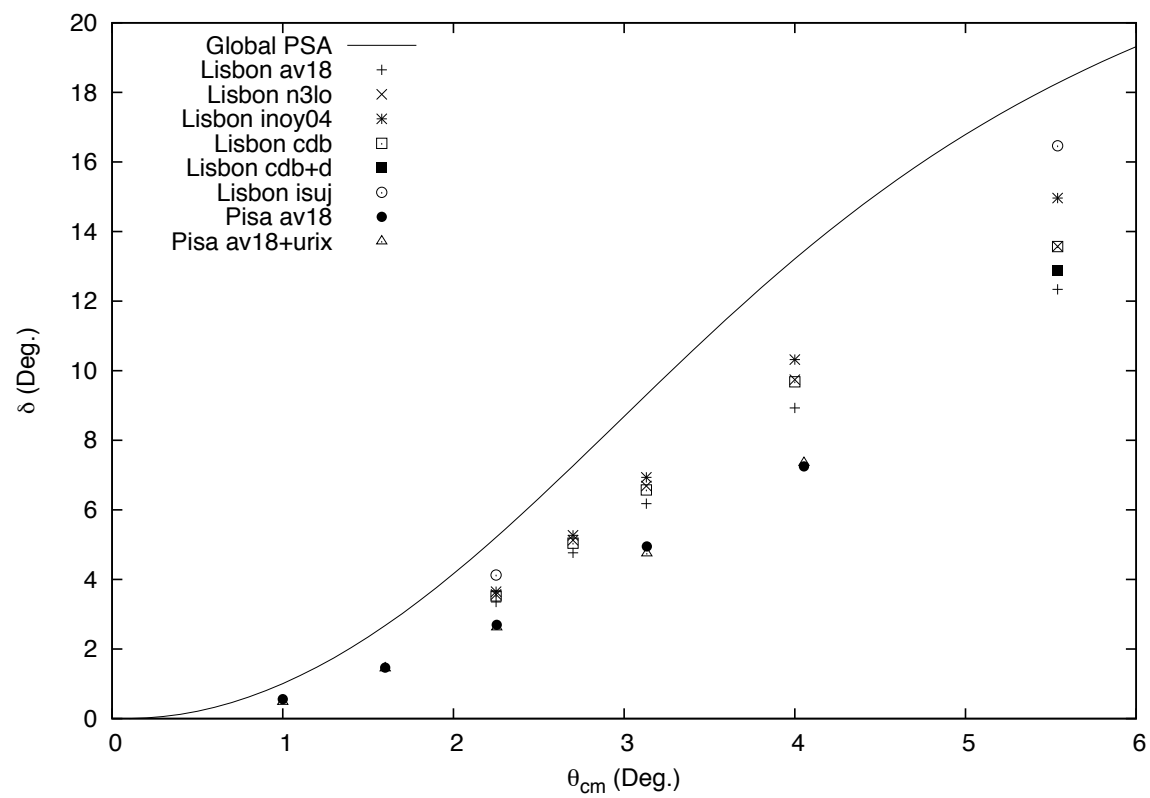


Figure 7.18: Triplet P-wave splitting.

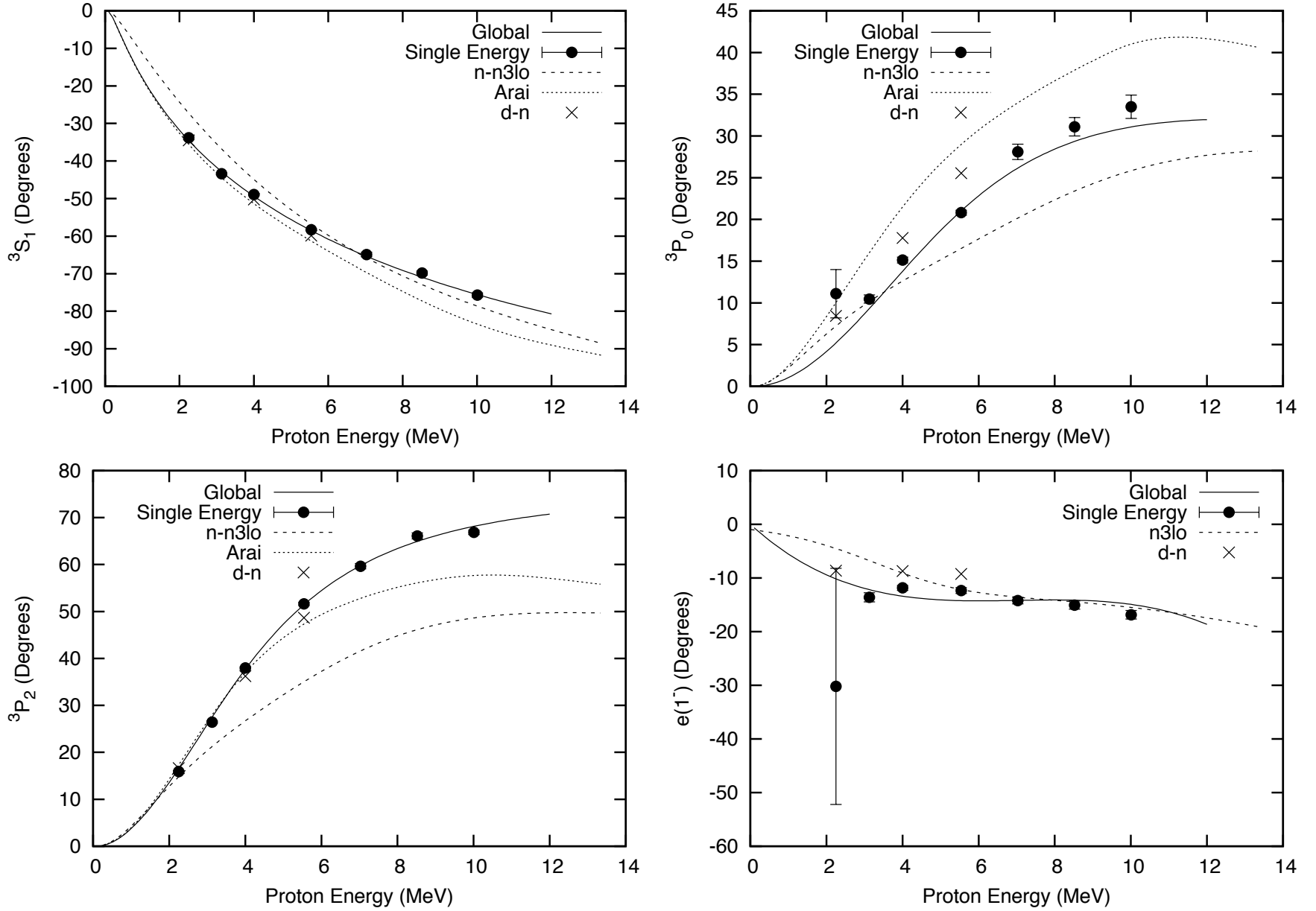


Figure 7.19: The RGM calculations of [Qua08] (“n”) using the N3LO model and of [Ara08] are compared with the new experimental results. The AGS result from [Del07b] using N3LO (“d-n”) is also shown.



Table 7.1: Theoretical scattering lengths

Reference	$a_s$ (fm)	$a_t$ (fm)
[Viv98]	11.5	9.13
[Fil00]	8.2	7.7
[Car91]		$10.1 \pm 0.5$

Table 7.2: Experimental scattering lengths

Reference	$a_s$ (fm)	$a_t$ (fm)
[Teg83]		$10.2 \pm 1.4$
[All93b]	$10.8 \pm 2.6$	$8.1 \pm 0.5$
[Geo03] Soln. 1	$15.1 \pm 0.8$	$7.9 \pm 0.2$
[Geo03] Soln. 2	$7.2 \pm 0.8$	$10.4 \pm 0.4$
[Lev07]	$10.63 \pm 0.52$	$8.88 \pm 0.48$
This work	$11.1 \pm 0.4$	$9.07 \pm 0.11$

### 7.3 Scattering Lengths

Our results for the singlet and triplet scattering lengths are shown in Table 7.2, along with the results of the previous experimental studies and theoretical calculations mentioned in the Introduction. Our results lie between the solutions of [Geo03], with a substantial increase in precision over those of [All93b]. These new values distinguish quite clearly between the available theoretical calculations, being in excellent agreement with [Viv98] and disagreeing with the others. This is perhaps not surprising, since that calculation uses the method with the least approximation and the most recent potential model.

The [Lev07] results were obtained by relating the  $p+^3\text{He}$  scattering lengths and effective range parameters to those for neutron-triton ( $n+T$ ) elastic scattering through a simple interaction model. The  $n+T$  scattering lengths used in that analysis were subject to systematic uncertainties, and the effective range parameters were determined from theoretical calculations. The agreement of the  $p+^3\text{He}$  results with the ones obtained in this work presents the possibility of inverting the [Lev07] analysis to obtain more precise  $n+T$  scattering lengths, as well as effective ranges which are less model-dependent.



## 8 Conclusions

---

The new measurements of  $A_{0y}$ ,  $A_{yy}$ , and  $A_{xx}$  for  $p+{}^3\text{He}$  elastic scattering at proton energies of 2.28, 2.77, 3.15, 4.02, and 5.54 MeV provide an increase in precision over existing measurements, such as those of [All93a] and [Sza78b]. They also include the only spin-correlation data for the system below 4 MeV. The new measurements were made with a new spin-exchange optical pumping polarized  ${}^3\text{He}$  polarized target [Kat05], in which  ${}^3\text{He}$  gas was polarized in an external system at a pressure of 8 bar and dispensed to the scattering target at a pressure of 1 bar. This relatively high target pressure was an important advantage over previous polarized  ${}^3\text{He}$  targets, which were polarized using metastability-exchange optical pumping and operated at a pressure of a few mbar. A further advantage was that the calibration for measurements of the new target's polarization using a separate alpha-scattering experiment, while time-consuming, was simpler and less prone to systematic error than the optical methods used to calibrate previous targets [All93a].

The use of the new target also introduced new challenges. The batch-fill design required that new polarized gas be dispensed to the target every few hours during an experiment, and the optical pumping cell had to be recharged and optically pumped for about a day once the polarized gas was exhausted. Also, the maximum  ${}^3\text{He}$  polarization for much of the experiment was 20-25%, which was a significant reduction from its initial value of 30%. This reduced polarization persisted despite efforts at improved optical pumping cells [Cou06] and frequency-narrowed optical pumping [Arn06]. The development of Rb/K hybrid optical pumping cells, however, substantially reduced the amount of time necessary to repolarize the  ${}^3\text{He}$  gas. Unexpectedly, the  $A_{0y}$  measurements required correction for a systematic effect caused by magnetic steering of the low-energy protons detected in the experiment. The correction was obtained from a combination of unpolarized target measurements and extrapolation of measured asymmetries to zero target polarization.

The new measurements, along with measurements of  $\frac{d\sigma}{d\Omega}$  and  $A_{y0}$  [Fis06], were included in a repetition of the global phase-shift analysis of [Geo03]. These added data, especially the

spin-correlation measurements below 4 MeV, resolved the ambiguity of that analysis, and a single energy-dependent phase-shift solution was obtained. This fit resulted in a  $\chi^2$ -per-datum of 2-3 for the added data, compared to about 1 for the remainder of the dataset. Dropping about 10 points from the more than 300 added ones improved the  $\chi^2$ -per-datum to between 1 and 2 for those measurements. This extraction of unique experimental phase-shifts is the most definitive advance resulting from this work.

The addition of the new data initially produced multiple solutions for the  $^1D_2$ ,  $^3D_j$ , and  $^3F_j$  partial waves which were discontinuous with respect to energy, generally at energies below the lowest-energy measurements of [Ber80] at 300 keV. A single, continuous solution was obtained by fixing the  $^3F_j$  phase-shift at the values of [All93b]. The discontinuity may simply have been the result extrapolating the convenient parameterization of the phase-shift energy-dependence beyond the range of available data. There was also some evidence of systematic disagreements among the lowest-energy data, since the [Ber80]  $A_{y0}$  data were renormalized by about 10% when the analysis included the [Fis06] data. The effect of systematic error was also evident from the deviation of single-energy results from the global fit for some phase-shifts, which were plotted in Figures 7.9-7.12.

The new results for observables and phase-shifts, along with the [Fis06]  $A_{y0}$  results, were compared with theoretical calculations from [Del07b], [Del08], [Viv05a], [Viv08], [Qua08], and [Ara08]. The microscopic calculations from the Lisbon and Pisa groups were substantially closer to the present results than the RGM calculations, even those which used realistic NN models. The Lisbon results showed that several realistic NN potential models qualitatively reproduce the low-energy spin-correlation coefficients within 2-3 sigma of the experimental results. The beam analyzing power, of course, was substantially underpredicted, as was the target analyzing power to a lesser extent. The NN model ISuj, the parameters for which were adjusted from their best-fit values to the NN database to reproduce N+d phase-shifts, was closer to the  $A_{y0}$  and  $A_{0y}$  data, but must be considered less realistic than the other models. The addition of the UR1X 3NF improves the Pisa calculation, and in fact reproduces  $A_{0y}$ , but the use of the CD-Bonn +  $\Delta$  potential degrades the agreement with the Lisbon calculations. A serious disagreement between the two groups for low-energy spin-correlation coefficients using AV18 was observed.

The phase-shift comparison revealed good agreement for the S-wave phase-shifts between Lisbon and Pisa theoretical groups and all realistic models, while discrepancies were observed in the P-waves, especially  $^3P_0$  and  $^3P_2$ . This was not surprising, since  $A_{y0}$  was known to depend sensitively on the triplet P-wave splitting [Fis06]. It was interesting to see that different models deviated from the new experimental results in different ways. Some calculations reproduced  $^1P_1$  and  $^3P_0$ , while others reproduced  $^3P_1$  and  $^3P_2$ , but none reproduced all four. The higher waves and mixing parameters, which, except for  $\epsilon(1^-)$  were small in comparison to the S- and P-waves, were approximately reproduced by theory, though the Pisa AV18

calculations for  ${}^3D_j$  were closer to the experimental result than the corresponding Lisbon calculation. More significant disagreement was observed for  $\epsilon(1^-)$ , though forthcoming Pisa calculations [Viv08] may better describe that parameter.

This work has established that the discrepancy between theory and experiment for  $A_{y0}$  in  $p+{}^3\text{He}$  elastic scattering results from small errors in the P-wave phase-shifts, as predicted in [Fis06]. The same connection was observed [Tor02, Woo02] for  $p+d$  elastic scattering, though the discrepancies were smaller in that system. More generally, the experimental phase-shift results constitute, within their error-bars, a complete description of  $p+{}^3\text{He}$  scattering below 12 MeV. Such experimental information should be useful in evaluating attempts to solve the  $A_y$  puzzle. For instance, calculations using three-nucleon forces up to N2LO in chiral perturbation theory are in progress [Viv08]. It is hoped that systematic chiral approach will be more accurate than the *ad hoc* models considered here.

# Appendices

# A Beam Spin Precession

---

The Wein filter on the TUNL polarized source precesses the beam spin about its dipole magnetic field. The filter itself can be rotated about the beam axis, so the two rotations can combine to produce any arbitrary spin orientation. Further precession of the beam spin, however, occurs after the Wein filter in the bending magnets before and after the accelerator, which precess the spins about an axis perpendicular to the lab floor. The net spin precession for beam tuned down the 52° beam line is 206.8°[Cle03]. The Wein filter setting, therefore, must be adjusted to account for this precession.

The spin orientation on target can be calculated by considering 4 rotations acting on a vector of the spin components,

$$V' = R_4 R_3 R_2 R_1 * V.$$

In what follows, the z axis is along the beam direction at the source, the y-axis is perpendicular to the lab floor, and the x-axis is parallel to the lab floor pointing to the right looking upstream at the source. The rotations are:

$R_1$  : Rotation about the z-axis to align the x-axis with the Wein filter's magnetic field.

$R_2$  : Wein filter precession: Rotation about the x-axis.

$R_3$  : Rotation about the z-axis to make the y-axis vertical.

$R_4$  : Bending magnet precession: Rotation about the yaxis.

In detail:

$$\begin{aligned} \begin{pmatrix} p_x \\ p_y \\ p_z \end{pmatrix} &= \begin{pmatrix} \cos \xi & 0 & \sin \xi \\ 0 & 1 & 0 \\ -\sin \xi & 0 & \cos \xi \end{pmatrix} \begin{pmatrix} \cos \delta & -\sin \delta & 0 \\ \sin \delta & \cos \delta & 0 \\ 0 & 0 & 1 \end{pmatrix} \begin{pmatrix} 1 & 0 & 0 \\ 0 & \cos \epsilon & \sin \epsilon \\ 0 & -\sin \epsilon & \cos \epsilon \end{pmatrix} \\ &\times \begin{pmatrix} \cos \delta & \sin \delta & 0 \\ -\sin \delta & \cos \delta & 0 \\ 0 & 0 & 1 \end{pmatrix} \begin{pmatrix} 0 \\ 0 \\ 1 \end{pmatrix} \\ &= \begin{pmatrix} -\cos \xi \sin \delta \sin \epsilon + \sin \xi \cos \epsilon \\ \cos \delta \sin \epsilon \\ \sin \xi \sin \delta \sin \epsilon + \cos \xi \cos \epsilon \end{pmatrix} \end{aligned} \tag{A.1}$$

The angle  $\xi$  was  $206.8^\circ$ , as discussed above. Settings for  $\delta$  and  $\epsilon$  for spin along the y-axis were  $0^\circ$  and  $90^\circ$ , respectively, while they were  $-90^\circ$  and  $-63.2^\circ$  for spin along the x-axis.



# B Angular Momentum Coupling

---

This appendix aims to clarify the relationship between the incoming and outgoing angular momentum states in the presence of mixing. Two spin-1/2 particles can couple to a total spin of either 1 or 0. A spin-1 system has three projections, and is referred to as a triplet state, whereas a spin-0 state has only one projection and is called a singlet state. Table B.1 illustrates the coupling of total spin  $s$  to the first three relative angular momentum states  $l$  to give the total angular momentum  $j$ . The parity  $\pi$  of the system is equal to  $(-1)^l$ . Each state is also labeled in spectroscopic notation.

Table B.1: Angular momentum coupling

$l$	$s$	$j^\pi$	$^{2s+1}L_j$
0	0	$0^+$	$^1S_0$
0	1	$1^+$	$^3S_1$
1	0	$1^-$	$^1P_1$
1	1	$2^-, 1^-, 0^-$	$^3P_2, ^3P_1, ^3P_0$
2	0	$2^+$	$^1D_2$
2	1	$3^+, 2^+, 1^+$	$^3D_3, ^3D_2, ^3D_1$
3	0	$3^-$	$^1F_3$
3	1	$4^-, 3^-, 2^-$	$^3F_4, ^3F_3, ^3F_2$

The scattering matrix connects states with the same  $j^\pi$ . Table B.2 lists the states mixed up to  $3^-$ . Except for  $j=0$ , the partial waves are connected in pairs.

Table B.2: Mixing between orbital angular momentum states

$j^\pi$	States
$0^+$	$^1S_0$
$0^-$	$^3P_0$
$1^+$	$^3S_1, ^3D_1$
$1^-$	$^1P_1, ^3P_1$
$2^+$	$^1D_2, ^3D_2$
$2^-$	$^3P_2, ^3F_2$
$3^+$	$^3D_3, ^3G_3$
$3^-$	$^1F_3, ^3F_3$



# C Data Tables

---

Table C.1: Data at 2.28 MeV

$\theta_{cm}$	$A_{0y} \pm$		$A_{yy} \pm$		$A_{xx} \pm$	
39.59	0.015	0.003	-0.048	0.006		
52.37	0.020	0.004	-0.052	0.009		
64.79	0.029	0.003	-0.027	0.005	-0.0419	0.0073
76.78	0.034	0.005	-0.023	0.012		
88.25	0.034	0.003	-0.010	0.006		
99.16	0.027	0.006	-0.011	0.014	0.0041	0.0070
109.47	0.027	0.003	0.006	0.006		
119.16	0.020	0.006	0.020	0.014		
128.25	0.016	0.006	0.024	0.009		

Table C.2: Data at 2.77 MeV

$\theta_{cm}$	$A_{0y} \pm$		$A_{yy} \pm$	
64.79	0.042	0.018	0.008	0.004
88.25	0.057	0.012	0.009	0.004
109.47	0.045	0.007	0.011	0.003
128.25	0.030	0.009	0.038	0.004
144.79	0.029	0.014	0.048	0.006

Table C.3: Data at 3.15 MeV

$\theta_{cm}$	$A_{0y}$	$\pm$	$A_{yy}$	$\pm$	$A_{xx}$	$\pm$
39.59	0.021	0.004	0.034	0.006		
52.37	0.033	0.005	0.054	0.007		
64.79	0.062	0.004	0.034	0.007	0.038	0.009
76.78	0.070	0.009	0.020	0.014		
88.25	0.080	0.004	-0.002	0.008	0.0160	0.013
99.16	0.073	0.007	0.017	0.010		
109.47	0.066	0.004	0.027	0.007	0.010	0.009
119.16	0.062	0.008	0.034	0.012		
128.25	0.039	0.005	0.036	0.009	0.051	0.012
136.78	0.026	0.007	0.061	0.011		
144.79	0.020	0.005	0.064	0.009	0.056	0.011
152.37	0.015	0.007	0.057	0.009		
159.59	0.001	0.007	0.073	0.010	0.052	0.012

Table C.4: Data at 4.02 MeV

$\theta_{cm}$	$A_{0y}$	$\pm$	$A_{yy}$	$\pm$
39.59	0.022	0.003	0.138	0.007
52.37	0.022	0.002	0.113	0.006
64.79	0.049	0.003	0.109	0.008
76.78	0.071	0.003	0.069	0.009
88.25	0.099	0.006	0.030	0.012
99.16	0.116	0.005	0.027	0.009
109.47	0.108	0.004	0.037	0.009
119.16	0.086	0.003	0.064	0.008
128.25	0.065	0.004	0.070	0.010
136.78	0.054	0.005	0.076	0.011
144.79	0.044	0.004	0.097	0.009
152.37	0.026	0.004	0.085	0.009
159.59	0.017	0.003	0.086	0.008

Table C.5: Data at 5.54 MeV

$\theta_{cm}$	$A_{0y}$	$\pm$	$A_{yy}$	$\pm$	$A_{xx}$	$\pm$
39.59	-0.007	0.008	0.183	0.005	0.151	0.007
52.37	-0.010	0.006	0.168	0.005		
64.79	-0.006	0.005	0.151	0.005	0.089	0.007
76.78	0.006	0.006	0.115	0.007		
88.25	0.069	0.004	0.079	0.007	0.0401	0.012
99.16	0.133	0.009	0.040	0.009		
109.47	0.171	0.008	0.049	0.007	0.025	0.010
119.16	0.137	0.011	0.074	0.009		
128.25	0.108	0.010	0.078	0.008	0.031	0.012
136.78	0.073	0.014	0.080	0.012		
144.79	0.068	0.014	0.094	0.008	0.077	0.010
152.37	0.051	0.016	0.091	0.013		
159.59	0.030	0.016	0.075	0.007	0.098	0.008



# Bibliography

- [All92] M. T. Alley, Ph.D. thesis, University of Wisconsin-Madison, 1992, Obtained via inter-library loan.
- [All93a] M. T. Alley and L. D. Knutson, Phys. Rev. C **48**, 1890 (1993).
- [All93b] M. T. Alley and L. D. Knutson, Phys. Rev. C **48**, 1901 (1993).
- [Alt67] E. O. Alt, P. Grassberger, and W. Sandhas, Nucl. Phys. B **2**, 167 (1967).
- [Ant96] P. L. Anthony, Phys. Rev. D **54**, 6620 (1996).
- [Ara08] K. Arai, S. Aoyama, and Y. Suzuki, arXiv , 0812.4732v1 (2008).
- [Arn06] C. Arnold, T. Daniels, A. Couture, and T. Clegg, Bull. Am. Phys. Soc. **51**, 20 (2006).
- [Art60] K. P. Artemov, S. P. Kalinin, and L. Samoilov, JETP **37**, 663 (1960).
- [Bab03] E. Babcock, I. Nelson, S. Kadlecik, B. Driehuys, L. W. Anderson, F. W. Hersman, and T. G. Walker, Phys. Rev. Lett. **91**, 123003 (2003).
- [Bak69] S. D. Baker, D. H. McSherry, and D. O. Findley, Phys. Rev. **178**, 1616 (1969).
- [Bar71] H. H. Barschall, editor, *Proceedings of the Third International Symposium on Polarization Phenomena in Nuclear Reactions*, Wisconsin, 1971.
- [Bel85] L. Beltramin, R. D. Frate, and G. Pisent, Nucl. Phys. **A442**, 266 (1985).
- [Ber80] H. Berg, W. Arnold, E. Huttel, H. H. Krause, J. Ulbricht, and G. Cluasnitzer, Nucl. Phys. **A334**, 21 (1980).
- [Bev92] P. R. Bevington and D. K. Robinson, *Data Reduction and Error Analysis for the Physical Sciences*, McGraw-Hill, New York, 2nd edition, 1992.
- [Bla52] J. M. Blatt and L. C. Biedenharn, Rev. Mod. Phys. **86**, 399 (1952).
- [Bly75] C. O. Blyth, O. Karban, W. B. Powell, and S. Roman, Nucl. Phys. **A247**, 1 (1975).
- [Bos72] M. Bosterli and G. Hale, Phys. Rev. Lett. **28**, 1285 (1972).
- [Bro60] J. E. Brolley, Jr., T. M. Putnam, L. Rosen, and L. Stewart, Phys. Rev. **117**, 1307 (1960).

- [Bro96] L. M. Brown and H. Rechenberg, *The Origin of the Concept of Nuclear Forces*, Institute of Physics Publishing, Bristol and Philadelphia, 1996.
- [Car83] J. Carlson, V. R. Pandharipande, and R. B. Wiringa, Nucl. Phys. A **401**, 59 (1983).
- [Car91] J. Carlson et al., Phys. Rev. C **44**, 619 (1991).
- [Car98] J. Carlson and R. Schiavilla, Rev. Mod. Phys. **70**, 743 (1998).
- [Car07] J. Carlson, Nucl. Phys. **A787**, 516c (2007).
- [Cha03] B. Chann, E. Babcock, L. W. Anderson, T. G. Walker, W. S. Chen, T. B. Smith, A. K. Thompson, and T. R. Gentile, J. Appl. Phys. **94**, 6908 (2003).
- [Cle64] T. B. Clegg, A. C. L. Barnard, J. B. Swint, and J. L. Weil, Nucl. Phys. **50**, 621 (1964).
- [Cle95] T. B. Clegg, H. J. Karwowski, S. K. Lemieux, R. W. Sayer, E. R. Crosson, W. M. Hooke, C. R. Howell, H. W. Lewis, A. W. Lovette, H. J. Pfutzner, K. A. Sweeton, and W. S. Wilburn, Nucl. Instr. Meth. **A357**, 200 (1995).
- [Cle03] T. B. Clegg, “Atomic and Nuclear Spin Precession - A Primer”, 2003, Private Communication.
- [Col63] F. D. Colegrove, L. D. Shearer, and G. K. Walters, Phys. Rev. **132**, 2561 (1963).
- [Cou06] A. Couture, T. Daniels, C. Arnold, and T. Clegg, Bull. Am. Phys. Soc. **51**, 20 (2006).
- [Del03] A. Deltuva, R. Machleidt, and P. U. Sauer, Phys. Rev. C **68**, 024005 (2003).
- [Del07a] A. Deltuva and A. C. Fonseca, Phys. Rev. C **75**, 014005 (2007).
- [Del07b] A. Deltuva and A. C. Fonseca, Phys. Rev. Lett. **98**, 162502 (2007).
- [Del07c] A. Deltuva and A. C. Fonseca, Phys. Rev. C **76**, 021001(R) (2007).
- [Del08] A. Deltuva, 2008, Private Communication.
- [Det79] J. R. Detomo, H. W. Clark, L. J. Dries, J. L. Regner, and T. R. Donoghue, Nucl. Phys. **A313**, 269 (1979).
- [Dol03] P. Doleschall, I. Borbely, Z. Papp, and W. Plessas, Phys. Rev. C **67**, 064005 (2003).
- [Dol04] P. Doleschall, Phys. Rev. C **69**, 054001 (2004).



- [Dol08] P. Doleschall, Phys. Rev. C **77**, 034002 (2008).
- [Dri66] L. Drigo, C. Manduchi, G. C. Nardelli, M. T. Russo-Manduchi, G. Tornielli, and G. Zannoni, Nucl. Phys. **89**, 632 (1966).
- [Dri67] L. Drigo and G. Pisent, Il Nuovo Cim. **LI B**, 6751 (1967).
- [Dri05] B. Driehuys, “A Practical Guide to Hyperpolarized Gas Production Via Optical Pumping and Spin Exchange”, 2005, Private Communication.
- [Dua95] F. J. Duarte, editor, *Tunable Lasers Handbook*, Academic Press, Inc., 1995.
- [Ent03] D. R. Entem and R. Machleidt, Phys. Rev. C **68**, 041001 (2003).
- [Fam54] K. F. Famularo, R. J. S. Brown, H. D. Holmgren, and T. F. Stratton, Phys. Rev. **93**, 928 (1954).
- [Fil00] I. N. Filikhin and S. L. Yakovlev, Phys. At. Nucl. **63**, 79 (2000).
- [Fis03] B. M. Fisher, Ph.D. thesis, University of North Carolina at Chapel Hill, 2003, Available from ProQuest UMI Dissertation Publishing, Ann Arbor, Michigan. Publication #3100293.
- [Fis06] B. M. Fisher, C. R. Brune, H. J. Karwowski, D. S. Leonard, E. J. Ludwig, T. C. Black, M. Viviani, A. Kievsky, and S. Rosati, Phys. Rev. C **74**, 034001 (2006).
- [Fra55] R. M. Frank and J. L. Gammel, Phys. Rev. **99**, 1406 (1955).
- [Fra80] P. L. France and P. Winternitz, J. Physique **41**, 1391 (1980).
- [Gei98] W. H. Geist, Ph.D. thesis, University of North Carolina at Chapel Hill, 1998, Available from ProQuest UMI Dissertation Publishing, Ann Arbor, Michigan. Publication #9902466.
- [Geo03] E. A. George and L. D. Knutson, Phys. Rev. C **67**, 027001 (2003).
- [Geo06] E. A. George, 2006, Private Communication.
- [Glö96] W. Glöckle, H. Witala, D. Huber, H. Kamada, and J. Golak, Phys. Rep. **274**, 107 (1996).
- [Got66] K. Gottfried, *Quantum Mechanics*, W. A. Benjamin, Inc., New York, New York 10016, 1966.
- [Har70] D. M. Hardy, R. J. Spiger, S. D. Baker, Y. S. Chen, and T. A. Tombrello, Phys. Lett. **31B**, 355 (1970).

- [Har71] D. M. Hardy, S. D. Baker, and W. R. Boykin, Nucl. Instrum. Meth. **98**, 141 (1971).
- [Jac01] R. E. Jacob, S. W. Morgan, B. Saam, and J. C. Leawoods, Phys. Rev. Lett. **87**, 143004 (2001).
- [Kap62] I. Kaplan, *Nuclear Physics*, Addison-Wesley, 2nd edition, 1962.
- [Kat05] T. Katabuchi, S. Buscemi, J. M. Cesaratto, T. B. Clegg, T. V. Daniels, M. Fassler, H. J. Karwowski, and R. B. Neufeld, Rev. Sci. Instrum. **76**, 033503 (2005).
- [Kav66] R. W. Kavanagh and P. D. Parker, Phys. Rev. **143**, 779 (1966).
- [Koh48] W. Kohn, Phys. Rev. **74**, 1763 (1948).
- [Kra88] K. S. Krane, *Introductory Nuclear Physics*, John Wiley and Sons, 1988.
- [Kra07] K. Kramer and othes, Nucl. Instrum. Meth. A **582**, 318 (2007).
- [Laz05] R. Lazauskas, J. Carbonell, A. C. Fonseca, M. Viviani, A. Kievsky, and S. Rosati, Phys. Rev. C **71**, 034004 (2005).
- [Lee71] C. Leemann et al., Helv. Phys. Acta **44**, 141 (1971).
- [Leo94] W. R. Leo, *Techniques for Nuclear and Particle Physics Experiments*, Springer-Verlag, New York, 2nd edition, 1994.
- [Lev07] V. P. Levashev, Ukr. J. Phys. **52**, 436 (2007).
- [Lov56] R. H. Lovberg, Phys. Rev. **103**, 1393 (1956).
- [Low54] R. W. Lowen, Phys. Rev. **96**, 826 (1954).
- [Mac01] R. Machleidt, Phys. Rev. C **63**, 024001 (2001).
- [May73] D. P. May, S. D. Baker, G. G. Ohlsen, and R. G. Hardekopf, Bull. Am. Phys. Soc. **18**, 1395 (1973).
- [McD64] D. G. McDonald, W. Haberli, and L. W. Morrow, Phys. Rev. **133**, B1178 (1964).
- [McS69] D. H. McSherry, S. D. Baker, G. R. Plattner, and T. B. Clegg, Nucl. Phys. **A126**, 233 (1969).
- [McS70] D. H. McSherry and S. D. Baker, Phys. Rev. C **1**, 888 (1970).
- [Mil89] R. G. Milner, R. D. McKeown, and C. E. Woodward, Nucl. Phys. A **497**, 495c (1989).
- [Mor69] L. W. Morrow and W. Haberli, Nucl. Phys. **A126**, 225 (1969).

- [Nav03] P. Navratil and W. E. Ormand, Phys. Rev. C **68**, 034305 (2003).
- [Nav07] P. Navratil, Few Body Sys. **41**, 117 (2007).
- [Nog02] A. Nogga, H. Kamada, W. Glockle, and B. R. Barrett, Phys. Rev. C **65**, 054003 (2002).
- [Nog03] A. Nogga, A. Kievsky, H. Kamada, W. Glockle, L. E. Marcucci, S. Rosati, and M. Viviani, Phys. Rev. C **67**, 043004 (2003).
- [Ohl72] G. G. Ohlsen, Rep. Prog. Phys. **35**, 717 (1972).
- [Pfi01] B. Pfitzinger, H. M. Hofmann, and G. M. Hale, Phys. Rev. C **64**, 044003 (2001).
- [Pie04] S. C. Pieper, R. B. Wiringa, and J. Carlson, Phys. Rev. C **70**, 054325 (2004).
- [Pla71] G. R. Plattner and A. D. Bacher, Phys. Lett. **36B**, 211 (1971).
- [Pol90] W. N. Polyzou and W. Glockle, Few-Body Sys. **9**, 97 (1990).
- [Pri03] R. Prior, 2003, Private Communication.
- [Qua08] S. Quaglioni and P. Navratil, Phys. Rev. Lett. **101**, 092501 (2008).
- [Qua09] S. Quaglioni and P. Navratil, arXiv **nucl-th**, 0901.0950v1 (2009).
- [Rei03] C. Reiß and H. M. Hofmann, Nucl. Phys. **A716**, 107 (2003).
- [Roh68] U. Rohrer et al., Helv. Phys. Acta **41**, 436 (1968).
- [Ros48] L. Rosenfeld, *Nuclear Forces*, North-Holland, Amsterdam, 1948.
- [Ros60] L. Rosen and J. E. Brolley, Jr., J. Phys. Rad. **21**, 365 (1960).
- [Sch71] P. Schwandt, T. B. Clegg, and W. Haberli, Nucl. Phys. A **163**, 432 (1971).
- [Sil59] E. A. Silverstein, Nucl. Instr. Meth. **4**, 53 (1959).
- [Spi92] M. R. Spiegel and J. Liu, *Mathematical Handbook of Formulas and Tables, Schaum's Outline Series*, McGraw-Hill, New York, 2nd edition, 1992.
- [Sri08] “The Stopping Range of Ions in Matter”, 2008, <http://www.srim.org>.
- [Swa53] P. Swan, Proc. Phys. Soc. **A66**, 740 (1953).
- [Swe55] D. R. Sweetman, Phil. Mag. **46**, 358 (1955).
- [Sza78a] G. Szaloky and F. Seiler, Nucl. Phys. **A303**, 57 (1978).

- [Sza78b] G. Szaloky, F. Seiler, W. Grubler, and V. Konig, Nucl. Phys. **A303**, 51 (1978).
- [Tam68] R. Tamagaki, Prog. Theor. Phys. **39**, 91 (1968).
- [Teg83] P. E. Tegner and C. Bargholtz, Astrophys. J. **272**, 311 (1983).
- [Til92] D. R. Tilley, H. R. Weller, and G. M. Hale, Nucl. Phys. **A541**, 1 (1992).
- [Tom62] T. A. Tombrello, C. M. Jones, G. C. Phillips, and J. L. Weil, Nucl. Phys. **39**, 541 (1962).
- [Tom65] T. A. Tombrello, Phys. Rev. **138**, B40 (1965).
- [Tor02] W. Tornow, A. Kievsky, and H. Witala, Few Body Sys. **32**, 53 (2002).
- [Viv98] M. Viviani, S. Rosati, and A. Kievsky, Phys. Rev. Lett. **81**, 1580 (1998).
- [Viv01] M. Viviani, S. Rosati, A. Kievsky, E. A. George, and L. D. Knutson, Phys. Rev. Lett. **86**, 3739 (2001).
- [Viv05a] M. Viviani, 2005, Private Communication.
- [Viv05b] M. Viviani, S. Rosati, and A. Kievsky, Phys. Rev. C **71**, 024006 (2005).
- [Viv08] M. Viviani, 2008, Private Communication.
- [Viv09] M. Viviani, 2009, Private Communication.
- [Wal97] T. G. Walker and W. Happer, Rev. Mod. Phys. **69**, 629 (1997).
- [Wei78] W. G. Weitkamp, W. Gruebler, B. Konig, P. A. Schmelzbach, R. Risler, and B. Jenny, Nucl. Phys. **A311**, 29 (1978).
- [Wei90] S. Weinberg, Phys. Lett. B **251**, 288 (1990).
- [Whe37a] J. A. Wheeler, Phys. Rev. **52**, 1083 (1937).
- [Whe37b] J. A. Wheeler, Phys. Rev. **52**, 1107 (1937).
- [Wir95] R. B. Wiringa, V. G. J. Stoks, and R. Schiavilla, Phys. Rev. C **51**, 38 (1995).
- [Wir00] R. B. Wiringa, S. C. Pieper, V. R. Pandharipande, and J. Carlson, Phys. Rev. C **62**, 014001 (2000).
- [Woo02] M. H. Wood, C. R. Brune, B. M. Fisher, H. J. Karwowski, D. S. Leonard, E. J. Ludwig, A. Kievsky, S. Rosati, and M. Viviani, Few Body Sys. **32**, 53 (2002).
- [Yos00] Y. Yoshino, V. Limkaisang, J. Nagata, H. Yoshino, and M. Matsuda, Prog. Theo. Phys. **103**, 107 (2000).

- [Yuk35] H. Yukawa, Proc. Phys.-Math. Soc. Jpn **17**, 48 (1935).
- [Zie85] J. F. Ziegler, J. P. Biersack, and U. Littmark, *The Stopping and Range of Ions in Solids*, Pergamon Press, New York, 1985.